博士論文

Wavelength-selective infrared light
emission and detection using modified
distributed-Bragg-reflector structures

(改良された分布ブラッグ反射器を用いた
波長選択赤外線放射・検出の研究)

王　智宇

Wavelength-selective infrared light emission and detection using modified distributed-Bragg-reflector structures

改良された分布ブラッグ反射器を用いた

波長選択赤外線放射・検出の研究

王　智宇

Zhiyu WANG

Department of Mechanical Engineering

The University of Tokyo

Associate Professor Jean-Jacques Delaunay, Supervisor

Abstract

Wavelength-selective absorption of light is required for design of many optical devices, including modulator, photodetector, biosensor, emitter, and optical filter. Surface plasmons (SPs) have been utilized in design of wavelength-selective optical structure for their behaviors of both selective absorbing and enhancing electromagnetic waves in subwavelength metallic structures. As a surface wave of metal, SPs lead to absorption of electromagnetic wave, as a result of free electron oscillation in the metallic structures, which is highly relied on the nature Ohmic losses in metals. Therefore, in order to obtain a high quality factor of resonance, low-loss metal such as Ag, Au and Al are commonly used. The limitation of metals to be chosen, constrains the wavelength-selective SP-based devices for many applications, such as for high temperature, for a good adhesion with dielectric, and for special catalyze use. In addition, these reported SP-based devices rely on two-dimensional/three-dimensional patterned nanostructures, and the fabrication of which involves advanced and costly micro/nanofabrication steps. Therefore, to realize narrowband absorption properties for versatile applications without increasing fabrication complexity, an optical resonance mechanism in a simple structure is required.

As a type of surface wave, optical Tamm state (OTS) has been first proposed in 2005, which exist at the interface between two one-dimensional (1D) distributed-Bragg-reflectors (DBRs). Having a zero in-plane wave vector means that OTS can be excited by light propagating in free space without the need for nanostructures to couple light. Instead of nanostructured metal, loss-less dielectric DBRs contribute to electromagnetic wave confinement, which makes the structure possible to store large energy, and thus the OTS structure is promising to have a better optical behavior in terms of Q-factor. Usually, the structure consisting of metal and DBR is classified from OTS structure, and is called as

"Tamm plasmon structure" or "TP structure", for its strong absorption by metal. This planar multilayer structures based on OTS/TP have attracted great attention due to their potential applications in high-Q-factor perfect absorber. With the idea of modifying the DBR stacks, we demonstrate an improved the wavelength-selectivity of these 1D structures, for applications as thermal emitters and photodetectors.

All matter with a temperature greater than absolute zero emits thermal emission. Thermal emission in mid-infrared (mid-IR or MIR) range (wavelength 2.5~25 µm) provides important light sources for bio-sensing and the detection of gases, since organic chemicals tend to have strong and characteristic absorption resonances (i.e., fingerprint) in the mid-IR range. In order to obtain spectrally resolved information, conventional mid-IR spectroscopy devices use broadband light sources with gratings, which hinder their miniaturization. Therefore, there is a strong motivation to design narrowband thermal emitters as light sources to replace the bulky optical system for portable and low-cost molecular spectroscopy devices. According to Kirchhoff's law, the emittance of a planar surface is equal to its absorptance, and thus, to design a narrowband thermal emitter equivalent to design a perfect absorber in mid-IR range. In order to achieve a high Q-factor absorption in mid-IR range, we explored different strategies, including increase last DBR layer thickness in a TP structure, inserting an optical cavity in a TP structure between metal and DBR, and modifying a OTS structure by adding a metallic layer.

First, we start from a TP structure consisting of a Ge/SiO$_2$/Ge DBR on top and an Au mirror at bottom. Sustaining a TP mode at the interface between Au and DBR, the structure exhibits a near-unity absorptance peak at a wavelength around 5 µm. For this well-developed TP resonance, adding extra DBR layers could increase it wavelength selectivity at expense of its high absorptance. We find that the increase the thickness of

the Ge layer adjacent to Au (i.e., the last DBR layer) can lead to an improvement in Q-factor by at least twice, without losing its high absorption. The improvement of the Q-factor is attribute to more energy stored within the structure, and the similar peak absorptance value indicates that the same impedance matching condition with the corresponding standard TP structure. In addition, we prove that the means of increase the last DBR thickness is more efficient than increase thickness of other DBR layers. This theory get proved by experiments, by increasing the last Ge layer in layer from 282 nm to 910 nm, the Q-factor of emittance peak at 150 C enhances from 22 to 48 with a similar emittance above 0.9.

By inserting an optical cavity with half wavelength optical thickness between DBR and metal, we report a four times enhancement of Q-factor compared without much change in absorptance. From the near-field (electric field distribution), the inserted optical cavity sustains a pronounced standing-wave pattern and thus much larger energy can be stored, leading to an enhancement of Q value; the similar peak absorptance value indicates that impedance matching condition keeps similar with the structure of the standard TP structure without cavity. The structure is fabricated and achieve a peak emittance as high as 0.9 with a Q-factor of 88, giving the highest Q value at that time. The proposed method of inserting cavity in standard TP structure provides a means to drastically enhance the Q-factor without changing the large absorptance, and thus it has been widely applied in design of many optical devices.

Due to the large absorption losses induced by the metallic films, TP structure has a limited Q-factor. Without any metallic film, the OTS structure using two loss-less DBRs to store energy may offer a means to improve the Q value of thermal emitters in a 1D configuration. With this idea, we demonstrate 1D structure consisting of a Ge/SiO_2 OTS

structure and a Pt mirror at bottom and realize narrow-band and wavelength-tunable thermal emission in the mid-infrared range. At the resonance wavelength, light is confined between the two loss-less DBRs of the hybrid metal-OTS structure leading to resonance with a high Q-factor (over 1000 is achieved through simulation) and the bottom metallic mirror blocks the light from leaking out thus providing an inelastic loss channel that guarantees a pronounced absorptance peak. As a result, the approach of modifying an OTS structure by adding a metallic layer, leads to a Q-factor of 780, giving it the highest Q-factor yet reported for a thermal emitter. Moreover, thermo-optic effect of Ge is significantly influence the peak, in the case of this narrow peak. As a result, this sharp emission peak can be actively tune within a range as large as 4.6 times of its bandwidth by controlling the operating temperature. Note that the fingerprints in mid-IR range usually correspond to a resonance with a Q-factor less than 200. Thus, the demonstrated thermal emitter is possible for actual use as light sources in portable chemical- and bio-sensing device.

In another part of my research, designing and improving of TP structures for wavelength-selective hot carrier photodetection are demonstrated. In SP and TP structures, accompanied by photons absorbed in metals, hot carriers can be generated. Extracted via internal photoemission, the hot carriers enable below-bandgap photodetection, and high tunability of the working wavelength by manipulating the structured resonance instead of the materials. Relying on this mechanism, many low-cost semiconductors (e.g., Si, ZnO, TiO$_2$) are possible to be utilized beyond the band-to-band limitations and extend even to near-infrared range, which may decrease the cost for a near-infrared photodetector. Indeed, direct illumination on a metal film can excite hot carriers, but with effective light-trapping mechanisms by SP and TP, generation of hot carriers can be improved at resonance

wavelength, realizing a much efficient and wavelength-selective photodetection. Hot carrier photodetection relying on SP has been demonstrated since 2010, but all of the above require 2D or 3D nanofabrication processes that are costly, and this hinders their practical use. Therefore, to realize narrowband emission over a large-area without increasing fabrication complexity, a planar multilayer structure based on surface-state resonances offers many advantages over 2D or 3D nanostructures.

We report a hot electron photodetector consisting of a modified Ge/SiO_2 DBR structure and an Au/Ti–ZnO–ITO hot electron device on top. ZnO is a well-known semiconductor with a bandgap energy corresponding to a photon in UV range, but utilizing the hot electron internal photoemission from metallic film (Au/Ti) into ZnO, we report a photoresponse even for telecommunication wavelength (around 1550 nm). An anisotropic light absorption in the metallic film (Au/Ti) and the ITO film leading to a predominant hot electron generation primarily in the metal film and transport of these hot electrons from the metallic film to the ITO film. The Au/Ti layers not only act as a hot-electron generator, but also contribute to wavelength dependent photoresponse, for constituting a TP structure with DBR underneath. For an even pronounced wavelength-selective behavior, we modified DBR by increasing the last DBR layer thickness, enabling a wavelength-selective absorptance peak with bandwidth of only 43 nm, which can be monitored by a change of the photoresponse at zero bias. As a result, a wavelength-selective photodetection was demonstrated in the C- and L-band of telecommunication wavelengths (from 1529 to 1607 nm). It is for the first time that a TP-based photodetector is experimentally demonstrated, which reveals the significant of this work.

Acknowledgements

Table of Contents

1. Introduction

1.1 Surface states in one-dimensional structures

1.1.1 Distributed Bragg gratings

A distributed Bragg reflector (DBR) is a reflector formed from multiple layers of alternating materials with varying refractive index, or by periodic variation of some characteristic (such as height) of a dielectric waveguide, resulting in periodic variation in the effective refractive index in the guide [1,2]. Each layer boundary causes a partial reflection of an optical wave. For waves whose vacuum wavelength is close to four times the optical thickness of the layers, the many reflections combine with constructive interference, and thus the DBR act as a high-quality reflector [3].

To form the best constructive interference condition in reflection direction to achieve a high reflection propose, the dielectric layers of a DBR (both of the dielectric materials) are usually set with an optical thickness of a quarter of the target wavelength in vacuum. Nevertheless, the DBR can show high reflection for a range of wavelengths around the target wavelength. Here, the target wavelength is also called as central frequency or Bragg frequency, and the range is called as stopband. Within the stopband, light is "forbidden" to propagate in the structure.

For a DBR with dielectric layers having a quarter of optical thickness of light, the reflectance can be approximately given by

$$R = \left(\frac{n_o n_2{}^{2N} - n_s n_1{}^{2N}}{n_o n_2{}^{2N} + n_s n_1{}^{2N}} \right)^2,$$

where n_o, n_s, n_1, and n_2 are the respective refractive indices of the originating medium

(i.e. index on top of the DBR), the terminating medium (i.e. index below the DBR), and the two alternating materials. N is the number of repeated pairs of low/high refractive index materials [4].

The bandwidth Δf_0 of the stopband can be calculated by

$$\frac{\Delta f_0}{f_0} = \frac{4}{\pi} \arcsin\left(\frac{n_2 - n_1}{n_2 + n_1}\right),$$

where f_0 is the Bragg frequency [5].

From the two equations above, increasing the number of pairs in a DBR will increase the mirror reflectivity, and increasing the refractive index contrast between the materials in the DBRs will increase both the reflectivity and the bandwidth.

Figure 1.1 is shown as an instance. For fixed pair numbers shown as the lower plots of Fig. 1.1, a larger index contrast causes a larger reflection and a wide stopband.
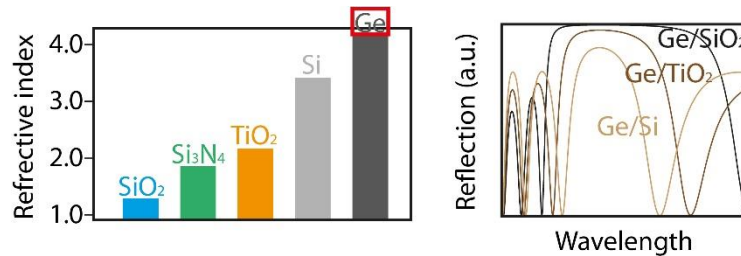
Figure 1.1 reflection spectra of three DBRs with fixed pair number but different materials combinations.

DBRs are critical components in vertical cavity surface-emitting lasers and other types of narrow linewidth laser diodes such as distributed feedback lasers and DBR lasers. They are also used to form the cavity resonator (or optical cavity) in fiber lasers and free-electron lasers.

1.1.2 Optical Tamm state (OTS)

In 2005, Kavokin and coworkers reported an optical surface state that occurs at

2

the interface between two photonic crystals (e.g., two DBRs) with overlapped stopbands [6]. In analogy with Tamm electronic surface states in a semiconductor, they named this new type of surface state "optical Tamm state (OTS)". The resonance wavelength of an OTS device depends on the central wavelength of the DBRs. It is interesting to note that this mode lies partially within the light cone when the in-plane k vector is near zero and the medium of the light cone is air, which means that it can be excited without an additional phase-matching component. As an optical surface wave, the OTS mode exhibits localized interface mode which does not extend into the DBR with negative permittivity or permeability because of its pure imaginary wave number.

From another point of view, the OTS structure with two DBRs can be seen as an optical cavity structure, where the DBRs themselves act as both cavity mirrors (for their high reflection behavior) and optical cavity (owing to their dielectric materials property). Therefore, similar to an optical cavity structure, an OTS can be either TM- or TE-polarized. Due to the loss-less DBRs in OTS structures, the OTS structure is lack of an inelastic loss channel, so, usually, a transmission peak appears at the resonance wavelength.

In 2007, the first experimental result of the OTS structure was reported by GOTO (as shown in Fig. 1.2) [7]. The structure was comprised of two adjoining one-dimensional DBRs deposited on quartz substrates using ion beam sputtering. A standing-wave pattern is shown in the electric field distribution plot. The maximum value localized at the interface of the two DBRs, revealing the surface wave property of the OTS mode (existing at the interface of two DBR). The parameters of the sample were chosen such that the OTS mode (as the curves 3 and 4 in Fig. 1.2c) appears at a wavelength of 800 nm within the DBR stopbands (as the curves 1 and 2).
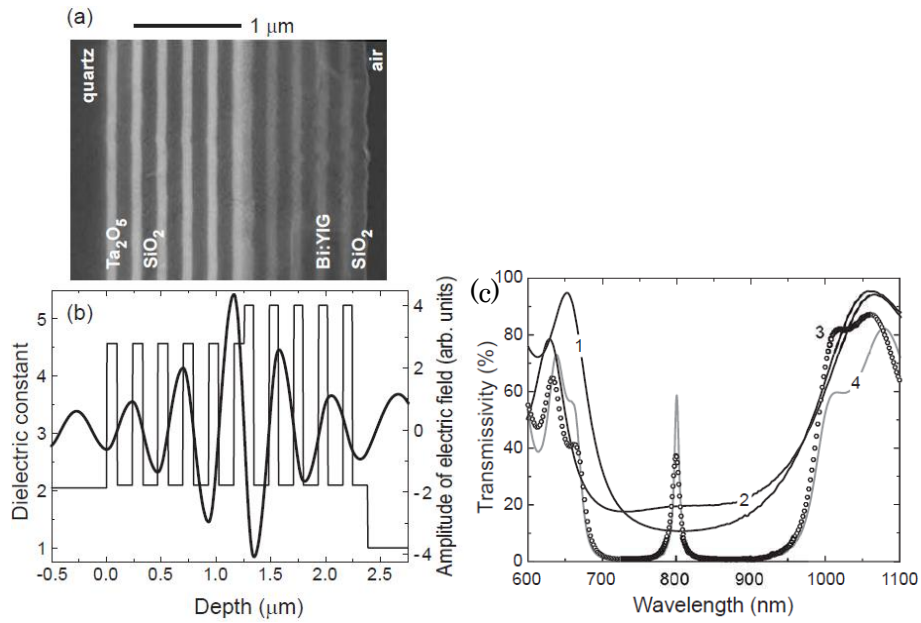
Figure 1.2(a) SEM image of the system of two adjacent DBRs. (b) A plot of the spatial distribution of dielectric constants and the distribution of the electric field amplitude within the sample. (c)Transmission spectra of DBR1 and DBR2 alone are denoted by (1) and (2), respectively. The transmission spectrum of the sample of OTS sample (DBR1 + DBR2) is shown by circles (3);its calculated spectrum is given by curve 4.Reprinted with permission, Copyright © 2008 by American Physical Society.

1.1.3 Tamm plasmon (TP)

In 2007, a class of OTS, Kaliteevski and his coworkers consider the formation of a confined electromagnetic mode at the boundary between an isotropic medium with negative dielectric constant and a DBR (e.g., between metal and DBR) [8]. As in the case of a conventional surface plasmon-polariton, the confinement in the metal is achieved as a result of its negative dielectric constant, but the confinement in the dielectric multilayer structure is due to a photonic stop band of the Bragg mirror. In analogy with the reported optical Tamm state, they called such the reported state a Tamm Plasmon (TP). In the report

by Kaliteevski, two possible configurations of the TP structure is discussed, i.e., a thin metallic film on top of a DBR and a thick metallic mirror underneath a DBR. As shown in Fig. 1.3, both of the two cases exhibit standing-wave patterns of electric field in the DBRs with maximum half-wave attached the metals, decaying towards another end of the DBRs. This distribution reveals the TP modes localizes at the interface of the metals and DBRs.

As depicted in Fig. 1.4, the resonance condition (eigenmode) is also defined as $r_{DBR}r_m= 1$, where r_{DBR} is the reflection coefficient of a wave incident on the DBR from just after the Au layer, and r_{Au} is the reflection coefficient of the wave incident on the Au film from the DBR side (as shown in Fig. 1.4). Note that reflection coefficient is a complex possessing real and imagery parts. As shown in Fig. 1.4, the metal reflection gives a "minus one" reflection coefficient (i.e. $r_m \sim$ -1). The sign of reflection coefficient of a DBR depends on its configuration: a DBR with high index material faced to incidence has a r_{DBR} of -1, while a DBR with low index material faced to incidence has a r_{DBR} of +1. Here, we can simply understand that light gets reflected by metal layer with a phase shift of a value near π, and the phase shift can be zero or π after getting reflected by DBR depending on the DBR's configuration. As a conclusion, TP resonance is sustained only for the case when DBR attaches to metal with the high index material.

Due to absorption and transmission losses in metal film, $|r_m|$ is always less than 1 (imperfect reflector); $|r_{DBR}|$ shows a near-unity value for Bragg frequency (the central frequency of a DBR). Therefore, the definition of $r_{DBR}r_m= 1$ is for perfect condition, which may not be possible in the real case. Nevertheless, it is true that a near-unity maxima value of $r_{DBR}r_m$ indicatesa good light confinement in TP structure, and thus this rule is always employed as an evaluation index for a TP mode. For a real TP structure, a

resonance can exhibit when Re($r_{DBR}r_m$) spectrum showing a maxima (where the imaginary part disappears). The $r_{DBR}r_m$ having a zero imaginary part means that light goes back to initial position without any phase change after the double reflection loop (reflected by the DBR and then reflected by the metal), which is similar to the resonance condition of an optical cavity. See detailed explanations in next section.
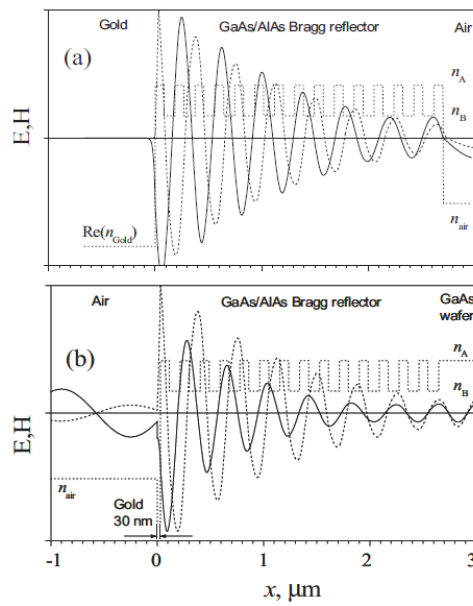
Figure 1.3 (a) The profile of the electric (solid curve) and magnetic (dashed line) fields for a Tamm plasmon at the interface between a semi-infinite metal layer and a GaAs/AlAs DBR structure. (b)Shows a Tamm plasmon at the interface between a 30-nm-thick metal film and a GaAs/AlAs DBR structure. Reprinted with permission, Copyright © 2007 by American Physical Society.
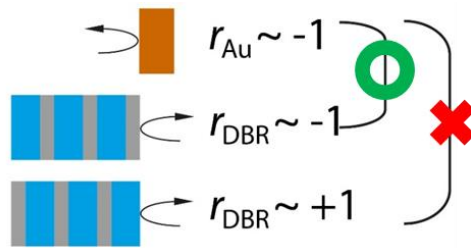
Figure 1.4 r_{DBR} is the reflection coefficient of a wave incident on the DBR from just after the Au layer, and r_{Au} is the reflection coefficient of the wave incident on the Au film from the DBR side. The eigenmode can be expressed as $r_{\text{DBR}}r_{\text{Au}} \approx 1$. Therefore, TP is possible to exist when DBR faces metal with higher index material.

1.2 Wavelength-selective thermal emission

1.2.1 Thermal emission

Thermal radiationor thermal emission is electromagnetic radiation generated by the thermal motion of particles in matter. All matter with a temperature greater than absolute zero emits thermal radiation. Particle motion results in charge-acceleration or dipole oscillation which produces electromagnetic radiation.

Blackbody radiation is the thermal electromagnetic radiation within or surrounding a body in thermodynamic equilibrium with its environment, emitted by a blackbody (an idealized opaque, non-reflective body) [9]. It has a specific spectrum of wavelengths, inversely related to intensity that depend only on the body's temperature, which is assumed for the sake of calculations and theory to be uniform and constant. Relatively, a source with lower emissivity independent of frequency often is referred to as a "gray body". For such a gray body, the thermal emission can be defined by linking with the blackbody emission as $E_{\text{gray}}(\lambda,T) = \varepsilon E_{\text{B}}(\lambda,T)$,where ε is called as emissivity or emittance possessing a value between 0 and 1.Therefore, blackbody emission property can be seen as a fundamental rule in all emission from objects. Here, in order to understand blackbody emission properties, we talk about three theorems for a blackbody: Planck's law, Wien's displacement law and Stefan–Boltzmann law.

If a radiation object meets the physical characteristics of a blackbody in thermodynamic equilibrium, the radiation is called blackbody radiation. Planck's law describes the spectrum of blackbody radiation, which depends solely on the object's temperature [10].

$$\text{B}(v,T) = \frac{2hv^3}{c^2}\frac{1}{e^{\frac{hv}{K_B T}} - 1}$$

Where k_B is the Boltzmann constant, h is the Planck constant, and c is the speed of light in the medium, whether material or vacuum. Planck's law describes the spectral density of electromagnetic radiation emitted by a blackbody in thermal equilibrium at a given temperature T, when there is no net flow of matter or energy between the body and its environment. At the end of the 19th century, physicists were unable to explain why the observed spectrum of black body radiation, which by then had been accurately measured, diverged significantly at higher frequencies from that predicted by existing theories. In 1900, Max Planck heuristically derived a formula for the observed spectrum by assuming that a hypothetical electrically charged oscillator in a cavity that contained black-body radiation could only change its energy in a minimal increment, E, that was proportional to the frequency of its associated electromagnetic wave. This resolved the problem of the ultraviolet catastrophe predicted by classical physics. This discovery was a pioneering insight of modern physics and is of fundamental importance to quantum theory. Thanks to Planck's law, we could obtain a blackbody thermal emission spectrum for a given temperature.

Wien's displacement law states that the blackbody radiation curve for different temperatures will show peaks at different wavelengths that are inversely proportional to the temperature (Emission peak will shift toward shorter wavelengths as temperature increases) [11]. The shift of that peak is a direct consequence of the Planck's law. However, interestingly, it had been discovered by Wilhelm Wien several years before Max Planck developed that more general equation, and describes the entire shift of the spectrum of blackbody radiation. Formally, Wien's displacement law states that the spectral radiance of blackbody radiation peaks at the wavelength λ_{peak} given by:

$$\lambda_{peak} = \frac{b}{T},$$

Where T is the absolute temperature in kelvins, and b is a constant of proportionality called Wien's displacement constant.

The Stefan–Boltzmann law describes the power radiated from a blackbody in terms of its temperature [11]. Specifically, the Stefan-Boltzmann law states that the total energy radiated per unit surface area of a blackbody across all wavelengths per unit time is directly proportional to the fourth power of the black body's thermodynamic temperature T:

$$j = \sigma T^4,$$

Where j is the total energy radiated per unit surface area of a blackbody, and σ is a constant of proportionality called the Stefan–Boltzmann constant.

In summary, for a blackbody, one can obtain its emission spectrum at a given wavelength using Plank's law, while relying on Wien and Stefan-Boltzmann laws, people can easily judge how the emission wavelength or emission energy change as temperature of a blackbody increases (or decreases), as shown in Fig. 1.5.
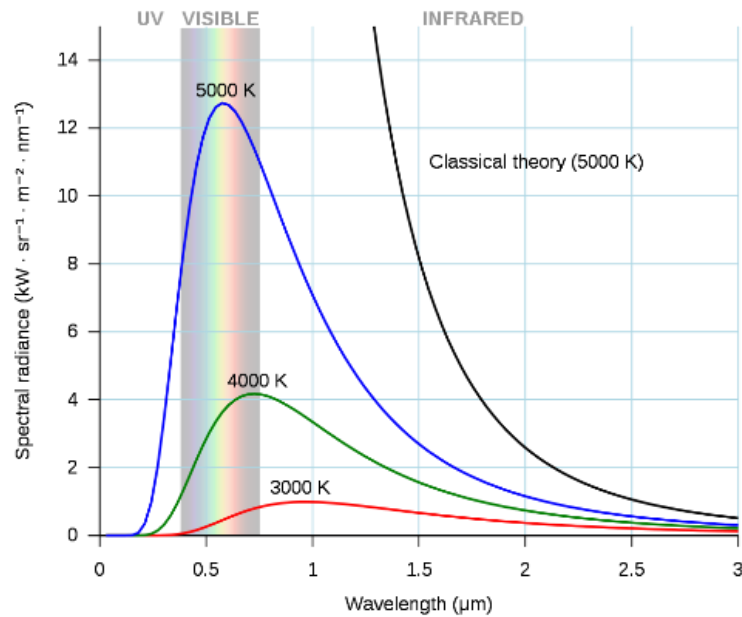
Figure 1.5 Blackbody emission at different temperatures. As temperature increases, emission intensity increases at every single wavelength, and the peak emission intensity wavelength shift to a shorter wavelength.

1.2.2 Kirchhoff's radiation law

In heat transfer, Kirchhoff's law of thermal radiation refers to wavelength-specific radiative emission and absorption by a material body in thermodynamic equilibrium, including radiative exchange equilibrium. Kirchhoff's law states that: For an arbitrary body emitting and absorbing thermal radiation in thermodynamic equilibrium, the emissivity is equal to the absorptivity [12].

A simple case can be used to roughly prove the Kirchoff's law. As shown in Fig. 1.6, imagine two parallel plates, one, which is a blackbody surface and the other one is gray. Two plates are at the same temperature, and there is no heat transfer between these systems and the outside environment. Therefore, there is a zero net energy transfer

between the blackbody and the gray body, i.e., energy transfer from left to right equals to the one in the opposite direction.

$$E_b(T) = (1 - A)E_b(T) + \varepsilon E_b(T)$$

W

h

e

r   =

e

E_bT is the energy transfer from the blackbody to the gray body, A and ε are absorptance and emittance of the gray body. The left side equals to the right side for the thermal equilibrium condition. Therefore, we can confirm that,

Kirchhoff's law has another corollary: the emissivity cannot exceed one (because the absorptivity cannot, by conservation of energy), so it is not possible to thermally radiate more energy than a black body, at equilibrium. In negative luminescence the angle and wavelength integrated absorption exceeds the material's emission, however, such systems are powered by an external source and are therefore not in thermodynamic equilibrium.

From the Kirchhoff's law, one can draw a conclusion that "a wavelength-selective absorber in mid-infrared range can be used as a wavelength-selective thermal emitter at elevated temperature", which provides a rule to design a wavelength-selective thermal emitter [13]. Thus, in order to design a narrowband thermal emitter, instead of simulating the complicated thermal emission property, the optical response under an incident light with the same wavelength range is the thing which needs to be considered.
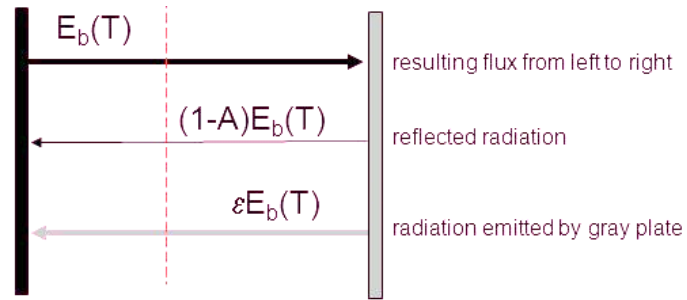
Figure 1.6 Schematic diagram of a thermodynamic equilibrium system consisting a blackbody plate and a gray body plate.

1.2.3 Wavelength-selective thermal emitter in mid-infrared range in 1D configurations

The mid-infrared (mid-IR) spectral range, where materials exhibit characteristic molecular absorption fingerprints originating from the intrinsic vibrational modes of chemical bonds, is crucial for bio-sensing and gas detection. Conventional mid-infrared spectroscopy devices rely on broadband blackbody light sources with bulky gratings or dispersion system in order to obtain spectrally resolved information. Miniaturized spectral selective emitters would allow for the design of spectroscopic devices without dispersive elements, drastically reducing their size and complexity.

According to Kirchhoff's law, a narrowband absorber in mid-IR range can serve as a wavelength-selective thermal emitter at elevated temperature. Therefore, as perfect absorbers, TP based one-dimensional structures could also be suitable for wavelength-selective thermal emission applications. To design a TP-based thermal emitter for mid-infrared range, people can consider from three aspects: choosing DBR and the metal materials, choosing DBR configuration, and optimizing the structure for a near-unity and narrow bandwidth property.

To choose materials for the DBR, one should choose a pair of dielectric materials with large refractive index contrast for a wide stop band and a good reflection ability. Usually, inorganic compounds, like SiO_2, exhibit low indices (~1.4), while pure semiconductors like Si and Ge have high indices (~3.4 and ~4.1, respectively). As a result, for a high-quality DBR, combinations of Si-SiO_2 or Ge-SiO_2 are usually chosen to comprise the DBR. Notice that for SiO_2, three major absorption bands can be observed at wavelength beyond 5 μm due to the resonance of Si-O-Si vibrations, which will induce loss broadening the emission peak in spectrum [14]. Therefore, to exhibit the full wavelength-selectivity of the structure, the central wavelength is usually designed less than 5 μm. In order to avoid large metal-induced loss, noble metals like Ag, Au and Al are good candidates. Also, for operating at elevated temperatures, a metal with high melting point and thermal stability should be considered. Therefore, Al and Ag may not be suitable for their relatively low melting points (for Al, the melting point is only 660 ℃) and poor thermal stability (Ag is easily oxidized by O_2 and N_2, especially under elevated temperatures) [15,16].

As discussed in Section 1.1.3, TP structures can have two possible configurations, i.e., metal-on-top and metal-at-bottom. It has been reported that, for mid-IR range, optical behaviors can be different. As demonstrated in Ref. [17], two types of TP structures having the same 4 μm resonance are compared. Figure 1.7a shows the metal-side TP structure with a thin metal film, while the DBR-side TP structure with an opaque metal film is seen in Figure 1.7d. A 5-layer Si/SiO_2 DBR, adjacent to Al films, was chosen to form the TP structures. As shown on the right side of Figures1.7, the DBR-side TP provides a 10 times narrower reflectance dip bandwidth compared to the metal-side TP. This drastic difference in behaviors was explained as more loss induced in the TP

structure with the thin metal layer on top. As a conclusion, the TP structure with a configuration of thick metal on bottom could be better choice to achieve a narrow bandwidth.

After choosing the materials and the configuration, the optical behaviors of the TP structure needs to be optimized. Similar as a normal optical cavity, the critical coupling condition and quality factor are the two basic rules which needs to be concerned and followed [18-20].

For a near unity absorptance value, we design the structure by considering the critical coupling condition. Critical coupling conditions can be used to evaluate the coupling efficiency between a waveguide and a resonator (e.g., ring or disk resonator). As shown in Fig. 1.8(a), in the waveguide and resonator system, For the harmonic time dependence of *exp(-iωt)*, the temporal normalized mode amplitudes *a* of the resonator can be described as

$$\frac{da}{dt} = (-i\omega_0 - \kappa_e - \kappa_o)a + e^{i\theta}\sqrt{2\kappa_e}S_{in}$$

where ω_0 represents the resonance frequency of the resonator, κ_o is the decay rate of the field due to internal loss in the resonator, and κ_e is the decay rate due to the energy escape into the waveguide. θ is phase of coupling efficiency. *da/dt = −iωa*. From energy conservation, the outgoing waves of the resonator can be written as

$$S_{out} = S_{in} - e^{-i\theta}\sqrt{2\kappa_e}a$$

Similarly, the TP structure can also be considered based on the critical coupling condition. Take TP structure with metal at bottom as an instance. As shown in Fig. 1.8, the DBR leakage rate γ and metal loss rate δ correspond to κ_e and κ_o respectively in the above equations. Then, the equations can be written as

$$\frac{da}{dt} = (-i\omega_0 - \gamma - \delta)a + e^{i\theta}\sqrt{2\gamma}S_{in}$$

$$S_{out} = S_{in} - e^{-i\theta}\sqrt{2\gamma}a$$

The absorptance A can be calculated from S_{in} and S_{out}

$$A(\omega) = 1 - R(\omega) = 1 - \left|\frac{S_{out}}{S_{in}}\right| = \frac{4\gamma\delta}{(\omega-\omega_0)^2+(\gamma+\delta)^2}$$

The equation above can have a maximum value when γ = δ. In other words, when the transmission loss of DBR coincident with the absorption loss of the metal mirror, the TP structure will show a near-unity absorptance value.

Besides a near-unity absorptance, the bandwidth of the peak is also critical. In physics and engineering the quality factor or Q-factor is a dimensionless parameter that describes how underdamped an oscillator or resonator is. It is defined as the ratio of the peak energy stored in the resonator in a cycle of oscillation to the energy lost per radian of the cycle. Q-factor is alternatively defined as the ratio of a resonator's central frequency to its bandwidth when subject to an oscillating driving force (here is the incident electromagnetic wave, see Figure 1.6) [21,22]. These two definitions give numerically similar, but not identical, results. Higher Q indicates a lower rate of energy loss and the oscillations die out more slowly. Using Q-factor, we can evaluate the quality of an optical cavity, and the sharpness of absorber/emitter in different works can be compared. For the TP structure with metal at bottom, the Q-factor can be expressed as

$$Q = \omega_{TP}\frac{E}{P} = \omega_{TP}\frac{\tau}{2},$$

where ω_{TP} refers to the TP resonance frequency, E is the stored energy within the structure and P is the leakage power, and the ration between E and P can be expressed by relaxation time τ.

16

$$\frac{1}{\tau} = \gamma + \delta$$

As a result, small values of γ and δ contribute to a large Q-factor.

As shown in Fig. 1.9, for a resonance mode, the light should have a zero phase change after a double reflection loop (after it gets reflected by Au and DBR), i.e., $r_{Au}r_{DBR}$ has a positive real value (the imaginary part is 0). For a critical coupling condition and a large Q-factor, $\gamma \approx \delta \approx 0$, so $|r_{Au}| \to 1$, $|r_{DBR}| \to 1$. Therefore, one needs to design a structure for $r_{Au}r_{DBR} \to 1$.
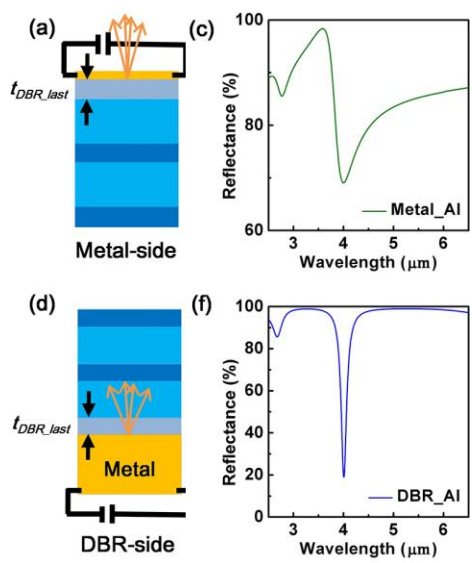
Figure 1.7 Comparison between TP structure with metal on top and metal at bottom.Reprinted with permission, Copyright © 2017 American Chemical Society.
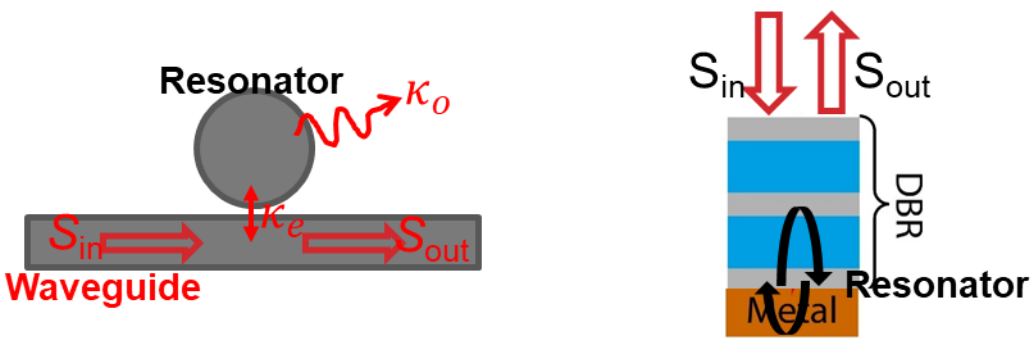
Figure 1.8 Critical coupling condition for a high absorptance.

Figure 1.9 Design principle for $r_{Au}r_{DBR} \to 1$.

1.3 Photodetection through hot carriers in one-dimensional structure

1.3.1 Semiconductor photodetection device (photoconductor)

Photoconductors represent the simplest conceivable type of photodetector: they consist of a finite-length semiconductor layer with contact at each end (Figure 1.10) [23]. A fixed voltage is applied between the two end contacts, in such a way that a bias current flows through the semiconductor layer. The active optical surface is formed from the region between the two collection electrodes. When it is illuminated, the photo-generated changes produced under the effect of the applied electric field lead to a photocurrent which is added to the bias current, effectively increasing the conductivity of the device.

The main point of interest in a photoconducting device is its increased gain, the response of photoconductors being typically several orders of magnitude greater than that of photovoltaic detectors for a given material. On the other hand, its other operational parameters (bandwidth, UV/visible contrast, infrared sensitivity) are generally below that of other types of photodetectors, which often greatly limits the scope of its potential applications.
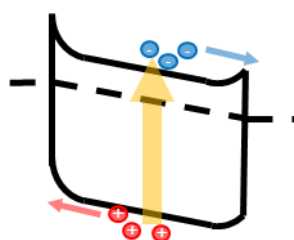
Figure 1.10 Energy band diagram of a photoconductor.

1.3.2 Sub-bandgap photodetection devices using hot electrons

Research on the hot carrier effect dates back to the early twentieth century [24]. Strictly speaking, the earliest experiments were the studies of photoemission, in which the incident photons excite electrons to higher energy states in metal, and the excited electrons with sufficiently high energy (greater than the work function of the metal) are able to escape from the metal into vacuum. Early experiments were mainly conducted in a vacuum chamber to prevent gases from impeding the flow of photoelectrons, and to also prevent the metal from being oxidized. These experiments on photoemission served mainly to understand the light-metal interaction, work function of metals and hot carrier generation and transport properties.

Energetic hot electrons excited through photon absorptionin metals can be extracted via internal photoemission for a number of applications, e.g., photodetection, photovoltaics, photocatalysis, and surface imaging. In terms of photodetection, the hot-electron mechanism enables direct and efficient below-bandgap photodetection, high tunability of the working wavelength by manipulating the structured resonance instead of the materials, and the possibility of room-temperature operation.

Figure 1.11 shows the two basic structures that have been used to generate and collect hot carriers in metals: metal-semiconductor (M-S) structure (left) and metal-insulator-metal (M-I-M) structure (right) [25,26]. Figure 1.11 left shows a n-type band bending, when a n-type semiconductor attaches with metal. In order to balance the Fermi level, electrons will begin to flow from the semiconductor to the metal, and creating a depletion layer, and hence a built-in electric field (band bending). The absorption of photon leads either to the direct generation of hot carriers, or to surface plasmons, which subsequently decay into hot carriers. These carriers will diffuse, and a fraction of them will find their way to the dielectric or semiconductor. Hot electrons having energy higher

than the energy barrier can traverse the interface enter into the semiconductor. The bended conductive band drives the electron, forming photocurrent even without bias. For semiconductor with low conductivity or insulator, M-I-M structure is usually utilized. The insulator layer needs to be thin (~ 20 nm) to guarantee a small carrier loss during traveling through the insulator film. Note that the hot electron can generate in metals on both sides, and a net current will flow based on the absorption profile within each metal and on the voltage established by the energy barrier for carriers to travel from one metal to the other.
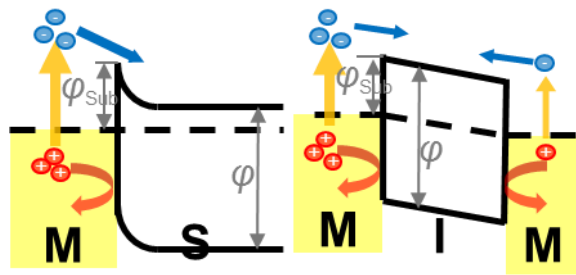
Figure 1.11 M-S Schottky diode (left) and M-I-M hot electron device (right).

1.3.3 Design of one dimensional wavelength-selective hot carrier photodetector

Indeed, due to the lack of effective light-trapping mechanisms, direct illumination on a metal film is usually not very efficient. Surface plasmons (SPs) provide an interesting solution because they can strongly localize the photon energy within a deep-subwavelength region where extensive hot electrons can be generated. Similarly, light can be highly confined along the metal/DBR interface in the region around the metal/dielectric interface, allowing for strong absorption by the metallic layer, which could contribute to an enhanced generation of hot carriers. Considering two types of TP structures and two types of HE devices, there are 4 possible configurations for TP-based wavelength-selective hot electron photodetectors, as depicted in Figure 1.12. High-

reflectivity, stable and high-conductivity metals like Au should be good choices as the metal. Instead of using bulky well-crystallized and concisely doped semiconductor like Si substrate, the semiconductor needs to be deposited as a layer in the structure. Therefore, some metal-oxide semiconductor with naturally n-doped, like ZnO and TiO_2, can be used.

For the devices with metallic films underneath the DBR (two devices on the right side), the metal sustains the multilayers with large internal stress, and due to a poor adhesion between dielectric and metal, the whole structure may not be stable after fabrication. As a means to improve adhesion, the structure can be deposited reversely on the substrate, and incident light launches from the backside of substrate. However, for the photoresponse measurement, a strong noise will be induced owing to interference effect of the substrate. For the case of M-S device on top of the DBR, in order to have a larger photoresponse, the semiconductor layer should be around 100 nm and be doped above a certain level for a good conductivity. However, a metal-oxide semiconductor, e.g. TiO2, exhibits higher absorption loss as the doping level increases. A higher doping concentration will introduce a larger absorption loss, hinder the wavelength-selectivity of the device. MIM device on top seems to be the best choose among them. However, in MIM device, hot electrons can generate from both metal films, which may reduce the net current. Therefore, some strategies need to be employed to make a dominated generation of hot electron from one metallic film.
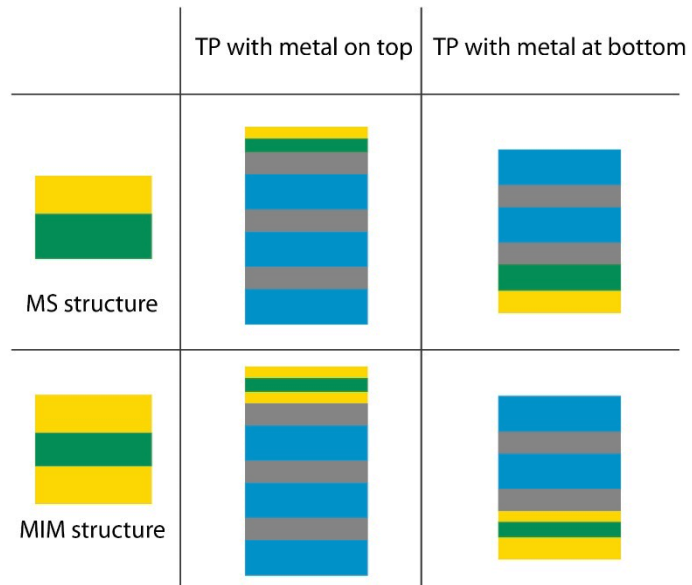
Figure 1.12All possible configurations of TP-based wavelength-selective hot electron photodetectors

References

1. Weisbuch, Claude, et al. "Observation of the coupled exciton-photon mode splitting in a semiconductor quantum microcavity." Physical Review Letters 69.23 (1992): 3314.

2. Gérard, J. M., et al. "Enhanced spontaneous emission by quantum boxes in a monolithic optical microcavity." Physical review letters 81.5 (1998): 1110.

3. Tohmori, Yuichi, et al. "Broad-range wavelength-tunable superstructure grating (SSG) DBR lasers." IEEE journal of quantum electronics 29.6 (1993): 1817-1823.

4. Sheppard, C. J. R. "Approximate calculation of the reflection coefficient from a stratified medium." Pure and Applied Optics: Journal of the European Optical Society Part A 4.5 (1995): 665.

5. Osting, Braxton. "Bragg structure and the first spectral gap." Applied Mathematics Letters 25.11 (2012): 1926-1930.

6. Kavokin, A. V., I. A. Shelykh, and G. Malpuech. "Lossless interface modes at the boundary between two periodic dielectric structures." Physical Review B 72.23 (2005): 233102.

7. Goto, T., et al. "Optical Tamm states in one-dimensional magnetophotonic structures." Physical review letters 101.11 (2008): 113902.

8. Kaliteevski, M., et al. "Tamm plasmon-polaritons: Possible electromagnetic states at the interface of a metal and a dielectric Bragg mirror." Physical Review B 76.16 (2007): 165415.

9. https://en.wikipedia.org/wiki/Black_body

10. Planck, M. (1914). The Theory of Heat Radiation. Masius, M. (transl.) (2nd ed.). P. Blakiston's Son & Co. OL 7154661M.

11. https://en.wikipedia.org/wiki/Thermal_radiation#cite_ref-1

12. Planck, Max. "On the law of the energy distribution in the normal spectrum." Ann. Phys 4.553 (1901): 1-11.

13. https://slideplayer.com/slide/4364210/

14. Kischkat, Jan, et al. "Mid-infrared optical properties of thin films of aluminum oxide, titanium dioxide, silicon dioxide, aluminum nitride, and silicon nitride." Applied optics 51.28 (2012): 6789-6798.

15. McWhan, D. B., B. B. Cunningham, and J. C. Wallmann. "Crystal structure, thermal expansion and melting point of americium metal." Journal of Inorganic and Nuclear Chemistry 24.9 (1962): 1025-1038.

16. Cunningham, B. B., and J. C. Wallmann. "Crystal structure and melting point of curium metal." Journal of Inorganic and Nuclear Chemistry 26.2 (1964): 271-275.

17. Yang, Zih-Ying, et al. "Narrowband wavelength selective thermal emitters by confined tamm plasmon polaritons." ACS Photonics 4.9 (2017): 2212-2219.

18. Haus, Hermann A., and Weiping Huang. "Coupled-mode theory." Proceedings of the IEEE 79.10 (1991): 1505-1518.

19. Lu, Hua, Xueming Liu, and Dong Mao. "Plasmonic analog of electromagnetically induced transparency in multi-nanoresonator-coupled waveguide systems." Physical Review A 85.5 (2012): 053803.

20. Li, Hongju, et al. "Total absorption of light in monolayer transition-metal dichalcogenides by critical coupling." Optics express 25.25 (2017): 31612-31621.

21. Harlow, James H. Electric power transformer engineering. CRC press, 2003.

22. Tooley, Mike. Electronic Circuits-Fundamentals & Applications. Routledge, 2007.

23. Lawton, R. A., and A. Scavanne. "Photoconductive detector of fast-transition optical waveforms." Electronics Letters 11.4 (1975): 74-75.

24. Takeda, Eiji, Cary Y. Yang, and Akemi Miura-Hamada. Hot-carrier effects in MOS devices. Academic Press, 1995.

25. Kim, Sunkook, et al. "Low‑power flexible organic light‑emitting diode display device." Advanced Materials 23.31 (2011): 3511-3516.

26. Krishnan, S., et al. "Design and development of batch fabricatable metal–insulator–metal diode and microstrip slot antenna as rectenna elements." Sensors and Actuators A: Physical 142.1 (2008): 40-47.

2. Wavelength-selective thermal emission with modified DBR structures

2.1 Introduction

The mid-infrared (mid-IR) range is very useful for chemical and biomedical sensing, because most gases and liquids have absorptions characteristic of their molecular vibration modes in this range [1-3]. However, in order to obtain spectrally resolved information, conventional mid-IR spectroscopy devices use broadband light sources with bulky gratings, which hinders their miniaturization. Narrowband and wavelength-tunable mid-IR light sources enabling portable and low-cost molecular spectroscopy devices (Figure 2.1) have been attracting extensive interests. Simple semiconductor structures such as light-emitting diodes (LED) based on inter-band transitions have a very low efficiency in the mid-IR. Since the radiative decay time of the electron is proportional to λ^3 and becomes longer than non-radiative decay times, non-radiative processes become predominant when λ increases and the LED radiative efficiency decreases accordingly. More sophisticated semiconductor devices, such as quantum cascade lasers (QCLs) based on inter-subband transitions, are powerful sources that operate at RT for wavelengths at mid-IR range. However, QCLs are fabricated with an epitaxial growth technique that is relatively expensive [4]. As a result, for a narrowband light sources in mid-IR range, incandescent sources (thermal emitter) are still the best candidate, not only in terms of cost, but also in regards to the absolute power whenever broad spectral features are considered.

During the last decade, a large variety of narrowband mid-IR thermal emitters

have been investigated: quantum well/photonic crystal-based thermal emitters [5-7], and SP-based thermal emitters [8-12], and TP-based thermal emitters [13,14]. The quantum well/photonic crystal-based thermal emitters can realize relatively narrowband emission in the mid-IR regime (Q-factor of emittance peaks can be larger than 100); however, their fabrication requires high-cost epitaxial growth techniques and the performance is highly related with the semiconductors quality which hinder their wide-spread applications. SPs, which are coupled electromagnetic field oscillations and collective electron oscillations at metal/dielectric material interfaces, have been applied to enhance the properties of narrowband thermal emitters using subwavelength nanostructures. There are two main types of conventional SPs, namely, surface plasmon polaritons (SPPs) and localized surface plasmon resonances (LSPRs). For real devices based on SPPs, the strong angular dependence of SPPs will induce an average effect within range of collection angles and the loss of metal will increase as temperature rises. Therefore, the SPP-based thermal emitters cannot reproduce sharp emittance peaks as simulations. The thermal emission from LSPR mode can exhibit an angular-independence and near-unity emittance, and but the emission bandwidth is relatively broad (with a Q-factor around 10) [10-12]. As a result, the realization of a low-cost yet high-intensity narrowband thermal emitter in mid-IR range still remains a challenge.

In 2005, a type of surface wave formed at the interface between two dielectric distributed Bragg reflectors (DBRs) with overlapping stop bands, known as an optical Tamm state (OTS), was demonstrated [15]. In 2007, a class of OTSs, Tamm plasmons (TPs), were proposed to exist at the interface between a DBR and a metallic film [16]. In contrast to OTS structures, which have high transmission, TP-structures can efficiently absorb incident light within their metal film resulting in a strong and sharp absorption

28

peak. As the in-plane wave vector of Tamm plasmons is smaller than the free space wave vector, TPs can be excited from free space in a one-dimensional (1D) structure without the need for additional nanostructures to couple light. This allows lithography-free fabrication of Tamm plasmon devices. Using a TP structure configuration (i.e., a dielectric DBR on a metallic film) several narrowband thermal emitters with multilayer structures have been proposed. In 2017, a TP structure consisting of a Si/SiO$_2$ DBR on top of a thick metallic film was applied as a thermal emitter [14]. In order to realize both strong and sharp emittance peaks, the number of DBR layers was optimized for different metals to achieve optical impedance matching (i.e., minimized reflection) at the interface of the DBR and the metal, resulting in a structure with a five-layer Si/SiO2 DBR and an Al film that had a strong emittance of 0.90 and a high resonance quality factor ($Q \sim 30$). Besides, the work also discussed about the comparison between two configurations of TP structure and refers that the latter is better due to a less material loss. The work paves a way for further study in TP-based thermal emitter. Later on, along the way of TP based structure, many designs have been reported in order to further improve the Q-factor of a thermal emitter. In 2018, we report that inserting an SiO$_2$ optical cavity between a Ge/SiO$_2$/Ge DBR and an Au film of a TP structure can drastically improve the Q from 22 to 88 [17]. In the same year, optical cavity consists DBR bilayer was reported to achieve a Q over 100 [18]. In 2019, another group used machine learning method to optimize a Ge/SiO$_2$ DBR on a W film and was able to achieve a Q-factor as high as 188 [19], which is already the largest Q-factor to date. These results indicate that, in addition to having a large-area and lithography-free fabrication process, TP-based thermal emitters also boast superior optical performance with narrow bandwidths of thermal emission. For real applications, a sharper emission peak gives a better spectral resolution, which is always required for

the bio-sensing proposes.

In this section, we show the strategies to improve the Q-factor of TP-based devices by modifying the DBR structures. A two-order improvement is achieved in terms of Q-factor, and the mechanisms behind are discussed. Surprisingly, the structure possesses a near-one-thousand Q value can exhibithigh sensitivity to the change of materials' properties with temperature, and by taking advantage of thermo-optical effect, the thermal emitter can exhibit an active wavelength-tunability controlled by the operating temperature. These results not only provide new insights for design of narrowband thermal emitters, not also help to develop high-performance and portable infrared light source systems for spectroscopy devices.
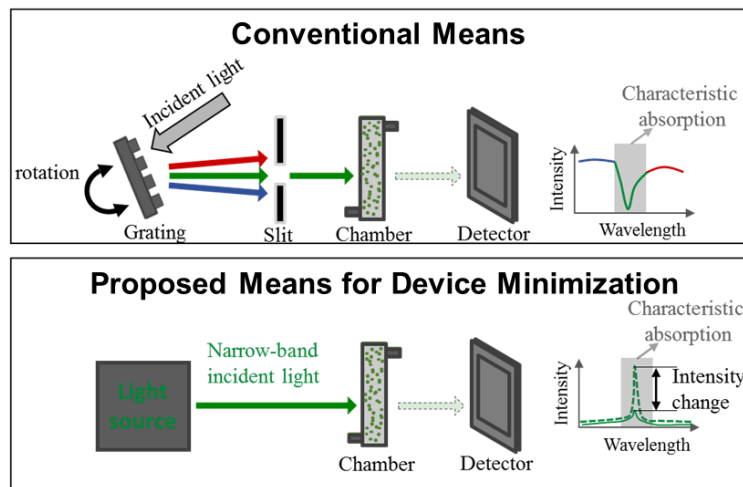
Figure 2.1 Narrowband and wavelength-tunable mid-IR light sources enabling portable and low-cost molecular spectroscopy devices. In conventional devices, broadband light sources and bulky optical gratings is employed for separate light into different wavelength, but the system is complicated and high-cost. The proposed strategy is using narrowband light sources (array) at different wavelengths, and thus the grating system can be eliminated which will simplify the device.

2.2 Methods for simulation, fabrication and measurement

The simulated reflectance, absorptance, and transmittance spectra, and the near-field electric field magnitude distributions are computed using rigorous coupled-wave analysis (DiffractMOD, Rsoft Design Group, Ossining, USA). The results for $r_{DBR}r_m$ as a function of wavelength were calculated using the transfer-matrix method using a MATLAB script. The complex permittivities of metals are described by the Drude-Lorentz dispersion model. The refractive indices of Ge and SiO_2 are modelled according to literature values.

The multilayer samples were fabricated using an RF-magnetron sputtering system (CFS-4ES, Shibaura Engineering Works Co., Ltd., Yokohama, Japan). To increase the adhesion between metal and dielectric, 5-nm adhesion layers such as Ti and Cr can be used at the interface to enhance the stability of the structure. A continuous deposition process without breaking the vacuum will guarantee a good adhesion. For the sample with total thickness larger than 5 µm, an annealing process is recommended to reduce the internal stress, but notice that annealing may also change the homogenous of the thickness along large surface.

Reflection and emission spectrum measurements were operated using an FT-IR spectrometer (VIR-300, JASCO, Tokyo, Japan). Schematic diagram of reflectance measurement setup is shown in Fig. 2.1. First, infrared light can be produced from the infrared source (broadband ceramic heater), and reaches an interferometer, consisting of a beam splitter and two mirrors. A spatial filter consisting of two concave mirrors and an aperture is employed to obtain a plane wave. Then, infrared light passes through a polarizer, so TM- or TE- polarized light can be obtained. Two rotating mirrors can control

the incident angle to the sample from 0 to 15° with angular resolution of 1°. A beam splitter

is employed, so reflection for near-normal incident angles can reach an MCT detector.

The reflectance is measured as a ratio of reflection spectrum of sample and the

spectrum of incident intensity (the "baseline"). With the setup, the baseline is

approximately measured by put an Au mirror in the position of sample. Due to a not

perfect reflection of the Au mirror (even a perfect flat Au mirror with infinite thickness

cannot reflect 100% of the incident intensity), a calibration is needed. Figure 2.2 shows a

sample reflectance spectrum before (grey solid curve) and after calibration (black solid

curve) with an Au mirror. Unity is indicated with a dashed red line. An Au mirror is used

to obtain the baseline reflection $S_b(\lambda)$ (i.e., spectrum of the incident light to the sample),

and the reflection spectrum of the sample $S_s(\lambda)$ is measured by replacing the Au mirror

with the sample. The reflectance spectrum can be calculated by

$$R(\lambda) = S_s(\lambda)/S_b(\lambda).$$

This initial uncalibrated reflectance spectrum has values above unit, because the Au

mirror does not have unity reflectance. The reflectance spectrum must be corrected by

considering the real Au mirror reflectance, $R_m(\lambda)$. $R_m(\lambda)$was approximated by fitting

the simulated reflectance (inset, red cross) of an Au mirror to a quadratic equation,

$R_m(\lambda) = -0.001387\lambda^2 + 0.01384\lambda + 0.9512$. With this, the calibrated sample

reflectance $R_c(\lambda)$ becomes

$$R_c(\lambda) = S_s(\lambda)R_m(\lambda)/S_b(\lambda).$$

Calibrating the reflectance reduces the reflectance by 1~2%, bringing it below unity to a

physical value. Note that the large noise around the wavelength of 4.25 μm is due to the

influence of CO_2 absorption.

For thermal emission measurement, the sample is heated up using a heating stage (UH200CV, SPLEAD Corp., Tokyo, Japan), and emission from the samples was measured through the external port of the same FTIR spectrometer, as shown in Fig. 2.3. A carbon soot film was deposited on a Si substrate to serve as a blackbody reference. The surface temperature of the hybrid structure was measured using a K-type thermocouple equipped with a surface temperature probe (IK-500, AS ONE Corp., Osaka, Japan), while the temperature of the carbon soot surface was measured using an infrared thermometer (IT-545S, HORIBA Ltd., Kyoto, Japan). The emittance spectrum $\varepsilon(\lambda)$ at temperature T can be calculated by

$$\varepsilon(\lambda, T) = \frac{I_s(\lambda, T) - I_{env}(\lambda, T)}{I_B(\lambda, T) - I_{env}(\lambda, T)}.$$

I_B is the estimated emission intensity of the blackbody, I_s is the measured sample emission spectrum, I_{env} is the environmental emissions corresponding to the measurement of the sample and the blackbody.
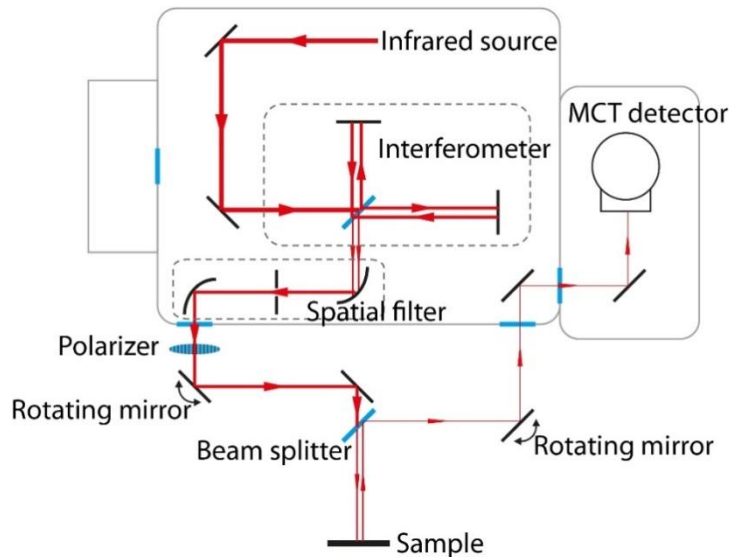

Figure 2.2.
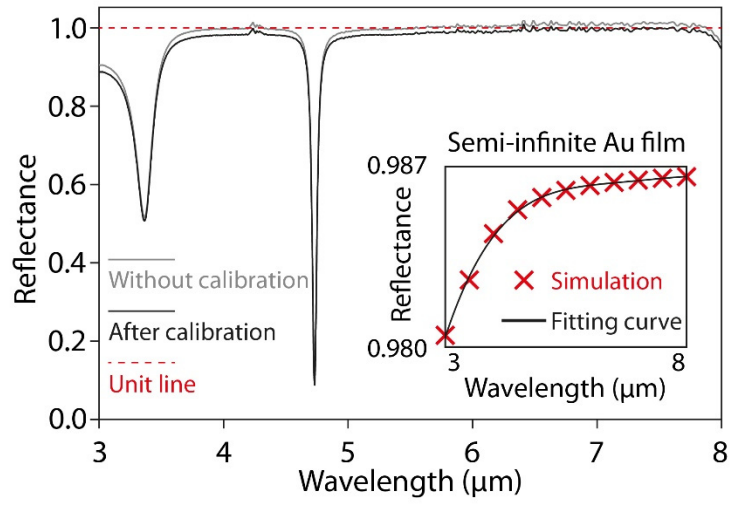
Figure 2.3.
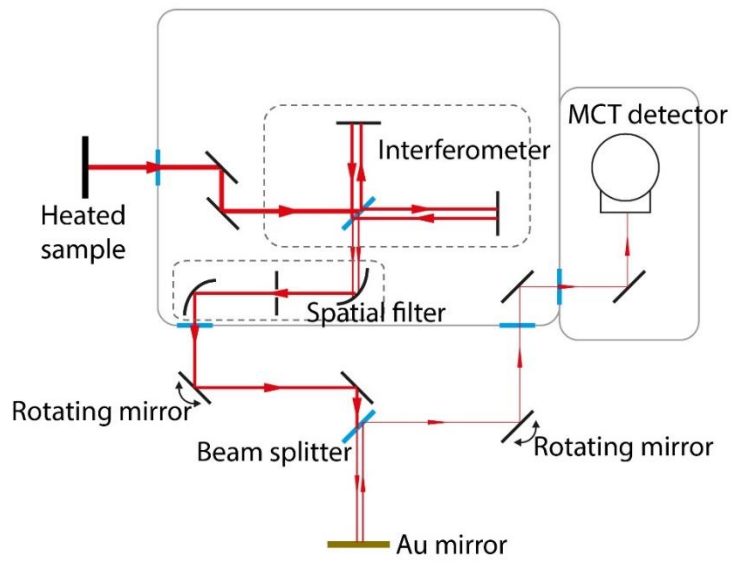
Figure 2.4.

2.3 Improving wavelength-selectivity of TP-based thermal emitters through increasing layer thickness in DBR

As we discussed in Section 1.2.3, for a typical TP structure under impedance matching condition, the Q-factor is only related to the different types of metal, and get limited because of the metal loss. In this section, we propose a means to further improve the wavelength-selectivity of a TP based thermal emitter through increase the thickness of the DBR layer adjacent to metallic mirror. By this way, the TP structure can store more energy without changing the impedance matching condition. As a result, we demonstrate both theoretically and experimentally that this modified TP structure can exhibit the same emittance with a twice enhanced Q-factor.

The structure consisting of an Au film and a Ge/SiO$_2$/Ge DBR with a thick last Ge layer is shown in Figure 2.5(a). The structure is originated from a typical TP structure by increasing of the thickness of the Ge layer, so we name the structure as "modified TP structure". Two-dimensional electric field distributions of the modified TP structure for normal incidence illumination at the resonance wavelength reveals a standing-wave pattern inside the DBR structure (Figure 2.5b). First, we optimize the structure of a typical TP configuration by adding one more pair on top as the upper plot of Figure2.5c. The method will increase the Q-factor (as the τ_{DBR} increases), but it breaks the impedance matching condition resulting in a weaker absorptance. In contrast, increasing the last Ge layer thickness from 280to 874nm results in bandwidth narrowing without the absorptance peak changing at the lower plot of Figure 2.5c. The modified TP structure is therefore expected to exhibit a sharper emittance peak than its corresponding standard TP structure.

To explain the optical behavior of the modified TP structure, its properties are

further investigated by varying the thickness of the last Ge layer. As shown in the inset of Figure 2.6a, t_{Ge} and T_{Ge} are used to represent the thicknesses of the upper and the lower (last) Ge layers, and t_{SiO2} and t_{Au} indicate the thicknesses of the SiO_2 and the Au layers, respectively. For a standard TP structure, the optical thickness of each DBR layer isset to be one-quarter of the targeted emission wavelength(here, $T_{Ge}=t_{Ge}=$ 280 nm, and $t_{SiO2}=819$ nm for the target wavelength of 4.5 μm). The Au film ($t_{Au}=$ 100 nm) on the bottom acts as a mirror with low absorption loss, contributing to the high Q-factor. Figure 2.6a shows the absorptance as a function of incident wavelength and T_{Ge} (other thicknesses are kept constant), where several high absorptance lines, indicating different orders of the TP mode, are observed. The upper plot of Figure 2.6bpicks the absorptance spectra for three different T_{Ge} values (i.e., $T_{Ge}=$ 280 nm, 874 nm, and 1468 nm as shown by the horizontal dashed lines in Figure 2.6a corresponding to the first, second, and third order TP modes. The absorptance peaks of the three spectra have the same value (0.89) at the same wavelength (4.773 μm); the only change observed is a decrease in the bandwidth (corresponding to an increase in the Q-factor from 27to 99). Since Ge is nearly transparent (imaginary part of the refractive index is close to zero) at wavelengths around 5 μm, the intensity of the incident light that can transmit the DBR and reach the DBR/Au interface will not be affected when T_{Ge} is varied. As a result of the same impedance matching condition, TP modes with a similar intensity are excited in the structures with different T_{Ge}. The higher Q-factor for the higher TP mode orders can be explained as a larger stored energy (as shown in Figure 2.6c). The resonance conditions of the TP modes given by Real ($r_{DBR}r_{Au}$) are also plotted in the lower part of Figure 2.6b. The peaks of Real ($r_{DBR}r_{Au}$) corresponds to a zero imaginary part, thus indicating a phase matching between the DBRs and Au mirror which results in a resonance. As the thickness of the last Ge

layer increases, the peak of the Re($r_{DBR}r_{Au}$) curve in Figure 2.6b sharpens, which indicates the resonance condition disappear more quickly for a higher order mode as the wavelength change (i.e. a stricter resonance condition for a higher order mode). This in turn results in a sharperabsorptance peak. It is clear from the absorptance spectra and the near field distributions that higher order TP mode contributes to an increase in the Q-factor of the absorptance peak. However, considering the difficulty of fabricating thick-layer structures, TP structures sustaining second order TP modes are studied throughout the rest of this work.

Now, it is clear that increase the thickness of the last DBR layer can lead to a better wavelength-selectivity. How about increasing thicknesses of layers other than the last DBR layer? Figure 2.7 shows electric field distributions and calculated absorptance spectra with their resonance conditions of four different TP structures. Structure ① represents a standard TP structure ($T_{Ge} = t_{Ge} = 280$ nm), while Structures ②, ③ and ④ represent modified TP structures where t_{Ge}, t_{SiO2} and T_{Ge} are increased to 874 nm, 2590 nm, and 874 nm, respectively. Electric field distributions indicate that Structure ②, ③ and ④ sustain TP mode one-order higher than that of Structure ①, but the absorptance Q-factors of Structures ② and ③ are not as high as that of Structure ④as shown in the upper plot of (b). The higher absorptance Q-factor of Structure ④can be explained by examining the resonance condition the TP mode, which is given by Equation 1 in the main text, and the calculation results are shown in the lower plot of (b). Structure ① shows a broad $r_{DBR}r_{Au}$ peak. From Structure ② to ④, the peak of the $r_{DBR}r_{Au}$ curve becomes narrower, which indicates a stricter resonance condition for the TP, and thus results in a higher absorptance Q-factor. Therefore, increasing the last Ge layer thickness rather than other layers is the most efficient way to increase the Q-factor of a TP structure.

To fully characterize the thermal emitter structure, angular and polarization dependence of the proposed structure were studied. The left and right parts of Fig. 2.8 show simulated absorptance dispersion diagrams of the modified TP structure with $T_{Ge} =$ 874 nm for transverse magnetic (TM-) and transverse electric (TE-) polarized light, respectively. As the incident angle increases, the wavelength of the absorptance peak blue-shifts. In the case of the TM-polarized incident light, the absorptance peak also broadens and decreases in intensity slightly, while the absorptance peak of the TE-polarized incident light sharpens and increases in intensity slightly. For the TM polarization, when changes from normal to about 25° the absorptance shows a decrease of 50% at the wavelength of the normal incidence peak (and the peak wavelength blue-shifts by 47 nm). The wavelength difference of the absorptance peak between TM and TE polarization components remains small (less than 15 nm when incident angle is below 40°).

Both the typical TP and modified TP structures were fabricated. Figure 2.9 shows the measured reflectance spectra of the samples, together with their SEM cross-section images. The reflectance values at the minimum of the reflectance dip are 0.022 and 0.008 for the standard TP structure and the modified TP structure, respectively. The modified TP structure exhibits a smaller full-width-at-half-maximum (fwhm = 86 nm) than that of the standard TP structure (fwhm = 179 nm), showing that increasing the thickness of the last DBR-layer of a TP structure results in a narrower bandwidth. The angular dependence of the modified TP structure's reflectance for near-normal incidence angles was also measured for transverse magnetic (TM-) polarized incident light. As shown in Fig. 2.9b, the initial position of the dip at the wavelength of 4.972 μm in the reflectance spectra blue-shifts by only 1 nm when θ is varied from 0° to 5°. The wavelength blue-shifts by

an additional 6 nm when θ varied was further increased from 5° to 10°. This wavelength shift of 7 nm (from 0° to 10°) is small compared to the peak bandwidth (86 nm), suggesting that the modified TP structure should exhibit a robust emittance peak for near-normal angles. In addition, control over the resonance wavelength of the TP structure was realized experimentally by adjusting the last Ge layer thickness. The measured reflectance spectra for different T_{Ge} are shown in Fig. 2.9c. The reflectance dips show a similar modulation and a red-shift as T_{Ge} increases. The wavelengths of these measured reflectance dips are in good agreement with the simulations, as shown in Fig. 2.9d.

Thermal emission of the structure was measured for the temperature up to 150 °C. A carbon soot film was deposited on a Si substrate to serve as a blackbody reference. Figure 2.10a shows the measured emission spectra for the three modified TP structures with different T_{Ge} together with the emission of the blackbody reference at a temperature of 150 °C. The three TP structures with different T_{Ge} exhibit different emission wavelengths, confirming that the emission wavelength can be controlled by varying the last DBR-layer thickness of the TP structure. The emittance spectrum of the tested samples was calculated as results of normalizing the emission intensity by blackbody emission intensity at a same temperature. Emittance spectra of the three samples at 150 °C together with the measured absorptance spectra, i.e., (1 – reflectance) spectra, are shown in Fig. 2.10b. The calculated emittance of the sample for T_{Ge} = 910 nm reaches about 0.94, with a high Q-factor ($Q = 48$) and a low background emittance in the vicinity of the emittance peak (about 0.01 at the wavelength of 6.5 μm). It is noted that the Q-factor of this structure and the ratio between the emittance peak and the background emittance (about 94) are larger than those of most recently reported SP-based and TP-based thermal emitters. A comparison with the (1 – reflectance) spectra reveals that the

emittance peaks are weaker and red-shifted. This effect can be explained by the increase in the refractive indices of materials of the DBR-layer and thermal expansion at higher temperatures. Finally, the standard TP structure ($T_{Ge} = 282$ nm) exhibits an emittance peak (with a Q-factor of 22) broader than that of the modified TP structures at 150 °C, as shown in Fig. 2.10c.

In summary, by increasing the thickness of the last DBR-layer in a standard TP structure to about three times, a modified TP structure was proposed and investigated numerically and experimentally as a wavelength-selective thermal emitter. The fabricated modified TP structure was found to have a near-unity emittance peak with near-zero background emission in the mid-IR regime, and a Q-factor that exceeds that of most recently reported SP- and TP-based thermal emitters, at temperatures up to at least 150 °C. Moreover, the wavelength of this strong and sharp emission peak was readily controlled by adjusting the last Ge layer thickness, thus permitting fine selection of the emission wavelength. This proposed modified TP structure achieves a Q-factor twice as high as that of a standard TP structure with the same emittance peak value. In contrast to adding more DBR-layers, increasing the last DBR-layer thickness can enhance the Q-factor without degrading the emittance peak value of the TP structure. This means can be utilized not only for improving narrowband thermal emitters, but also for other applications of TP structures in the visible and near-infrared regimes.
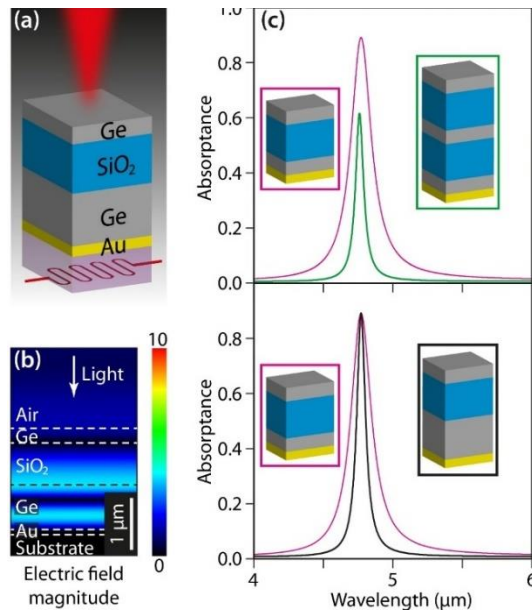
Figure 2.5Characteristics of the modified TP structure. (a) Schematic diagramof using the modified TP structure as a thermal emitter. (b) Normalized electricfield magnitude distribution in the modified TP structure at the resonancewavelength corresponding to the black curve in (c). (c) Simulatedabsorptance spectra.
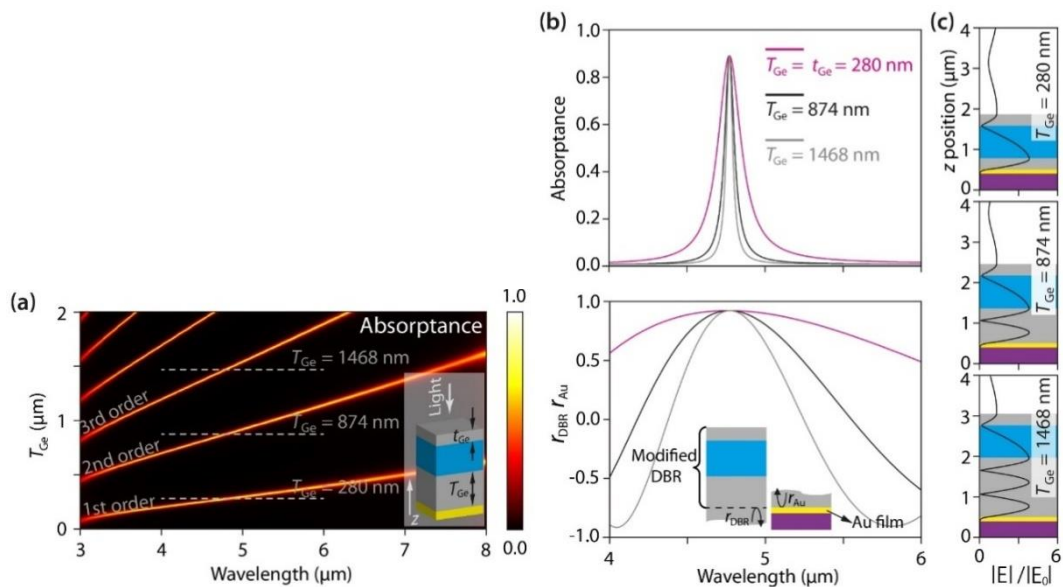
Figure 2.6 Simulation of the TP structure with varying T_{Ge}. (a) The simulated absorptance for varying wavelengths and T_{Ge} with normally incident light. (b) The calculation results of the absorptance spectra and spectra of Re($r_{DBR}r_{Au}$). (c) The simulated normalized electric field magnitude distributions.

41
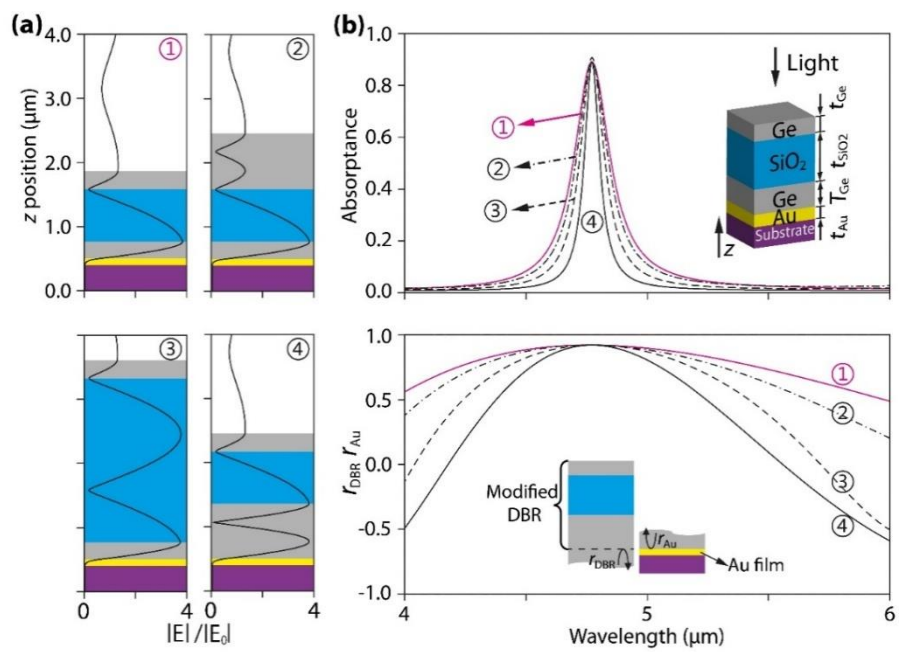
Figure 2.7The results of increasing the thicknesses of the layers other than the bottom layer.
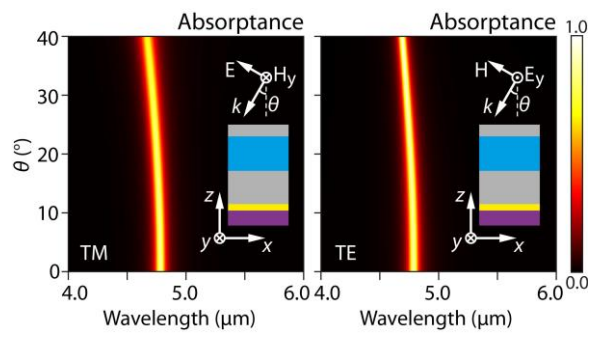
Figure 2.8 Angular and polarization dependence.
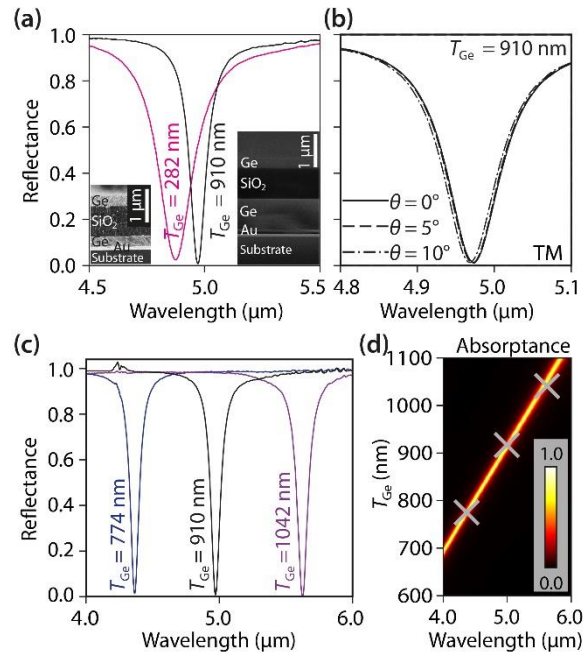
Figure 2.9 Experimental results of reflectance spectra for the typical TP and the modified TP structures.
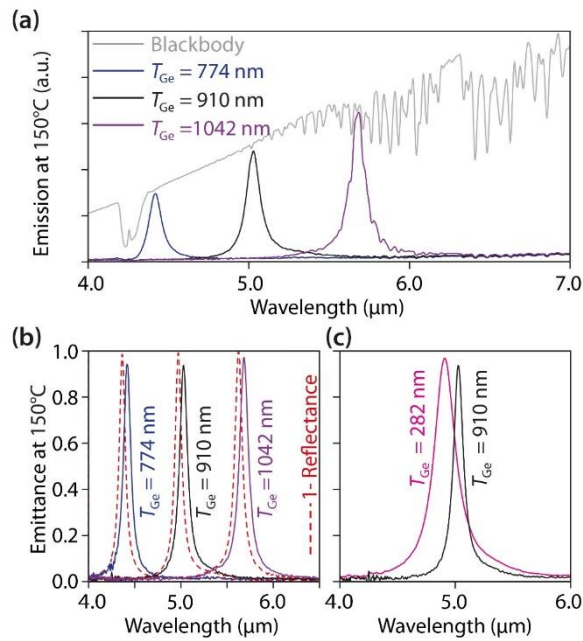
Figure 2.10 Experimental results of emission spectra for the typical TP and the modified TP structures.

2.4 Improving wavelength-selectivity of TP-based thermal emitters through inserting an optical cavity

In this work, we demonstrate another method to optimize wavelength-selectivity from a standard TP structure by inserting an optical cavity between a Ge/SiO$_2$/Ge DBR and an Au film. As shown in the inset of Figure 2.11a, the hybrid structure consists of a SiO$_2$ optical cavity sandwiched between a Ge/SiO$_2$/Ge DBR structure on top and an Au film underneath. The DBR at the top of the structure is made of alternating layers of Ge and SiO$_2$. These two materials were chosen to provide a large refractive index contrast, as a large index contrast results in the DBR having a spectrally wide stop band (about 6.4 μm) and a high reflectance. The thickness of each DBR layer is set to make each layer having an optical thickness of one-quarter the targeted emission wavelength. On the other side of the optical cavity, a highly reflective yet slightly absorbing Au film acts as both the high-temperature source of radiation and one of the cavity mirrors. Since the structure is dedicated to mid-infrared applications, a 100 nm Au layer is thick enough to be opaque for the range of relevant wavelengths. The absorptance spectrum (Fig. 2.11a) reveals a sharp and strong absorptance peak (corresponding to a reflectance dip). The maximum of the absorptance peak is as high as 0.993, and the absorptance peak has a Q-factor of 135. At an off resonance wavelength of 6 μm, the hybrid structure has a low absorptance of 0.002, a value which is even lower than the absorptance of a semi-infinite Au mirror (calculated to be about 0.014 at the same wavelength). Therefore, this structure is expected to show not only a sharp and strong emission peak, but also a low background emission.

Figure 2.11b shows the simulated absorptance under normal incidence as a function of wavelength and cavity thickness (other thicknesses being kept constant). To

the left of Point A, there are some additional weak peaks resulting from leaky TP resonances in the side bands of the DBR. If an optical cavity is inserted between the DBR and the Au film, the TP mode resonance condition equation must be revised to consider the phase change of the light as it propagates one round trip in the cavity. As t_{cavity} is increased from zero, the wavelength for this new hybrid resonance condition red-shifts as can be seen to the right of Point A in Figure 2.11b. The phase shift induced by the cavity thickness makes it possible to select the wavelength of the resonance through changing the cavity thickness. In addition to the TP resonance of the structure, the cavity has its own resonance modes described by $t_{\text{cavity}} = m\lambda/2n_{\text{SiO2}}$. When the cavity thickness is increased sufficiently enough to excite one of these modes within the stop band of the DBR, a coupled TP-cavity resonance that results in strong constructive interference within the cavity and a large absorptance (Point B) is obtained. The three white dashed curves indicate conditions for different orders of the cavity modes, as described by cavity resonance equation. It is evident from the good overlap between the strong absorptance lines and the cavity modes, as shown in Figure 1b, that the high absorptance is a result of a strongly coupled TP-cavity mode.

The near-field behavior of the hybrid structure is investigated at five points (Points A−E in Figure 2.11b). Points B, C, and D have the same cavity thickness as each other ($t_{\text{cavity}} = 1972$ nm), corresponding to the thickness used in Figure 1a; and Points A,B, and E have the same wavelength as each other. Point A, in which no SiO_2 cavity is present, represents a standard TP resonance within the stop band of the DBR. The electric field distribution at Point A, shown in Figure 1c, reveals a standing-wave pattern inside the DBR with an antinode at the upper side of the DBR and a node at the lower side. The electric field intensity has a maximum at the first Ge/SiO_2 interface and decays toward

both the Au film and the Ge/air interface. In contrast to the TP resonance of Point A, a bare DBR at the same incident wavelength possesses a node at the upper side and an antinode at the lower side of the DBR, and the electric field decreases going from the upper side to the lower side, as shown in the inset for Point A in Figure 1c. The difference in phase between the bare DBR and the TP mode is related by the excitation of the TP, and allows the DBR to transmit light to the DBR/Au interface despite its normal mirror-like reflectance.

By inserting an optical cavity into the TP structure of Point A, the hybrid structure of Point B can be obtained. The strong resonance at Point B is a result of the coupling between the TP mode and the first order mode of the cavity (m = 1), as suggested by the similarity between the resonance dispersion and the mode dispersion (Figure 1b). The electric field distribution of Point B (Figure 1c) has, in addition to the standing-wave pattern inside the DBR typical of a TP mode, a very pronounced standing-wave pattern in the cavity. This allows energy to be trapped in the cavity, and results in a high absorptance peak Q-factor of 135 at Point B. This high Q value compares favorably with the $Q = 34$ obtained for the pure TP at Point A. Point C represents the properties of the background of the absorptance spectrum in Figure 1a and has a low absorptance and a high reflectance. The electric field distribution of Point C reveals the DBR behaving as a mirror (node at the top and antinode at the bottom). This means that most of the light is reflected back at the top layer of the DBR and is not absorbed in the Au. A portion of the light that is transmitted through the DBR is reflected by the bottom Au layer, and a very low intensity standing-wave between the DBR and the Au film is seen. The constructive interference between the light reflected by the different interfaces results in Point C having a reflectance larger than even an opaque Au mirror. Points D and E both exhibit a

second order standing-wave within the cavity as a result of the fact that they are both along the resonance line formed by the coupling of the second order cavity mode and the TP mode. Point D, however, has a much lower intensity, because Point D lies at the edge of the DBR stop band, where the DBR reflectance is imperfect. Here, the coupled TP-cavity mode is leaky, and as such the resonance is weak and broad. In contrast to Point D, Point E falls within the DBR stop band and the coupling condition can be fulfilled (see Figure S1). This results in Point E having a high absorptance and cavity modes is also clearly observable in Figure 1c for Point E, where a second order standing-wave pattern with a large intensity is observed. The Q-factor of the coupled mode can be increased by using higher orders of the cavity mode, but to simplify the fabrication process, the coupled mode around Point B is studied throughout the rest of this work. It is noted that by varying the thickness of the cavity, the wavelength of the strong coupled mode can be adjusted between 4.0 and 7.5 μm, as seen in Figure 1b. Therefore, the hybrid structure makes it possible to obtain a resonance wavelength in a wide range of wavelengths simply by adjusting the optical cavity thickness. It is envisaged that electro-optical materials could be used to control the effective optical thickness of the cavity and achieve a tunable emitter.

For structures used in narrowband thermal emission, angular and polarization dependence should be characterized. The simulated absorptance spectra for different incident angles of transverse magnetic (TM-) polarized light are shown in Figure 2a. For TM-polarized incidence, resonance wavelength shifts 8 nm for θ increasing from 0 to 5°. When the incident angle changes from normal to about 8°, the absorptance shows

a decrease by 50% at the wavelength of the normal incidence peak (and peak wavelength blue-shifts by 20 nm). The wavelength difference ($\Delta\lambda$) between the absorptance peaks of

the TM and the transverse electric (TE) polarizations for varying θ is shown in Figure 2b. From this, it is clear that the absorptance peaks for TM- and TE-polarized light exhibit very little wavelength difference as θ varies from 0° to 30° (the difference is within 2 nm).

In Figure 2.13, the absorptance spectra of two hybrid structure designs are compared to the absorptance spectra of TP structures and Fabry−Perot cavities. Figure 3a shows the absorptance spectra for a TP structure with a 3-layer Ge/SiO$_2$DBR and a 5-layer Ge/SiO2 layer DBR, where the high-index Ge layer is in contact with the Au film as necessary to meet the TP resonance condition. The 3-layer DBR corresponds to the same hybrid structure studied in Figure 1b when t_{cavity} is zero. From Figure 2.13a, it is evident that the absorptance peak bandwidth shrinks as an addition DBR period is added; however, the intensity of the absorptance peak diminishes. The 5-layer DBR has a lower transmittance, which allows light to be effectively confined in the TP mode and contributes to the structure having a higher Q-factor. The reduced absorptance intensity is a result of the reduced coupling of the incident light to the TP mode at the DBR/Au-film interface. For the TP to be excited, incident light must penetrate through the DBR and reach the DBR/Au-film interface. Since the TP mode is within the stopband of the DBR, the incident light is initially reflected at the DBR/Air interface and only propagates in the DBR as an evanescently decaying wave. As the thickness of the DBR is increased by adding an additional period, the intensity of light that can reach the DBR/Au-film interface and excite the TP mode is also reduced. This results in less light being coupled from free space to the TP mode and a smaller TP absorptance peak for the structure.

Figure 2.13b shows the absorptance spectra for a Fabry−Perot cavity structure with different thicknesses for the top Au layer. The thicknesses of the cavity and the bottom Au layer are kept constant and are $t_{\text{cavity}} = 1972$ nm and $t_{\text{Au}} = 100$ nm, respectively

(the same as the hybrid structure for Point B of Figure 1b). As the top Au layer thickness is increased, the resonance bandwidth and intensity become smaller. A thicker Au top layer has a higher reflectance, which improves the light confinement and results in a higher Q-factor, but since the Au layer transmittance is lower, less light can enter the cavity and resonate, resulting in a smaller absorptance. For this reason, it is difficult to obtain a Fabry−Perot cavity that has both a large absorptance peak and a small bandwidth. The absorptance spectra for a hybrid structure with a 3-layerDBR and a hybrid structure with a 5-layer DBR are shown in Figure 2.13c. Both hybrid structures exhibit an absorptance spectrum similar to the TP structures, suggesting that the absorptance is related with the TP resonance; however, their absorptance peaks are narrower than both the TP structuresand the Fabry−Perot structures. The coupling of the cavity and TP mode in the hybrid structure results in a more stringent excitation condition for the coupled mode, and thus, a sharper resonance. Moreover, the Q-factors of the hybrid structures are enhanced over the TP structures as a result of the cavity's ability to store a large amount of energy.

The TP-cavity hybrid structure was fabricated. The dimensions of the fabricated structure were measured by scanning electron microscopy (SEM) as t_{Ge} = 298 nm, t_{SiO2} =982 nm, t_{cavity} = 1693 nm, and t_{Au} = 106 nm, and the inset to the right of Figure 2.14a shows the SEM cross-section image of the fabricated structure. The measurements were performed with a spectral resolution of 4 cm^{-1}. The measured and simulated spectra are in good agreement, as shown in Figure 2.14a. The measured reflectance spectrum shows a dip at a wavelength of 4.733 μm, with a full width at half-maximum (fwhm) of 45nm, a Q-factor of 104 (simulated Q-factor with fabricated dimensions is 122), a dip value of 0.085, and a near unity background reflectance (0.991 at a wavelength of 6 μm). The

reflectance spectra of the hybrid structure for near-normal incidence angles were measured with TM-polarized incident light. As shown in Figure 4b, the initial position of the dip at the wavelength of 4.733 μm in the reflectance spectra shifts by only 6 nm when θ is varied from 0° to 5°. The peak shifted an additional 10 nm when θ varied was further increased from 5 to 10°. In order to verify that the coupled TP-cavity mode performs better than a pure TP mode, a TP-based structure with a Ge/SiO2/Ge DBR on an Au film was also fabricated and characterized. The dimensions of the fabricated TP structure are different from those of the hybrid structure due to minor fabrication problems. The measured reflectance dip of the TP structure has a Q-factor of 27 under normal incident light. The reflectance spectra of the TP structure and the hybrid structure, as seen in Figure 2.14c, clearly show that the hybrid structure possesses a much narrower bandwidth than the pure TP structure. The structure whose reflectance spectrum is shown in Figure 2.14a showed a strong and narrow reflectance dip, and it is expected that this peak will give rise to a narrowband and high-emittance peak in the structure's emittance spectrum. To measure the thermal emission of the TP-cavity hybrid structure, the sample was heated up to 150 °C.

Figure 2.15a shows the measured emission spectrum of the hybrid structure for a surface temperature of 150 °C, together with the emission spectrum of the carbon soot layer (blackbody reference) at the same temperature. The emittance spectrum of the tested sample can be calculated from its measured emission spectrum using a normalization procedure with the blackbody spectrum as a reference. Emittance spectra of the hybrid structure at different surface temperatures (50, 75, 100, 125, and 150 °C) are shown in Figure 2.15b. The absorptance spectrum for the sample at room temperature, (1 - reflectance), is also shown for comparison. The calculated emittance of the sample for a

temperature of150 °C reaches up to 0.90 at 4.731 μm, with a Q-factor as high as 88 and a low background emittance (about 0.02 at wavelength of 6 μm) in the vicinity of the emittance peak. The ratio between the emittance peak and the background emittance (about 45), and the Q-factor of this structure are larger than any other values reported for SP-based thermal emitters, including TP-based thermal emitters. The peak in the emittance spectrum is found to be slightly weaker and broader than the observed absorptance peak at room temperature, and the background of the emittance spectrum is found to be slightly stronger than the observed absorptance spectrum. These slight deviations from the observed absorptance are attributed to the averaging of the emittance spectrum over the FT-IR collection angle (±8°) and to the increased loss factor of the Au and SiO2 layer at elevated temperatures. As the surface temperature decreases from 150 to75 °C, the maximum emittance remains relatively constant, ranging from 0.88 to 0.90; the Q-factor slightly increases from 87.5 to 88.3; and the emittance peak blue-shifts by 7 nm. These small changes in the emittance peaks are likely caused by thermal expansion of the layers and/or variations in the optical properties with temperature. At a low temperature of 50 °C, due to the weak intensity of thermal emission (proportional toT4), noise in the measurement, especially around the CO2 absorption window (about 4.25 μm), becomes significant in comparison to the emission intensity. The pure TP structure exhibits an emittance peak (with a Q-factor of 22) broader than the hybrid structure at 150 °C, as shown in Figure 5(c). In summary, by inserting a cavity between the DBR and the Au film of a standard TP structure, a hybrid structure sustaining a coupled TP-cavity mode that has a low background emission and a high Q-factor was obtained.
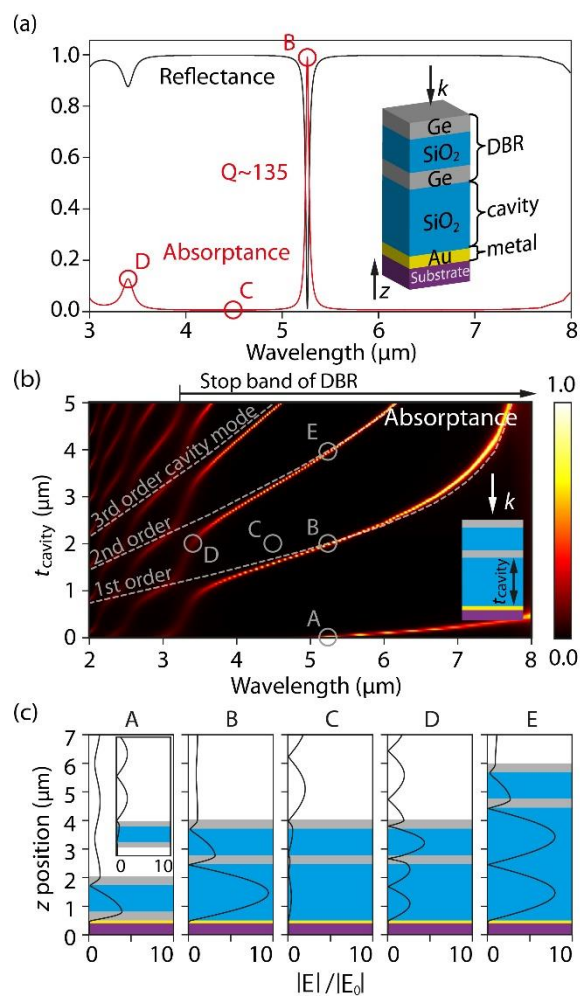
Figure 2.11(a) Simulated reflectance (black solid curve) and absorptance (red solid curve) spectra for the designed hybrid structure under normal incident light. (b) The simulated absorptance varying with light wavelength and cavity thickness, and the electric field distribution are shown in (c). Reprinted with permission, Copyright © 2018 American Chemical Society.
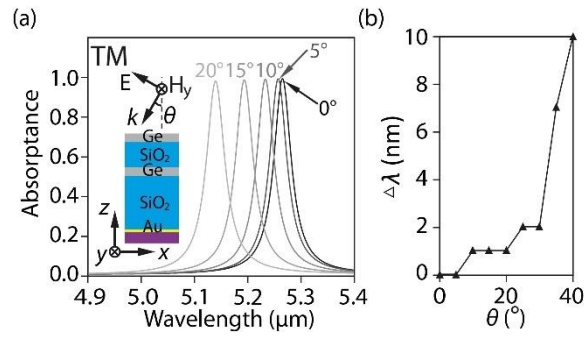
Figure 2.12(a) Simulated absorptance spectra for TM-polarized light for varying incident angles (0°, 5°, 10°, 15°, and 20°). (b) Polarization dependence. Reprinted with permission, Copyright © 2018 American Chemical Society.
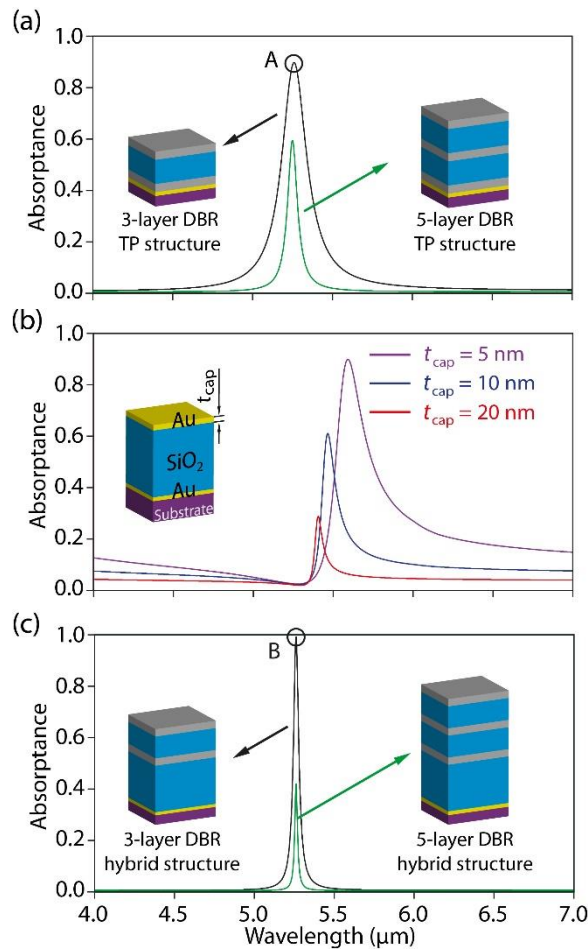
Figure 2.13(a) Absorptance spectra of the 3-layer and 5-layer DBR TP structures (black and green solid curves). (b) Absorptance spectra of Au/SiO2/Au cavity structure with different t_{cap} (thickness of surface Au). (c) Absorptance spectra of the 3-layer and 5-layer

DBR hybrid structures (black and green solid curves).Reprinted with permission, Copyright © 2018 American Chemical Society.
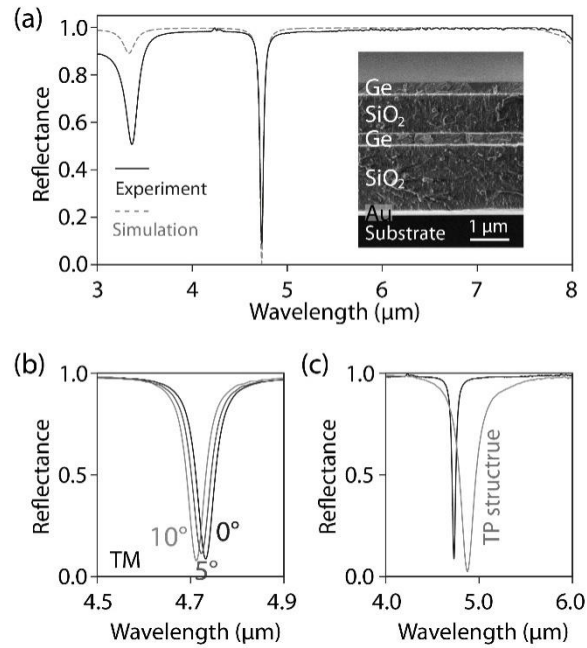
Figure 2.14 Experimental results of the reflectance spectra for the fabricated structures. Reprinted with permission, Copyright © 2018 American Chemical Society.
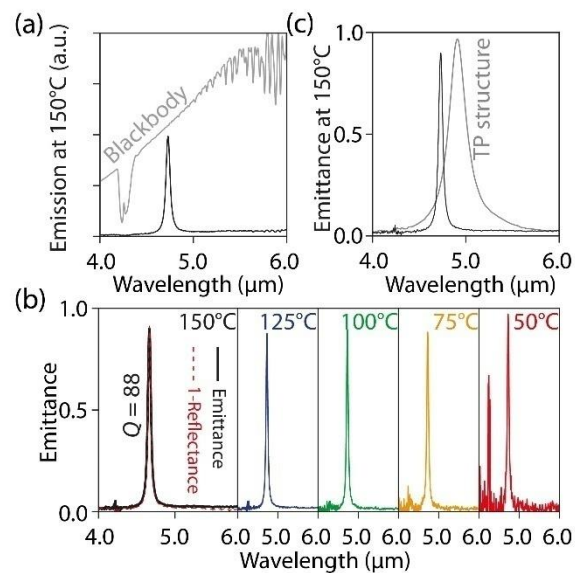
Figure 2.15 Emisssion spectra for the fabricated structures. Reprinted with permission, Copyright © 2018 American Chemical Society.

2.5 Ultra-narrowband wavelength-tunable thermal emission from hybrid metal-OTS structure

We propose a 1D structure consisting of a Ge/SiO$_2$ OTS structure and a Pt mirror as shown in Fig. 2.16a for narrow-band and wavelength-tunable thermal emission in the mid-infrared range. The two DBRs in the hybrid metal-OTS structure are adjacent to each other with Ge layer at the interface. The combination of Ge and SiO$_2$ as the DBR layers provides a large refractive index contrast, resulting in the DBRs having a high reflectance in the mid-infrared. The thickness of each DBR layer is set to have an optical thickness of one-quarter of the target wavelength (4.5 μm). As a heat resistant material, Pt provides good thermal stability when used as the metallic layer at the bottom of the structure. The layer thicknesses of the different materials are fixed throughout this section, with t_{Ge} = 280 nm, t_{SiO2} = 819 nm, and t_{Pt} = 200 nm. The hybrid metal-OTS structure exhibits a sharp and strong absorptance peak at normal incidence as shown in Fig. 2.16c. The maximum of the absorptance peak is larger than 0.8, and the peak has a Q-factor of 1908, while at an off-resonance wavelength of 4.0 μm, the hybrid metal-OTS structure maintains a low absorptance of less than 0.001, a value which is much lower than the absorptance of a semi-infinite Pt mirror (about 0.043 at the same wavelength used in the calculation). According to Kirchhoff's law, the emittance of a planar surface is equal to its absorptance, and therefore, this structure is expected to show not only a sharp and strong emission peak, but also low background emission over a large range of wavelengths.

As shown in the inset in Fig. 2.16c, we separate the hybrid structure into a top reflector and a bottom reflector along a virtual interface (i.e., the interface of two DBRs illustrated by the white dashed line), and define the reflection coefficient of an upward-propagating wave at the virtual interface as r_{top}, and the reflection coefficient of a downward-propagating wave at the virtual interface as r_{bot}, with the ambient being Ge in both cases. The confinement of light between the two reflectors requires

$$r_{top}r_{bot} \sim 1.$$

Here, $r_{top}r_{bot}$ as a function of wavelength is plotted in Fig. 2.16c (in pink color). The $r_{top}r_{bot}$ spectrum shows a peak with a near-unity value of 0.9992 corresponding to the same wavelength of the peak in the absorptance spectrum (in black color), suggesting that the

strong and sharp absorptance peak is due to the high confinement of the eigenmode sustained at the interface between the top and the bottom reflectors. Without the bottom Pt mirror (i.e., for its corresponding OTS structure), the value of the $r_{top}r_{bot}$ peak would be only 0.9977, showing that the addition of the Pt mirror enhances the confinement in the hybrid metal-OTS structure relative to a typical OTS structure.

To further compare the eigenmodes in the hybrid metal-OTS structure with the TP and OTS modes, we investigate the optical behaviors of TP, OTS, and hybrid metal-OTS structures for incident light from top (Figs. 2.16d and e). As shown by the normalized electric field ($|E| / |E_0|$) distributions at the resonance wavelengths in Fig. 2.16d, the TP structure with the Ge/SiO$_2$/Ge DBR and Pt mirror exhibits a relatively weak standing-wave pattern with a maximum normalized electric field value near the Pt mirror decaying towards the structure top, which corresponds to a relatively broad near-unity absorptance peak (the blue curve in Fig. 2.16e). Note that with only a three-layer DBR, this TP structure can sustain a fully developed TP mode. An increase in the number of the DBR pairs reduces its near-unity absorptance peak. Instead of using a metallic mirror to confine light, two DBRs having less material losses are employed in the OTS and hybrid metal-OTS structures. This results in improved light confinement observed as pronounced standing-wave patterns shown in the electric field distribution plots (Fig. 2.16d), thus revealing a much larger stored energy with sharper absorptance peaks (see the red and the black curves in Fig. 2.16e). Similar electric field distributions are found for the OTS and the metal-OTS structures, i.e., maximum values for the normalized electric field near the interface of the two DBRs (indicated as a white dashed line) decaying in intensity away from the interface. The non-zero electric field intensity below the bottom DBR of the OTS structure indicates that light transmits through the structure bottom, as evidenced by the transmittance peak at the resonance wavelength shown in the bottom-right plot of Fig. 1e. In contrast to the OTS structure, the metal-OTS structure possesses low transmission losses. Indeed, the metal film at the structure bottom can not only improve the light confinement (evidenced by a stronger electric field distribution in Fig. 1d), but also reduce the transmission loss and provide an additional inelastic loss channel. Accordingly, the hybrid metal-OTS structure exhibits an absorptance peak with a higher Q value (Q-factors are 1908 for the hybrid metal-OTS structure and 1324 for the

OTS structure) and a two-fold increase in the absorption intensity compared with that of the OTS structure (see the top-right plot in Fig. 1e). The zoomed-in plots red-rectangle-marked in Fig. 1d show absorption distributions around Pt mirror in TP and metal-OTS structures (here, absorption, noted Abs., is defined as $\omega \text{Im}(\varepsilon)|E(z)|^2$, where ω is the angularfrequency, and $\text{Im}(\varepsilon)$ is the imaginary part of permittivity) with logarithmic-scale. In the TP structure, most of the incident light is absorbed by the Pt mirror. This contrasts with the hybrid metal-OTS structure where most of the light is absorbed by the dielectric DBRs. The strong electric field of the DBRs results in two-order weaker light absorption in the Pt mirror. Interestingly, this weak metal absorption property of the metal-OTS structure is associated with a robust optical behavior (i.e., absorptance peak) independent of the metal used in the hybrid metal-OTS structure. Therefore, the metal is not limited to commonly used low-loss metals such as Ag, Au, and Al, and a variety of metals could be chosen, such as Ti for good adhesion, Pt for good thermal stability, or Pd for catalysis, without any significant change in the optical behavior. Note that this is a consequence of the non-zero loss of the dielectric materials, as evidenced by the fact that when the dielectric loss is decreased to zero in simulation, the metal-dependent absorption will become obvious.

To optimize the optical behavior of the hybrid metal-OTS structure, we examine the absorptance spectra when the number of DBR layers is varied (Fig. 2.17a). Here, as demonstrated on the right part, the configuration of the DBR_{bot} and the metallic film are fixed, and the layer number of DBR_{top} is varied (N_{top} = 5, 7, and 9). From N_{top} = 5 to N_{top} = 7, both the absorptance peak intensity and Q-factor improved. By adding two more layers (i.e., N_{top} = 9), the peak intensity decreases drastically. As a result, the structure with the 7-layer DBR exhibits the best optical behavior when considering both absorptance intensity and Q value. The optical behaviors change can be attributed to different optical "impedance matching" conditions for N_{top} = 5, 7 and 9. In the case of N_{top} = 7, it is found that the structure achieves the best impedance matching condition (the transmission loss through the top reflector matches the absorption loss of the lower reflector), thus generating a minimum reflection from the structure and a maximum for the absorptance peak.

The angular and polarization dependences are characterized for the hybrid metal-OTS structure with 7 layers in the DBR_{top}. The simulated absorptance spectra for different incident angles of the transverse electric (TE-) and transverse magnetic (TM-) polarized light are shown in the left part of Fig. 2.17b. For both TE- and TM-polarized light, when the incident angle is small (e.g., within 5°), the wavelength deviation is relatively small (less than 3 nm). However, for a larger incident angle, the resonance wavelength shows a larger angular dependence (e.g., the wavelength difference is as large as 47 nm between the case of normal incidence and the 20° TM-polarized incidence). As the incident angle increases, TE-polarized spectra exhibit weaker absorptance peaks, while the TM-polarized spectra show stronger peaks. This intensity change can be explained by the difference in the impedance matching conditions occurring for different polarizations and incident angles. The right part of Fig. 2.17b shows the wavelength difference ($|\Delta\lambda|$) between the absorptance peaks of the TM and the TE polarizations for varying incident angles. The wavelength difference increases with the incident angle, but the difference caused by the different polarizations is relatively small compared with the peak resonance bandwidths (for the incident angle of 20°, the TM and TE show a wavelength difference of 1.2 nm while the bandwidth of the peak is around 2.5 nm). In summary, the resonance wavelength of the hybrid metal-OTS structure exhibits a smaller angular and polarization dependence at small incident angles, so for the structure applied as thermal emitters, the emission near normal angle should be utilized to avoid a broadening of the emission spectrum.

Figure 2.18a shows absorptance as a function of incident wavelength and the thickness of the middle Ge layer t_{mid} (the absorptance is shown on a logarithmic-scale for a clear demonstration of the ultra-narrow absorptance peaks). High-absorptance lines represent resonance modes, and by varying t_{mid}, the resonance wavelengths can be adjusted from 3.5 μm to a wavelength longer than 5.5 μm. Therefore, thenarrow absorptance peak can be artificially designed within a wide range of wavelengths by simply adjusting t_{mid}. The inset of Fig. 2.18a shows the absorptance spectra for three different t_{mid} values (i.e., $t_{mid} = 0$, 560, and 1120 nm) as marked by the circles referring to different orders of the resonance modes. It is observed that higher-order modes have

narrower bandwidths, allowing narrower bandwidth resonances to be designed without altering the DBR layer structure.

In addition to the ability to design the absorptance peak wavelength by adjusting t_{mid}, the wavelength can also be actively tuned effect as a result of the temperature-dependent material properties. In Fig. 2.18b, we simulated the absorptance spectra of the hybrid structure with (t_{mid} = 1120 nm) and without (t_{mid} = 0 nm) the middle Ge layer at different temperatures by considering the temperature dependence of the SiO_2 and Ge refractive indices as well as the thermal expansion coefficients of Ge and SiO_2. Using a linear fitting procedure, the thermo-optic coefficients of Ge and SiO_2 are estimated to be 4.77×10^{-4}/°C and 1.23×10^{-5}/°C, respectively, and the thermal expansion coefficients of Ge and SiO_2 are taken directly from literatures as 5.90×10^{-6}/°C and 5.60×10^{-7}/°C, respectively. Without the Ge middle layer, the simulated absorptance peak shows little variation with temperature, while for the structure with a thick Ge middle layer, a strong wavelength-tuning behavior is observed. As the temperature changes from 100 to 150 °C, the absorptance peak red-shifts by 23 nm. The electric field distributions, shown to the right of the absorptance spectra, can be used to explain these different behaviors. For the structure without Ge middle layer, the maximum electric field exists in the SiO_2 layer, while for the structure with a thick Ge middle layer, the maximum electric field is within the Ge layer. Because Ge has both a more than one-order larger thermo-optic coefficient and thermal expansion coefficient than SiO_2, the structure with a Ge middle layer has a larger sensitivity to temperature. The middle Ge layer does not only store a large amount of energy, allowing for a high Q-factor resonance, but also acts as a wavelength tuning material. This structure with a thick middle Ge layer (t_{mid} around 1120 nm) was therefore chosen for fabrication.

The hybrid metal-OTS structure was fabricated and its reflectance and emittance spectra were measured as shown in Fig. 2.19. As shown in Fig. 2.19a, the measured reflectance spectrum under normal incidence (0°) shows a sharp dip at 4.516 μm with a bandwidth of 4.7 nm (corresponding to a Q-factor of 961). The reflectance dip blue-shifts by only 1.4 nm when the incident angle is varied from 0° to 5° under transverse-electric (TE) polarized incidence. An additional 5.4 nm shift is observed when the incident angle is further increased from 5° to 10°. This angular dependence reveals a relatively robust

optical behavior for near-normal incidence (e.g., within $\pm 5°$). In Fig. 2.19b, the simulations are performed for different incident angles (TE-polarized) with the actual layer thicknesses determined by cross-section scanning electron microscopy (inset in Fig. 2.19a). The wavelength of the reflectance dips matches well with the measured spectra of the fabricated structure. The deviations in the modulation depth and bandwidth may be due to imperfections in the deposited dielectric layers introducing a larger optical loss.

Figure 2.19c shows the measured emission spectra of the structure for varying temperatures between 100 and 150 °C. As temperature rises, in addition to the intensity increasing, the emission peak shifts to longer wavelengths. After normalizing by the emission of a blackbody, the emittance spectra of the structure for different temperatures are plotted in Fig. 2.19d. The room temperature emittance (grey colored, calculated as 1 - reflectance) is shown as a reference. The red-shift of the emittance peak wavelength with increasing temperature is observed. For every 10 °C increase in temperature, the wavelength of the emittance peak red-shifts by about 5.4 nm, with a total change from 100 to 150 °C of 27.1 nm. The shift of the emittance peak is 4.6 times the average bandwidth (5.9 nm) of the measured emittance peaks. Based on the data of thermo-optic coefficients of Ge and SiO_2 and their thermal expansion coefficients, the trend of the emittance wavelength shift can be reproduced by simulation. Note that this wavelength tuning behavior is not caused by the thermal degradation of the sample, as can be confirmed by the reflectance spectra taken before and after thermal emission measurements. The emittance spectra for different temperatures show similar maximum emittance values about 0.35, and the Q-factors of these emittance peaks are 789, 974, 762, 775, 703, and 684 (average Q-factor of 780) for temperatures from 100 to 150 °C. Compared with the room temperature emittance, the emittance peaks at elevated temperatures exhibit smaller Q-factors and modulations, which should be attributed to increased losses in each layer material due to the elevated temperatures. Nonetheless, the Q-factor and tunable range vs. bandwidth ratio are superior to those of any other reported thermal emitters (see the list in Table 2.1).

This temperature sensitive narrowband thermal emitter is expected to be used as a finely tunable monochromatic light source for the analysis of characteristic molecular absorptions in applications such as volatile vapour identification and bio-sensing.
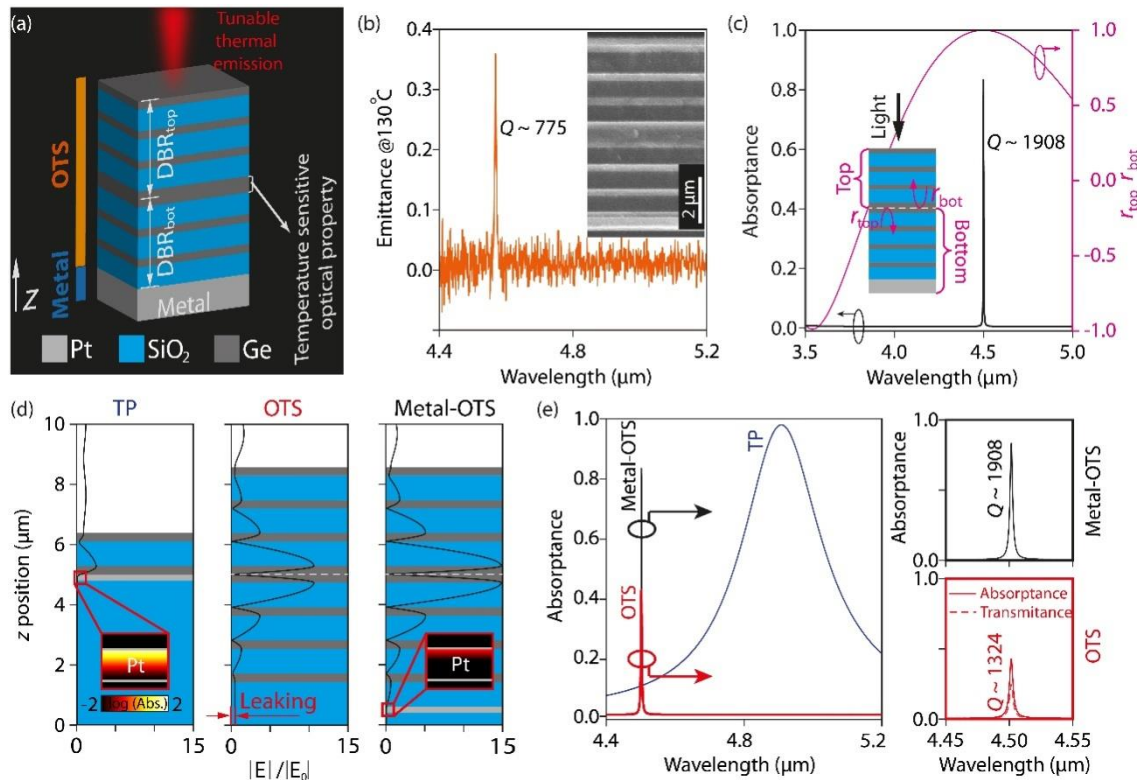
Figure 2.16 (a) Illustration of the hybrid metal-OTS structure as a wavelength-tunable thermal emitter. (b) Measured emittance spectrum at 130 °C. (c) Simulated absorptance spectrum (in black color) for the hybrid metal-OTS structure under normal incident light. (d) The simulated normalized electric field magnitude distributions of the TP, the OTS, and the hybrid metal-OTS structures at the wavelengths of the absorptance peaks. The zoomed-in plots with their absorption distributions along the Pt mirror are shown. (e) The absorptance spectra of the TP, OTS, and hybrid metal-OTS structures for normal incidence. The zoom-in plots for the absorptance spectrum of the hybrid metal-OTS structure, and the absorptance and transmittance spectra of the OTS structure are shown on the right side. Reprinted with permission, Copyright © 2020 American Chemical Society.

61
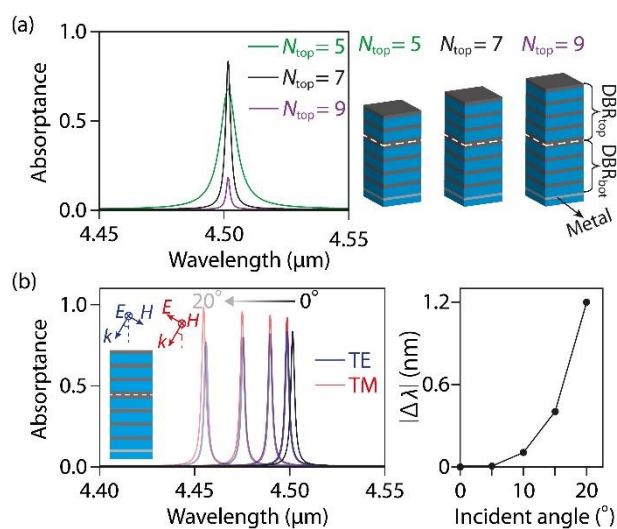
Figure 2.17 (a) Simulatedabsorptance spectra for the hybrid metal-OTS structures with different layer numbers (Ntop) in the DBRtop under normal incidence, with schematic diagrams shown on the right side. (b) Left: Simulated absorptance spectra for the hybrid metal-OTS structures with Ntop = 7 for different polarizations and incident angles of light; right: the wavelength differences between the TE- and TM-polarizations calculated for different incident angles. Reprinted with permission, Copyright © 2020 American Chemical Society.
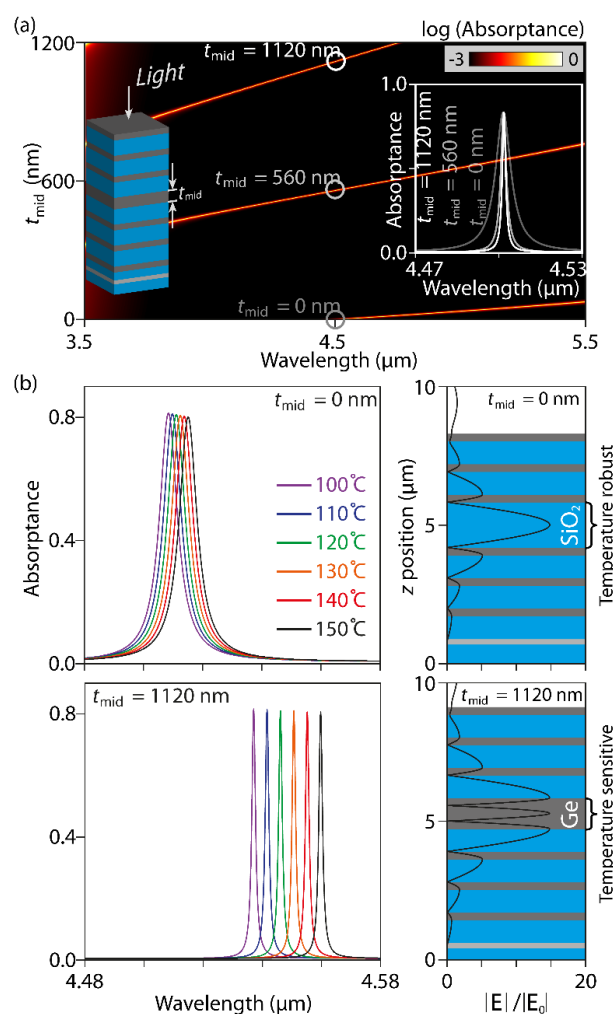
Figure 2.18 (a) The simulated absorptance varying with light wavelength and thickness of the middle Ge layer t_{mid} under normal incident light on a logarithmic-scale. The absorptance spectra for the three t_{mid} thicknesses are exhibited in the inset on the right side (the structure for tmid = 560 nm is identical to the hybrid metal-OTS structure discussed in Fig. 1 and Structure 4 in Fig. 2. (b) The simulated absorptance spectra of the structures with t_{mid} = 0 and 1120 nm at temperatures from 100 to 150 °C, together with their normalized electric field magnitude distributions at the wavelengths of their absorptance peaks at room temperature. Reprinted with permission, Copyright © 2020 American Chemical Society.
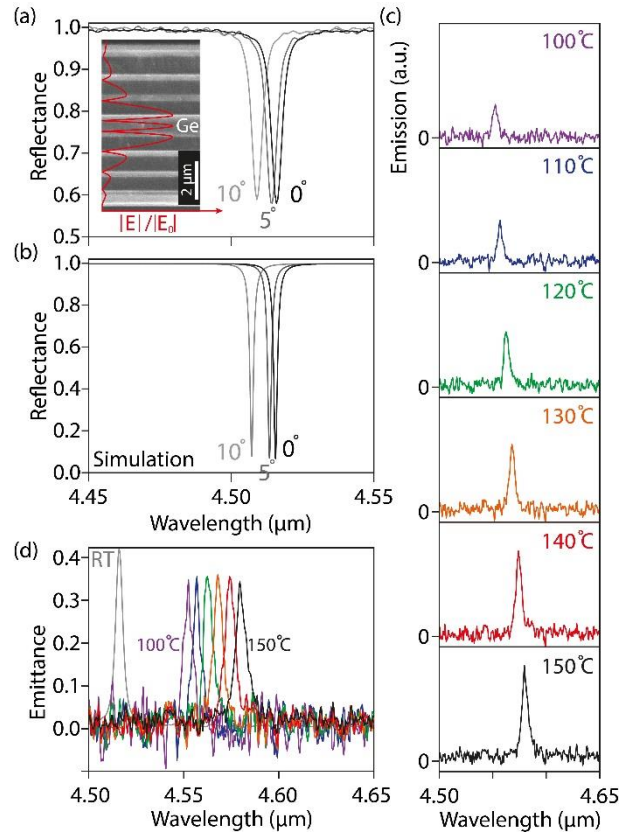
Figure 2.19Measured (a) and simulated (b) reflectance spectra of the fabricated hybrid metal-OTS structure for three different incident angles (0, 5, and 10°) under TE-polarized incident light. The actual thicknesses of the fabricated device were determined by scanning electron microscopy cross-sectional view in the inset, where the red curve reveals the normalized electric field distribution according to the actual dimension. (c) Emission spectrum of the fabricated hybrid metal-OTS structure at different temperatures of 100, 110, 120, 130, 140, and 150 °C. (d) Emittance spectra of the fabricated hybrid metal-OTS structure at different temperatures including the room temperature (marked as "RT" in grey color) shown as a reference. Reprinted with permission, Copyright © 2020 American Chemical Society.

Table 2.1 A summary of recently reported thermal emitters

Structures	$\lambda(\mu m)*$	$\varepsilon**$	Q	$\Delta\lambda_{tune}/\Delta\lambda_{band}$ ***	Refs.
Al-MIM structure	~4.2	0.95	~14	-	[8]
Quantum-well structure	~10	0.74	72	-	[11]
Hybrid TP-cavity structure	4.731	0.90	88	0.1	[16]
Optimized TP structure	6.534	0.82	188	-	[17]
SiC grating	11.5	0.46	~200	-	[7]
GST metasurface	~3	0.66~0.94	5.4	0.5	[27]
VO$_2$-sapphire 1D structure	~11	0.3~1.0	4.1	0.6	[19]
Cr-GST-Au trilayer	~10	~0.7	3.3	0.9	[20]
GST-Au 1D structure	~10	0.2~1.0	~3.6	1.1	[18]
GST-TP structure	~4.2	0.43~0.70	47~172	~2	[28]
Hybrid metal-OTS structure	4.565	0.35	780	4.6	this work

*$\lambda(\mu m)$ is the central wavelength of the emission peak.

**ε indicates peak emittance.

***$\Delta\lambda_{tune}$ is the tunable wavelength range; $\Delta\lambda_{band}$ is the bandwidth of the emittance peak.

2.6 Discussions
2.6.1 Wall-plug efficiency of the studied 1D narrowband thermal emitter

As shown in Fig. 2.20, for a thermal emitter device, unwanted heat leakage can occur through conduction and convection, thermal energy for heating up the device, and radiation into unwanted wavelength and directions. Since convection can be suppressed by operating under vacuum and conduction can be suppressed as small as 2% through a proper design of the device, it appears that the ultimate efficiency limit for incandescent sources is due to the heat for warming up the device and the emission into unwanted frequencies and directions. For an ideal thermal emitter, which has a small volume and an emission window matched the useful spectrum range, the wall-plug efficiency could achieve a value up to 98% [20]. Unfortunately, the investigated structure possesses large volume (the hybrid metal-OTS structure) and an angular dependent emission wavelength, which makes the efficiency lower than the ideal value. Here, we evaluate the efficiency of the thermal emitter by taking the hybrid metal-OTS structure as an instance.

First, we calculate heat energy consuming for warming up the structure by considering a structure with 100 mm^2 surface area. The minimum consuming energy can be calculated using specific heat capacity equation,

$$Energy(warming) > \Delta T(c_{Ge}m_{Ge} + c_{SiO2}m_{SiO2} + c_{Pt}m_{Pt}) = 0.185 \text{ J,}$$

where ΔT is the temperature change (130 °C for operating temperature at 150 °C), c is the heat capacity of materials, and m refers to mass.

Then, we consider the angular dependence of the emission. As what has been discussed, the 1D cavity structures have an angular dependent resonant frequency, exhibiting as a blue shift for a larger incident angle. As shown in Fig. 2.21, we define a useful wavelength window as wide as the full-width-at-half-maximum of the resonance

peak (~6 nm). For incident angle increasing from 0 to 6°, the central wavelength of the resonance will shift to the edge of the useful window. Therefore, the only the emission for a solid angle within 6° can be utilized, corresponding to a ratio of useful emission component of

$$\eta = \frac{\int_0^{\frac{\pi}{30}} sin\theta d\theta \cdot \int_0^{2\pi} d\varphi}{2\pi} = 0.55\%.$$

The energy consumption for a device can be calculated as

$$Energy(emission) = 2\pi A\Delta\lambda t S_B \varepsilon,$$

where 2π is the solid angle of half sphere, A is the active area of the device (100 mm^2), $\Delta\lambda$ is the emission window of 6 nm, t is the working time (for 60 minutes), S_B is the spectral radiance of the blackbody that is 35 W/m^2/sr/μm, and ε is the emittance of the structure (~0.35). Then, it is obtained that for one hour working, the energy consuming is 0.166 J, in which only 0.55% is really useful (9.13×10^{-4} J).

As shown in Table 2.2, the maximum theoretical efficiency is less than 0.3%.

The thickness of the structure or the volume can influence the energy efficiency a lot. Therefore, in order to evaluate a thermal emitter structure, we should consider not only from the Q-factor and emittance value, but also from energy aspect. Here, we give a figure of merit (FOM) for evaluation.

$$FOM = \frac{\varepsilon \times Q}{c \times t}$$

here, c is mean heat capacity $c = \frac{c_{Ge}\rho_{Ge} + c_{SiO2}\rho_{SiO2}}{2}$, t refers to total thickness of the DBR stack, ε and Q are peak emittance and quality factor. The values of FOMs for the three structure is list in Table 2.3. Although inferiors cause by large thickness and low emittance

of the metal-OTS structure, it still shows a largest FOM, because of it super-high Q value.
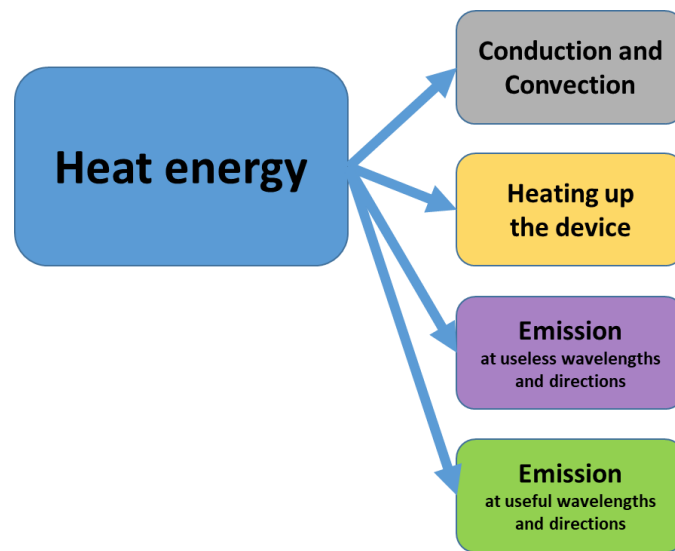
Figure 2.20 Flow chart of the heat energy consuming.
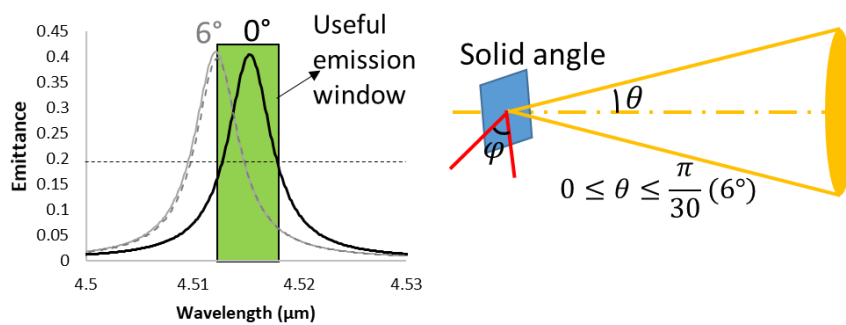
Figure 2.21 Calculations of the emission at useful wavelength range by considering the angular dependence.

Table 2.2 Energy consuming of the thermal emission device for one hour

	Energy consuming	Percentages
conduction and convection	7.20×10^{-3} J	2.00%
warming up	0.185 J	51.7%
Emission at useless wavelengths and directions	0.165 J	46.0%
Emission at useful wavelengths and directions	**9.13×10^{-4} J**	**0.254%**

Table 2.3 FOM list of all the investigated structures

Structures	ε	Q	t	c (J/K/cm)	**FOM**
Modified TP	0.94	48	2.1	1.938	**11.1**
TP -cavity	0.90	88	3.3	1.938	**12.4**
Metal-OTS	0.35	780	8.1	1.938	**17.4**

2.6.2 Detailed discussion about modulation different between the experimental spectrum and the simulation spectrum

As shown in Fig. 2.19(a) and (b), there is a large deviation in term of modulation between the experimental and the simulation results. Here, we will discuss possible reasons for this deviation.

First, the defect resulted from impurity and/or the fabrication process may increase the doping concentration in Ge material. However, the optical data for Ge in the simulation is for pure Ge without defect (k value is zero). As shown in Fig. 2.22, the carrier concentration can affect the absorption coefficient of Ge drastically. When the carrier concentration is 5×10^{17} cm^{-3}, Ge can show a k value as high as 0.0018. Then, we used this value for simulation and the result can almost reproduce the experimental reflectance spectrum.

Then, the roughness may also influence the result. We run the simulation by consider layers with a roughness Ra of 0.005 μm, as illustrated in Fig. 2.23. The value of Ra is evaluated from the real SEM image. However, it is found that the roughness of the Ge layer can make the reflectance dip a bit shallower (<0.1), so for the roughness itself cannot explain the large deviation as shown in Fig.2.19.

In conclusion, the lossy Ge in the fabricated structure as well as the roughness can affect the experimental reflectance spectrum. The lossy Ge may dominantly cause the shallower reflectance dip.

Since we have known the real loss of the materials, we could know the limitation of the Q-factor for the real fabricated metal-OTS structure. Figure 2.24 shows the simulation results of absorptance spectra of the metal-OTS structure with different DBR layer numbers achieving critical coupling conditions (for a near-unity absorptance). For

a zero-loss Ge, the structure achieves critical coupling condition for 7-layer DBR on top; however, for lossy Ge, the will structure achieves critical coupling condition for 5-layer DBR on top. The *Q*-factor drastically decreased from 1908 to 418.
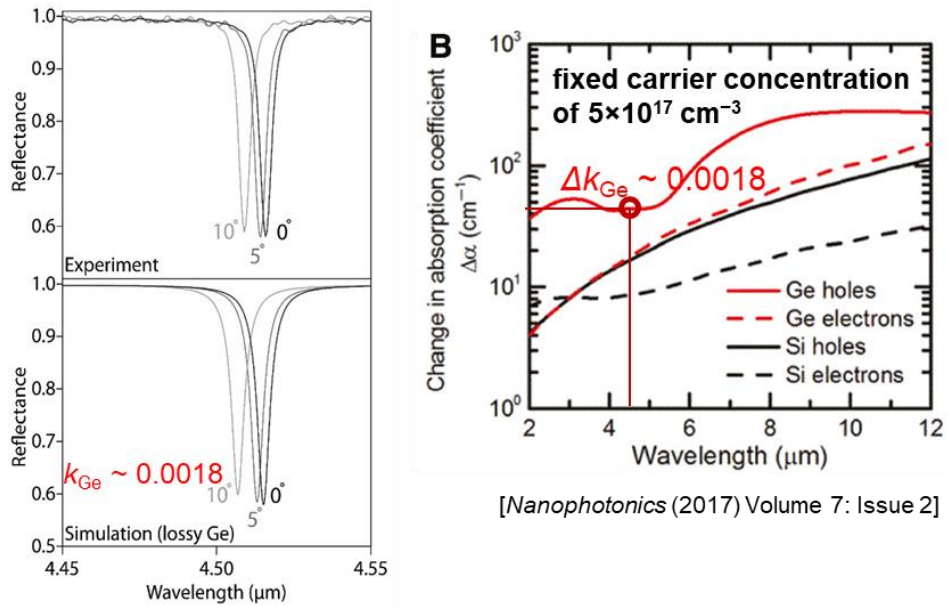
Figure 2.22 Simulation by considering optical loss in Ge.
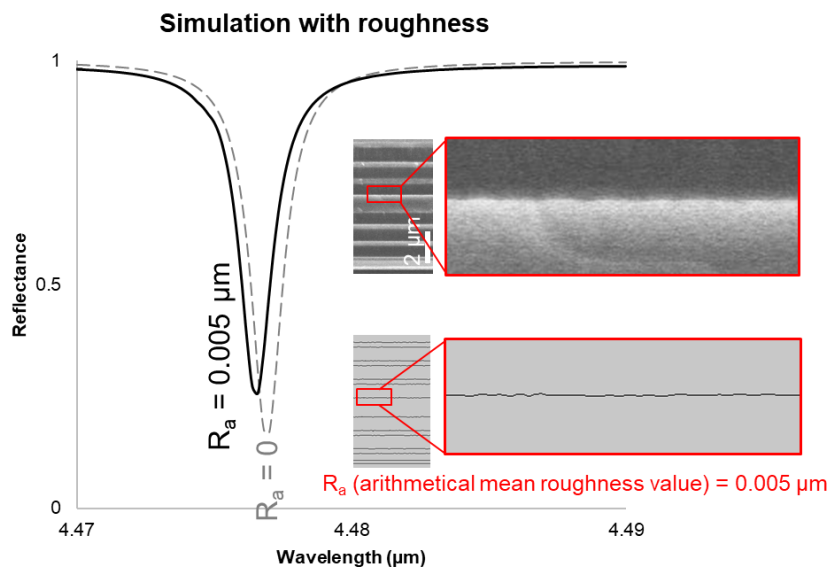
Figure 2.23 Simulation by considering the surface roughness Ra of 0.005 µm.
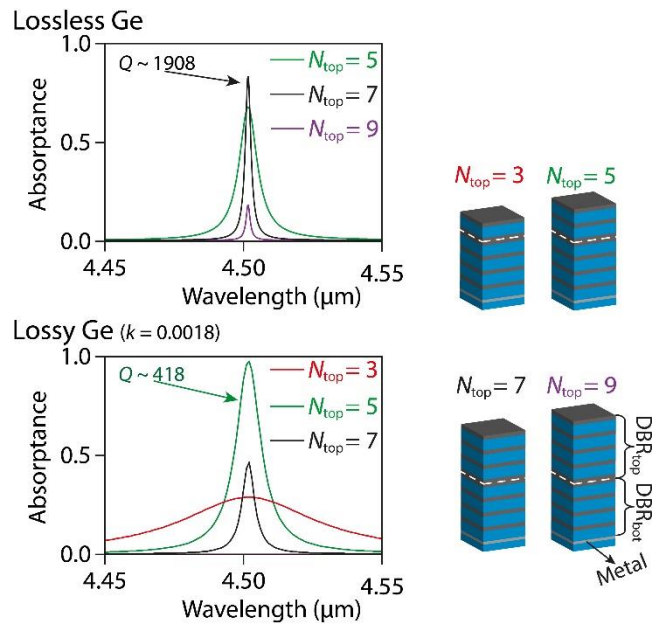
Fig. 2.24 Optimization of the configuration by considering the real loss in Ge.

References

1. D. Lin-Vien, N. B. Colthurp, W. G. Fateley, and J. G. Grasselli, The Handbook of Infrared and Raman Characteristic Frequencies of Organic Molecules (Academic Press, London, 1991).

2. H. Kaplan, Practical Applications of Infrared Thermal Sensing and Imaging Equipment (SPIE press, Bellingham, 2007).

3. P. Tallury, A. Malhotra, L. M. Byrne, S. Santra, Adv. Drug Deliv. Rev. 62, 424 (2010).

4. Costantini, D., et al. "Plasmonic metasurface for directional and frequency-selective thermal emission." Physical Review Applied 4.1 (2015): 014023.

5. Y. Yao, A. J. Hoffman, and C. F. Gmachl, Nat. Photonics 6, 432 (2012).

6. M. De Zoysa, T. Asano, K. Mochizuki, A. Oskooi, T. Inoue, and S. Noda, Nat. Photonics 6, 535 (2012).

7. T. Inoue, M. De Zoysa, T. Asano, and S. Noda, Appl. Phys. Lett. 102, 191110 (2013).

8. Y.-H. Ye, Y.-W. Jiang, M.-W. Tsai, Y.-T. Chang, C.-Y. Chen, D.-C. Tzuang, Y.-T. Wu, and S.-C. Lee, Appl. Phys. Lett. 93, 263106 (2008).

9. J. Liu, U. Guler, A. Lagutchev, A. Kildishev, O. Malis, A. Boltasseva, and V. M. Shalaev, Opt. Mater. Express 5, 2721 (2015).

10. D. Costantini, A. Lefebvre, A.-L. Coutrot, I. Moldovan-Doyen, J.-P. Hugonin, S. Boutami, F. Marquier, H. Benisty, and J.-J. Greffet, Phys. Rev. Appl. 4, 014023 (2015).

11. X. Liu, T. Tyler, T. Starr, A. F. Starr, N. M. Jokerst, and W. J. Padilla, Phys. Rev. Lett. 107, 045901 (2011).

12. K. Ikeda, H. T. Miyazaki, T. Kasaya, K. Yamamoto, Y. Inoue, K. Fujimura, T. Kanakugi, M. Okada, K. Hatade, and S. Kitagawa, Appl. Phys. Lett. 92, 021117 (2008).

13. Yang, Zih-ying, et al. "Tamm plasmon selective thermal emitters." Optics letters 41.19 (2016): 4453-4456.

14. Yang, Zih-Ying, et al. "Narrowband wavelength selective thermal emitters by confined tamm plasmon polaritons." ACS Photonics 4.9 (2017): 2212-2219.

15. Kavokin, A. V., I. A. Shelykh, and G. Malpuech. "Lossless interface modes at the boundary between two periodic dielectric structures." Physical Review B 72.23 (2005): 233102.

16. Kaliteevski, M., et al. "Tamm plasmon-polaritons: Possible electromagnetic states at the interface of a metal and a dielectric Bragg mirror." Physical Review B 76.16 (2007): 165415.

17. Wang, Zhiyu, et al. "Narrowband thermal emission realized through the coupling of cavity and Tamm plasmon resonances." ACS photonics 5.6 (2018): 2446-2452.

18. Zhu, Huanzheng, et al. "Tunable narrowband mid-infrared thermal emitter with a bilayer cavity enhanced Tamm plasmon." Optics letters 43.21 (2018): 5230-5233.

19. Sakurai, Atsushi, et al. "Ultranarrow-band wavelength-selective thermal emission with aperiodic multilayered metamaterials designed by Bayesian optimization." ACS central science 5.2 (2019): 319-326.

20. G. Brucoli, P. Bouchon, R. Haidar, M. Besbes, H. Benisty, and J.-J. Greffet, High efficiency quasi-monochromatic infrared emitter, Appl. Phys. Lett. 104, 081101 (2014).

3. Wavelength-selective hot electron photodetector through modified DBR

3.1 Introduction

Photoconductors represent the simplest conceivable type of photodetector: they consist of a finite-length semiconductor layer connected with electrodes. When it is illuminated, the photogenerated changes produced under the effect of the applied electric field lead to a photocurrent which is added to the bias current, effectively increasing the conductivity of the device. Over the past decades, the upgrading of the materials has propelled the development of different types of semiconductor-based photodetectors with operating wavelengths extending from ultraviolet to mid-infrared regime [1-5].

However, the applicable semiconductor materials are limited by their band gaps. For example, silicon cannot be used for photodetection based on band-to-band transition for the photons with energy below 1.1 eV. Aiming at the development of silicon-compatible optoelectronic devices that facilitate on-chip optics-electronics integrations, Germanium (Ge) and III−V semiconductors epitaxially grown or wafer bonding on Si with extended spectral photoresponse have therefore been attracting extensive interests for telecom communication and other infrared applications [6,7]. On the contrast, there are several alternative mechanisms enabling sub-band gap photoresponsein semiconductors, for example, two-photon absorption, bulk defect-mediated absorption, and surface defect-mediated absorption have been proposed previously for silicon devices.

Without extra process complexity or cost for introducing foreign absorbing materials on silicon, the implementation of these sub-band photon-to-electricity

conversion strategies in practice, however, has been hampered by problems inefficiency, speed, reliability issues, and so on. Photon absorption in a metal can excite hot-electrons with energies higher than the Fermi level of the metal. This hot-electron generation mechanism has been used in a variety of applications, such as photodetection [8-12], photovoltaics [13,14], and photocatalysis [15,16]. In photodetection, the generated hot-electrons can cross the energy barrier at a metal-semiconductor (M-S) or metal-insulator (M-I) interface, creating a photocurrent that enables the detection of photons with an energy smaller than the band-gap of the semiconductor or insulator. This allows even wide-bandgap metal oxides (e.g., Al_2O_3, ZnO, and TiO_2) to be used to detect low-energy photons in the visible or even and infrared spectral regions [17,18].

In order to detect the photocurrent generated by hot-electrons, metal-insulator-metal (M-I-M) structure has been studied theoretically and experimentally. In the M-I-M structure, the absorption of light in the metallic films generates hot-electrons. Assuming that the generated hot-electrons propagate in all directions with the same probability, half of the hot-electrons will diffuse towards the M-I interface. Only the hot-electrons with energy higher than the energy barrier at the interfaces will have possibilities to cross the insulator layer and, finally, be collected by the opposite electrode to form a photocurrent. Since the hot-electrons are generated on both sides of the structure, a net photocurrent only results when the current from one of the two metallic films is larger than the other. For optical systems, such as wavelength division demultiplexing [19,20], imaging [21], and bio-sensing [22], wavelength determination and selection are also crucial. However, without a light-trapping mechanism, a mirror-like M-I-M structure cannot effectively absorb light at a given wavelength, and thus, is not suitable for spectrally selective detection.

Tamm plasmons (TPs) or optical Tamm states are known to exist at the interface between a metallic film and a distributed Bragg reflector (DBR) [23]. At the TP resonance wavelength, the electromagnetic surface wave propagating along the metal/DBR interface can be highly confined in the region around the metal/dielectric interface, allowing for strong absorption by the metallic film. Because of this, the planar Tamm plasmonic structures (TP structures) have generated a lot of interest as narrowband wavelength-selective absorber and have been used in many applications, such as thermal emitters [24,25], semiconductor lasers [26], and chemical and biochemical sensors [27,28]. In a TP structure, by replacing the metallic film with the M-I-M or M-S hot-electron device, the wavelength dependent absorption modulation can be harnessed, thus realizing a wavelength-selective photodetection.

In this section, first, we demonstrate a one-dimensional wavelength-selective hot electron photodetector at telecomm-wavelength. The photocurrent is caused by hot electron internal emission from metal into ZnO, and the wavelength-selective property is due to TP resonance. This result is the first, so it proved the possibility of one-dimensional structure for wavelength-selective photodetection using hot electron. However, extend Si possibility is terminal wanted. And due to a high temperature crystal process, Si crystallization cannot be operated on the device, so Si-device needs to rely on well-crystallized and doped Si substrate. However, it is difficult to combine the Si substrate with TP structure for a hot electron internal emission from metal into Si. In the second section of this part, we propose an idea of combining Si substrate and one-dimension wavelength-selective structure using SOI substrate.

3.2 Hot-electron photodetector with wavelength selectivity in near-infrared via Tamm plasmon

For the first time, we experimentally investigate a TP coupled hot-electron photodetector. The proposed photodetector consists of a metal-semiconductor-ITO (M-S-ITO) structure on the top and a seven-layer DBR on the bottom and is designed for wavelength-selective photodetection at telecommunication wavelengths (around 1550 nm) (see Fig. 3.1a). Having a similar mechanism as the M-I-M structure, the M-S-ITO structure with Au/Ti, ZnO, and ITO thin layers acts as a hot-electron device; however, in contrast with the conventional M-I-M structure, the M-S-ITO structure guarantees a large net photocurrent, due to a predominant hot-electron generation in the Au/Ti films. In the proposed TP structure, the metallic films are designed to be on the top, which avoids the large internal stress at metal interfaces in the case of using the metallic films between a thick DBR stack and the substrate, thus ensuring a stable structure. Owing to the large refractive index contrast between Ge and SiO_2, a Ge/SiO_2 DBR with only seven layers can realize high light confinement, and a well-developed TP is sustained between the DBR and the metallic film in the M-S-ITO structure, as revealed by the observed strong and sharp reflectance dip (bandwidth of 43 nm and modulation of 0.70) at a wavelength of 1581 nm. The photoresponse has a maximum value of 8.26 nA/mW at a wavelength of 1581 nm which drops by more than 80% when the illumination wavelength is varied by only 52 nm (from 1581 to 1529 nm), thus indicating the realization of a wavelength-selective photodetection. This TP structure provides a practical means for realizing high-performance, lithography-free, and wavelength-selective hot-electron photodetectors using the proposed M-S-ITO-DBR planar structure in the near-infrared range.

The studied TP coupled hot-electron photodetector comprises an Au/Ti-ZnO-ITO structure (i.e., the M-S-ITO structure) and a modified Ge/SiO$_2$ DBR on a fused quartz substrate, as shown in Fig. 1a. The modified DBR consists of three pairs of alternating layers of Ge/SiO$_2$ combined with a thicker Ge layer adjacent to the M-S-ITO structure (i.e., the last Ge layer). The M-S-ITO structure acts as a hot-electron device and concurrently provides the metallic film used to excite TPs. As shown in Fig. 3.1b, at the TP resonance wavelength, the electric field magnitude distributions reveal a standing-wave pattern with a maximum in the last Ge layer that decays towards both the Au film and the Ge/substrate interface, indicating light confinement between the metallic film and the modified DBR. As a result, the TP coupled photodetector structure exhibits a peak in the absorptance spectrum (or a dip in the reflectance spectrum) with a narrow bandwidth of 32 nm at a wavelength of 1600 nm in the stop band of the modified DBR for normal incidence (see Fig. 3.1c). At the TP resonance wavelength (indicated by the black circle in Fig. 3.1c), the calculated absorption distribution in the M-S-ITO structure (presented in Fig. 1d) shows that the absorption predominantly occurs in the Au/Ti thin films near the Ti-ZnO interface, thus indicating a preferential hot-electron generation in the Au/Ti (the absorptance in the Au/Ti, the ITO, the ZnO, and the Ge layers are 0.636, 0.055, 0.007, and 0.147, respectively). Note that the thickness of the Au film is much smaller than the mean free path (MFP) of electrons in Au (about 74 nm for low-energy electrons) ensuring a high probability for the generated hot-electrons to reach the M-S interface before scattering occurs; however, a shorter MFP of ITO hinders the hot-electrons from reaching the ITO-ZnO interface. Depending on the energy and momentum of the hot-electrons reaching the interface, the hot-electrons will accomplish the interfacial electron transmission process with different probabilities and ultimately generate a photocurrent.

As a result, the hot-electrons will preferentially flow from the metal side to the ITO side. Besides increasing the adhesion between Au and ZnO, the existence of the 2-nm Ti also helps to reduce the barrier energy by forming an ohmic contact at the M-S interface. This lower energy barrier interface can contribute to an improvement of the photoresponse, owing to an increase in the probability for the hot-electrons to cross the energy barrier at the interface. In Fig. 3.1e, the energy band diagram of the structure is shown. The Fermi level of the structure consisting of Au, Ti, ZnO, and ITO is indicated as a dashed line, the upper and lower horizontal lines of the square in the ZnO layer represent the conduction and valence band edges, respectively, and the vertical lines represent the energy barriers at the interfaces. Here, the Fermi levels of the metals and the ITO are assumed to have the same value due to the similar work functions of ITO and Ti, and the energy barriers for electrons (ϕ_e) at the Ti-ZnO and ITO-ZnO interfaces are evaluated to have low values less than 0.35 eV (from the literature, the work functions of Ti and ITO, and the electron affinity of ZnO are 4.33 eV, 4.15~4.40 eV, and 4.20~4.50 eV, respectively). As shown in Fig. 3.1e, the hot-electrons (red dots) having energies greater than the electron barrier ϕ_e may cross the barrier throughthe conduction band of ZnO, and an equal number of hot-holes (red circles) are left below the Fermi level. However, considering the ZnO band gap ($\phi_e + \phi_h$) of 3.30 eV, a much larger value of the energy barrier is experienced by the hot-holes (ϕ_h should be not less than 2.95 eV). As this is much larger than the incident photon energy (0.8 eV), there is a negligible transmission probability of hot holes across the barrier, and as a result, the photocurrent contributed by the hot-holes is miniscule and not discussed in the following. The number of injected hot-electrons is indicated by the number of arrows above the energy band diagram (Fig. 3.1e): more hot-electrons are injected from the metal side than from the ITO side, resulting in a clockwise direction of

electron flow in the circuit. Note that a SiO$_2$ layer of 10 nm is used to insulate the M-S-ITO hot-electron device from the DBR, in order to avoid the leakage of the photocurrent.

To clarify the optical behavior of the proposed TP hot-electron photodetector, the structure with different DBR configurations are numerically investigated (see Fig. 3.2). The DBR labelled by the number, N, of Ge/SiO$_2$ pairs with an additional Ge layer adjacent to the Au film (the last Ge layer), as shown in the schematic diagram given in Fig. 3.2a. In a standard TP structure, the optical thickness of each DBR layer needs to be one-quarter of the DBR central wavelength. Here, t_{SiO2}, t_{last} and t_{Ge} are set to be 195 nm, 66 nm, and 52 nm, respectively, thus giving a DBR central wavelength of around 1600 nm (t_{SiO2}, t_{last}, and t_{Ge} represent the thicknesses of the SiO$_2$ layers, the last Ge layer, and the other Ge layers in the DBR). The top Au layer needs to be semitransparent ($t_{Au} = 20$ nm), so that the incident light at the TP resonance wavelength can penetrate through the Au layer. The thicknesses of the insulating SiO$_2$, ITO, ZnO, and Ti layers are fixed at 10 nm, 20 nm, 20 nm, and 2 nm throughout this paper. Figure 3.2a shows the reflectance and transmittance spectra of the TP coupled hot-electron photodetector for different values of N of the DBR. As N increases from 1 to 4, the reflectance dip deepens and narrows (conversely the transmittance decreases), which indicates the strengthening of the TP resonance. The electric field distributions of the TP structures with different pair numbers calculated at their corresponding reflectance dip wavelengths are shown in Fig. 3.2b. The TP structure with only one pair reveals a clear standing-wave pattern inside the DBR structure with an electric field maximum at the top Ge/SiO$_2$ interface and a gradual decrease in the field towards the Au film and the substrate. As N increases, a stronger electric field is built at the top Ge/SiO$_2$ interface indicating improved light confinement. Concurrently, the electric field in the substrate decreases resulting in a lower transmission loss of the TP

structure. Note that the proposed TP structure with only-three-pair DBR achieves a reflectance dip as low as 0.2, which demonstrates superior light confinement of DBR based on the Ge/SiO$_2$ pair of materials. As no significant improvement in the optical behavior of the TP structure for N larger than three was found, the TP structure with a three-pair DBR is discussed in the following.

In order to optimize the optical performance of the three-pair DBR TP structure, the reflectance spectra were calculated by varying the thickness of the last Ge layer (t_{last}) from 0 to 500 nm (other thicknesses are kept unchanged from those in Figs. 3.2a and b). As shown in Fig. 3.2c, several low reflectance lines, indicating different orders of the TP mode, are observed in a wide range of wavelengths, thus enabling a fine selection of the photodetection wavelength. The upper plot of Fig. 3.2d shows the reflectance spectra for the three different t_{last} values of 52, 240, and 428 nm as indicated by the horizontal dashed lines in Fig. 3.2c. As t_{last} increases, the structure shows a slightly shallower reflectance dip with a narrower bandwidth at the same resonance wavelength. To clarify the optical behavior of the TP structure with different t_{last}, simulation results of $r_{DBR}r_{top}$ as a function of wavelength are plotted below their reflectance spectra. As shown in the inset at the bottom of Fig. 3.2d, r_{DBR} is the reflection coefficient of a wave incident on the DBR from Ge, and r_{top} is the reflection coefficient of the wave incident on the insulating SiO$_2$ layer and hot-electron device layers (i.e., ITO, ZnO, Ti, and Au layers) from the DBR side. For TPs to be excited, the condition of $r_{DBR}r_{top} \sim 1$ should be satisfied (corresponding to $r_{DBR}r_{top}$ peak in the lower plot of Fig. 3.2d). Due to the nonzero imaginary part of the refractive index of Ge at wavelengths around 1600 nm, the absorption loss increases with t_{last}, resulting in a less-developed TP resonance for a larger t_{last}, as indicated by the weaker $r_{DBR}r_{top}$ peak that corresponds to the shallower reflectance dip. However, a sharper

$r_{DBR}r_{top}$ peak indicates a stricter resonance condition for a higher-order TP mode, which in turn results in a sharper reflectance dip. As shown in their electric field distributions (Fig. 3.2e), in the case of a larger t_{last}, a standing-wave pattern with a larger number of nodes is found in the last Ge layer indicating a higher-order TP mode. In order to take advantage of both narrowband wavelength selectivity and hot-electron generation efficiency, the TP structure with t_{last} around 240 nm is targeted for fabrication.

The TP structures were fabricated on fused quartz substrates using RF-magnetron sputtering (a detailed description of the fabrication process is reported in the Methods section). The reflectance spectra of the fabricated structures were measured under normal incidence using an FT-IR spectrometer (VIR-300, JASCO, Tokyo, Japan) with a spectral resolution of 4 cm^{-1}. For comparison purposes, the optical properties of the TP hot-electron photodetector (with all hot-electron device layers as shown in the right inset of Fig. 3.3a) together with that of a simple TP structure (without the ITO, ZnO, and Ti thin films, as shown in the left inset) are shown in Fig. 3.3a. The simple TP structure exhibits a reflectance dip of 0.15 at a wavelength of 1485 nm with a full-width-at-half-maximum (fwhm) of 64 nm (black curve), while the sample including the hot-electron structure exhibits a red-shifted (96 nm) reflectance dip with a narrower fwhm of 43 nm (blue curve). The simulated reflectance spectra (dashed curves) reproduce well the measured spectra of the fabricated structure in terms of the position, bandwidth, and modulation of the resonance dips. The differences between the simulated and the measured spectra are very likely due to differences in the actual and ideal refractive indices of the materials. The scanning electron microscopy (SEM) cross-sectional image of the fabricated TP hot-electron photodetector with all layers included is shown in Fig. 3.3b. Since photons absorbed in the different layers do not contribute equally to the photo-

generated current, we also show the proportions of light absorbed by the different materials within the device in Fig. 3.3c. It is found that the absorptances of all layers have peak values around the wavelength of the absorptance peak of the whole device (1581 nm). However, the contributions of the different layers to the absorptance vary with the wavelength: on the short wavelength side of the absorptance peak (around 1529 nm), absorption of the Ge layers account for a large portion of the total absorption (about 80%), while on the long wavelength side of the peak (around 1629 nm), absorption is mainly due to the metallic films (metal films absorptance accounts for about 90% the total absorption). As a result, the net photocurrent, which is approximately proportional to theabsorptance difference between the metal layer and the ITO layer, is expected to be larger on the long wavelength side of the peak than on the short wavelength side.

The current−voltage ($I−V$) characteristics under dark conditions for the fabricated TP coupled hot-electron photodetector structure are shown in Fig. 3.4a with the corresponding schematic diagram inserted in the top-left figure. The $I−V$ curve was obtained with an ammeter operating with a DC source swept from −0.2 to 0.2 V. The current versus voltage shows a linear relation indicating an ohmic contact at the interfaces of Au/Ti-ZnO as well as ZnO-ITO. A logarithmic-scale $I−V$ curve is shown in the right-bottom inset, revealing a dark current at zero bias of the order of 10 pA. The wavelength dependent photoresponse of the device was experimentally examined under a monochromatic collimated beam with a diameter of 1.4 mm from a narrow bandwidth tunable laser source (TLG-210, Alnair Labs Co., Tokyo, Japan) within a wavelength range of 1529-1607 nm (within C- and L-band of telecommunication wavelengths). As shown in Fig. 3.4b, the electrical photoresponse variation of the TP coupled hot-electron photodetector for varying incident wavelengths at zero bias is plotted together with

absorptance difference between the metallic films and the ITO film (i.e., $A_{\text{Metal}} - A_{\text{ITO}}$, in red color). Qualitatively, the photoresponse and $A_{\text{Metal}} - A_{\text{ITO}}$ have a similar wavelength dependence, indicating the realization of a wavelength-selective photodetection. Some discrepancies may be caused by sample to sample variability as separate samples had to be made for the reflectance measurement and the photocurrent measurement because of the differecences in the experimental setups (see *Fabrication process* in the Methods section for detailed information). The photoresponse shows the largest reaches a maximum value of 8.26 nA/mW at a wavelength of 1581 nm around the ($A_{\text{Metal}} - A_{\text{ITO}}$) peak and decreases by more than 80% (to a value of 1.62 nA/mW) from the peak to background level (corresponding to a wavelength of 1529 nm). Note that the value of the electrical photoresponse of an M-I-M or M-S-ITO devices can be affected by many factors, such as the structure configuration, choice of materials, and the target wavelength. Values ranging from 0.01 to 7000 nA/mW have been reported in the literature. The maximum photoresponse reported in this work is comparable to other works reported in the literature and could potentially be improved by reducing the ZnO thickness. Though other M-I-M or M-S-ITO devices operating with higher photoresponses at wavelengths below 850 nm have been reported, this work offers a practical strategy to extend the operating wavelength to the telecommunication range (about 1550 nm) while simultaneously providing wavelength-selectivity. The optical and electrical performances under oblique incidences were simulated. With a larger incident angle, the absorptance peak blue shifts, and therefore, the electrical photoresponse is expected to weaken. Furthermore, the photocurrent is measured for different powers intensities of the monochromatic illumination. The linearity of the photocurrent with incident light power intensity confirms that hot-electrons are generated via a single-photon process. Figure

3.4c shows the time-dependent photoresponse of the TP coupled hot-electron photodetector with no bias for the wavelengths of 1529, 1555, and 1581 nm. The illumination is switched on/off by using an optical shutter and an exposure time of 10 s is used.
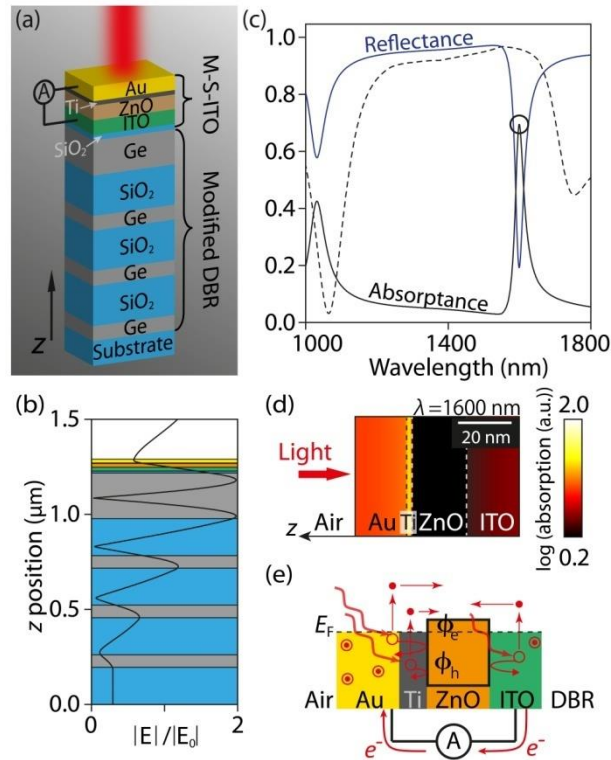
Fig. 3.1(a) Schematic diagram of the TP coupled hot-electron photodetector. (b) Profile of the normalized electric field |E|/|E₀| along *z*-axis for the TP coupled hot-electron photodetector at the resonance wavelength corresponding to the black circle in (c). (c) Simulated reflectance (blue solid curve) and absorptance (black solid curve) spectra for the TP coupled hot-electron photodetector for normal incidence, together with reflectance spectrum of the modified DBR (black dashed curve). (d) Absorption distribution in the M-S-ITO structure at the resonance (i.e., λ= 1600 nm) corresponding to the black circle in (c) with logarithmic-scale. (e) Energy band diagram of the M-S-ITO structure. (Thicknesses of the last and other Ge layers, SiO$_2$ in the DBR, SiO$_2$ below the ITO, ITO, ZnO, Ti, and Au layers are 240 nm, 66 nm, 195 nm, 10 nm, 20 nm, 20 nm, 2 nm, and 20 nm, respectively.)
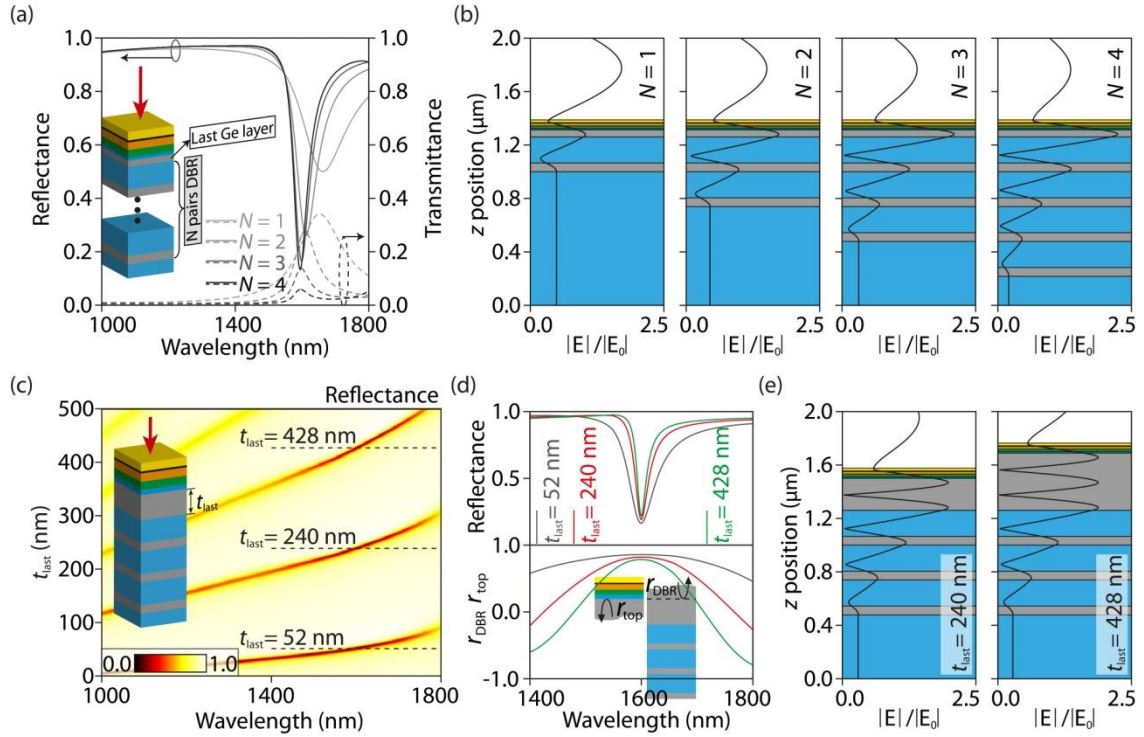
Fig. 3.2 Simulation results of the TP coupled hot-electron photodetector by varying Ge/SiO$_2$ pair number (N) and thickness of the last Ge layer (t_{last}), with other thickness kept constant. (a) Simulated reflectance (solid curves) and transmittance (dashed curves) spectra with different N for t_{last} = 52 nm. (b) Normalized electric field magnitude distributions at the wavelengths corresponding to the reflectance dips having different N, as in (a). (c) Simulated reflectance for varying wavelengths and t_{last} with normal incidence. The three horizontal dashed lines indicate different t_{last} values (i.e., 52, 240 and 428 nm). The reflectance spectra for the three t_{last} thicknesses exhibited in the upper plot of (d); the calculated $r_{DBR}r_{top}$ as a function of wavelength for the three t_{last} thicknesses simulated is shown in the lower plot of (d). (e) Normalized electric field magnitude distributions at the wavelengths corresponding to the reflectance dips with t_{last} = 240 and 428 nm, as in (d).
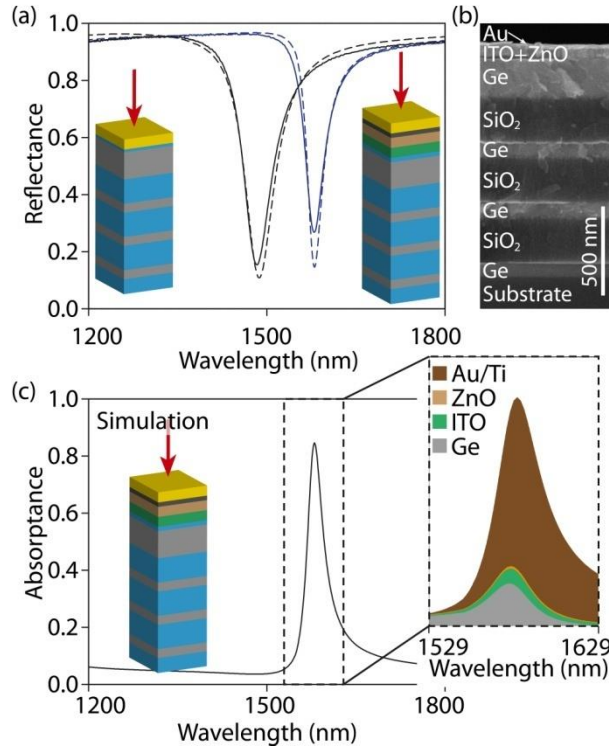
Fig.3.3 (a) Comparison between the measured reflectance spectra of the TP structure with (blue solid curve) and without the hot-electron device layers (black solid curve) under normal incidence. The simulation results are also plotted as references (dashed curves). The actual thicknesses of the fabricated device were determined by scanning electron microscopy cross-sectional view in (b):t_{Ge} = 82 nm, t_{SiO2} = 254 nm, t_{last} = 221 nm, t_{ins} = 10 nm, t_{ITO} = 20 nm, t_{ZnO} = 20 nm, t_{Ti} = 2 nm, and t_{Au} = 20 nm, where t_{ins} indicates the thickness of the SiO_2 layer insulate the M-S-ITO structure from the DBR. The insets show schematic diagrams of these two structures. (c) Simulated absorptance (dashed curves) spectrum for the fabricated structure, with fractions of light absorbed by the different absorbing materials in the device (the right part).

89
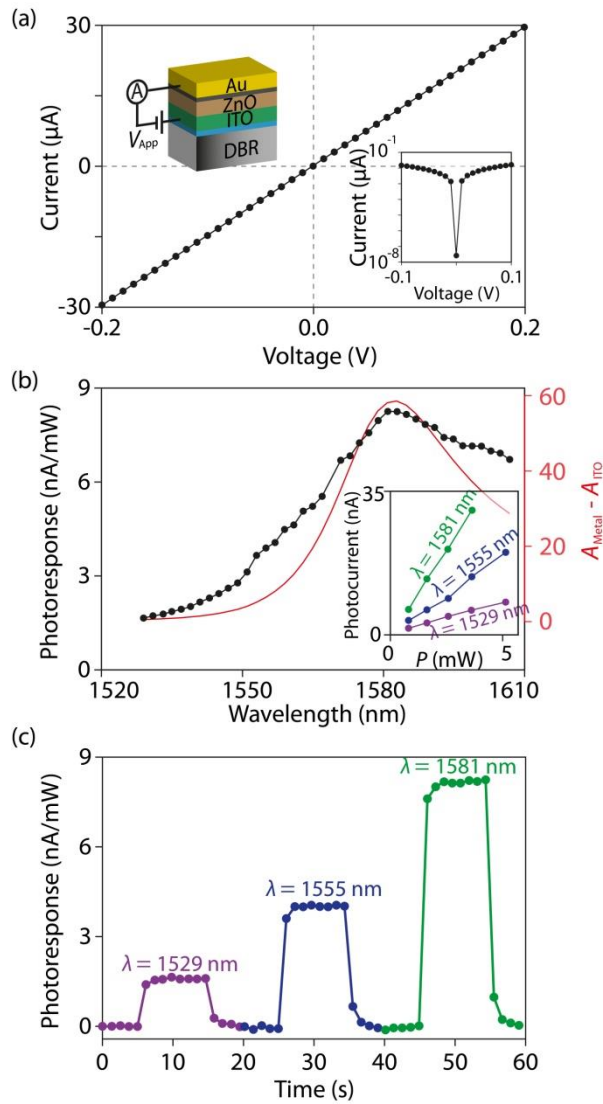
Fig. 3.4 (a) Current-voltage curve ($I-V$ curve) of the TP photodetector. The two electrodes are Au/Ti and ITO thin films as shown in the left-top inset. A logarithmic-scale $I-V$ curve is shown in the right-bottom inset. (b) The wavelength dependent photoresponse of the TP photodetector (black points) at zero bias together with absorptance difference spectrum between metallic films and ITO film ($A_{Metal} - A_{ITO}$, red curve). Photocurrent changes with incident power for different illumination wavelengths shown as the inset. (c)Time-dependent photoresponse of the TP coupled hot-electron photodetector without bias.

3.3 Conclusions

In his work, the TP coupled hot-electron photodetector, which combines a TP structure and an M-S-ITO structure, was investigated both theoretically and experimentally in the near-infrared range. The excitation of TPs in the structure realizes a wavelength-selective absorption, contributing to a wavelength dependent hot-electron generation. The anisotropic light absorption in metallic films and ITO film leading to a predominant hot-electron follow from metal to ITO. As a result, a maximum photoresponse of 33 nA/mW was measured at the TP resonance wavelength of 1581 nm. The absorption peak of the photodetector was monitored by a change of photoresponse as large as 26 nA/mW at zero-bias. As a result, a wavelength-selective photodetection is realized. This work provides an actual approach to achieve a wavelength-selectivity of a planar photodetector via a coupling of TPs.

References

1. Dou, Letian, et al. "Solution-processed hybrid perovskite photodetectors with high detectivity." Nature communications 5.1 (2014): 1-6.

2. Wan, Xia, et al. "A self-powered high-performance graphene/silicon ultraviolet photodetector with ultra-shallow junction: breaking the limit of silicon?." npj 2D Materials and Applications 1.1 (2017): 1-8.

3. Koppens, F. H. L., et al. "Photodetectors based on graphene, other two-dimensional materials and hybrid systems." Nature nanotechnology 9.10 (2014): 780-793.

4. de Arquer, F. Pelayo García, et al. "Solution-processed semiconductors for next-generation photodetectors." Nature Reviews Materials 2.3 (2017): 1-17.

5. Keuleyan, Sean, et al. "Mid-infrared HgTe colloidal quantum dot photodetectors." Nature Photonics 5.8 (2011): 489-493.

6. Michel, Jurgen, Jifeng Liu, and Lionel C. Kimerling. "High-performance Ge-on-Si photodetectors." Nature photonics 4.8 (2010): 527-534.

7. Brouckaert, Joost, et al. "Thin-film III–V photodetectors integrated on silicon-on-insulator photonic ICs." Journal of Lightwave Technology 25.4 (2007): 1053-1060.

8. Knight, M. W.; Sobhani, H.; Nordlander, P.; Halas, N. J. Science 2011, 332, 702-704.

9. Ho, Y.-L.; Huang, L.-C.; Delaunay, J.-J. Nano Lett. 2016, 16, 3094-3100.

10. Chalabi, H.; Schoen, D.; Brongersma, M. L. Nano Lett. 2014, 14, 1374-1380.

11. Gong, T.; Munday, J. N. Nano Lett. 2014, 15, 147-152.

12. Lin, K. T.; Chen, H. L.; Lai, Y. S.; Yu, C. C. Nat. commun. 2014, 5, 3288.

13. Clavero, C. Nat. Photonics 2014, 8, 95-103.

14. Smith, J. G.; Faucheaux, J. A.; Jain, P. K. Nano Today 2015, 10, 67−80.

15. Li, J.; Cushing, S. K.; Zheng, P.; Meng, F.; Chu, D.; Wu, N. Nat. Commun. 2013, 4, 2651.

16. Mukherjee, S.; Libisch, F.; Large, N.; Neumann, O. Brown, L. V.; Cheng, J.; Lassiter, J. B.; Carter, E. A.; Nordlander, P.; Halas, N. J. Nano Lett. 2012, 13, 240-247.

17. Ishii, S.; Shinde, S. L.; Jevasuwan, W.; Fukata, N.; Nagao, T. ACS Photonics 2016, 3, 1552-1557.

18. García de Arquer, F. P.; Mihi, A.; Konstantatos, G. ACS photonics 2015, 2, 950-957.

19. Brackett, C. A. IEEE J. Sel. Areas Commun. 1990, 8, 948-964.

20. Kersey, A. D.; Davis, M. A.; Patrick, H. J.; LeBlanc, M.; Koo, K. P.; Askins, C. G.; Putnam, M. A.; Friebele, E. J. J. Lightwave Technol. 1997, 15, 1442-1463.

21. Park, H.; Dan, Y.; Seo, K.; Yu, Y. J.; Duane, P. K.; Wober, M.; Crozier, K. B. Nano Lett. 2014, 14, 1804-1809.

22. Wu, X.; Lee, H.; Bilsel, O.; Zhang, Y.; Li, Z.; Chen, T.; Liu, Y.; Duan, C.; Shen, J.; Punjabi, A.; Han, G. Nanoscale 2015, 7, 18424-18428.

23. Kaliteevski, M., et al. "Tamm plasmon-polaritons: Possible electromagnetic states at the interface of a metal and a dielectric Bragg mirror." Physical Review B 76.16 (2007): 165415.

24. Wang, Z.; Clark, J. K.; Ho, Y.-L.; Vilquin, B.; Daiguji, H.; Delaunay, J.-J. ACS photonics 2018, 5, 2446-2452.

25. Wang, Z.; Clark, J. K.; Ho, Y.-L.; Vilquin, B.; Daiguji, H.; Delaunay, J.-J. Appl. Phys. Lett. 2018, 113, 161104.

26. Symonds, C.; Lheureux, G.; Hugonin, J. P.; Greffet, J. J.; Laverdant, J.; Brucoli, G.; Lemaitre, A.; Senellart, P.; Bellessa, J. Nano Lett. 2013, 13, 3179-3184.

27. Auguié, B.; Fuertes, M. C.; Angelomé, P. C.; Abdala, N. L.; Soler Illia, G. J.; Fainstein, A. ACS Photonics 2014, 1, 775-780.

28. Maji, P. S.; Shukla, M. K.; Das, R. Sensors and Actuators B: Chemical 2018, 255, 729-734.

4. Discussions and outlook

4.1 Summary and discussions

By adding more DBR layers or increase the thickness(es) of layers in TP structures, we could realize a better wavelength-selective absorption. However, these methods would increase the total thickness of the structure, which will cause more consuming energy to warm up the structure for every operation, and also increase the fabrication difficulties because of the large internal stress at the interfaces of layers. For example, the metal-OTS structure consumes about four times energy to warming up the sample than that of the modified TP structure; also, the total thickness is over 8 μm, which needs special treatment after deposition of each layer, otherwise, it will get damaged due to the strong internal strength. Therefore, the ultra-thick structure is not suitable for real application.

A detailed fabrication process of an ultra-thick dielectric layer stack by RF sputtering. The SiO2 material has a low sputtering rate of about 5 nm per minute, and thus an 800 nm thick layer needs around three hours. During the sputtering process, the heat will accumulate on the sample, and the long operating time will heat the sample up to 100 °C. If one keeps depositing this kind of thick layers, the temperature would be even higher. After deposition, taking off the samples from the stage will decrease the temperature to room temperature. Due to the large expansion rate difference between the two materials (Ge expansion rate is 5.90×10^{-6}/°C, while SiO_2 is 5.60×10^{-7}/°C), at the interface large internal stress will occur (Ge will shrink 10 times larger than the SiO_2). Therefore, (1) in order to avoid too high surface temperature, we avoided sputtering for too long time, and separated the fabrication into different days (only sputtered maximum

three hours for each time). (2) We did an annealing process up to 150 °C after every deposition process, in order to decrease the internal stress. However, note that after annealing, the thickness along a large surface area may not be very homogenous.

To constitute a DBR with less absorption loss is good for achieving a large Q-factor. Due to limited materials, we used Ge and SiO2 for the DBR for applications in both near-infrared and mid-infrared ranges. However, the DBR with a combination of Ge and ZnSe is good for mid-infrared range, while the combination of Si and SiO_2 is good for near-infrared range, because of near-zero absorption losses.

In the work of thermal emitter by metal-OTS structure, we developed a wavelength tuning mechanism by adjusting the temperature. However, as shown in Fig. 2.19c, the change in temperature will also affect the emission intensity. At 100 °C, the emission intensity is not strong, and the noise level is relatively large, so the signal to noise ratio is not stable for different wavelengths. Therefore, the tuning mechanism without change the peak intensity is strongly desired. Instead of this temperature controlling the emission, using an electrical method to control the wavelength will be better. For example, using EO polymer as the middle layer for the metal-OTS structure will be one possible solution.

For the photocurrent measurement for the M-S-ITO diode. Ti is used between Au and ZnO to create an ohmic contact for a lower Schottky barrier height and thus a larger photocurrent. However, the low barrier height also means a larger dark current (if we measure with certain bias), which could be unwanted for the photoconductor. Fortunately, our data can be measured with zero-bias. Also, it is found that the ohmic contact will convert to a Schottky contact when we put it in the air for one week, while it

will not change that much if put the diode device into a vacuum chamber. This is highly suspected to be related to the oxidation of the thin Ti layer.

As shown in Fig. 3.4(c), the response time is found to be low (large than 100 ms). There are two possible reasons: (1) the defects in the ZnO influence the response time; (2) the large capacity makes the response time slow. Therefore, in order to improve the response time, one should consider to use some well-crystalline semiconductor and/or to decrease the active area (the M-I-ITO area).

4.2 Outlook

4.2.1 Outlook about narrowband thermal emission devices

As shown in the Table 2.3, the thicker structures also show larger FOM values. However, as I mentioned in the previous section, the thicker the structure, the more difficult it can be in both fabrication and robustness. Therefore, naturally, it is desired for a structure with a thin configuration but a high FOM value. In the future, for thermal emitter design, we should not only concern for a high Q value, but also consider other aspects, such as a less angular dependence and a thin configuration.

For achieving the wavelength tunable propose, electrical controlled mechanism with EO polymer or piezo materials or phase change materials should be considered.

It should be feasible to design the multilayer structure by using deep learning methods. Also, using the computational methods, many difficult designs for human being can be achieved, such as design multiple emission peaks at multiple given wavelengths even for certain peak values. Or design for less angular dependence. Also, using deep learning, we could also design for absorption at certain range of wavelengths, which could find potential applications in radiative cooling and design for optical filters.

4.2.2 Outlook in wavelength-selective photodetector in multilayer configuration

Chapter 3 introduced a wavelength-selective photodetector in planar configuration (the TP photodetector has a thin metal film on top of a DBR). However, the wavelength selectivity as well as the large background could be improved. The thin metal film on top will induce much loss and a large background, which is not good for wavelength selective propose. In the future, configurations with DBR on top of a thick metal mirror needs to be considered (same configuration as the thermal emitters).

There is always a topic if TPs induced hot electron can be more efficient than those induced by SPs for a larger photocurrent. The first simulation paper gave an affirmative answer [ACS Nano 2017, 11, 1719−1727]. However, the paper doesn't take the plasmon-induced charge-transfer transition effect into account, and until now there is no experimental evidence supporting that point. Experimentally comparison the efficiency of hot carrier generations by TPs and SPs could be a topic for future studies.

Hot electron photodetection was first introduced to extend the working range for Si (enabling Si working beyond 1100 nm). However, under the framework of multilayer it is very difficult to utilize single-crystal Si materials as one of the layers, for high-efficient photodetection. Introducing Si into the layer stack should be considered as a topic.

Appendix: Fano resonances in one-dimensional metal-optical Tamm state structure: from a perfect absorber to a perfect reflector

A Fano resonance is observed as an asymmetric line-shape response that occurs through interference between a resonant process and a background continuum. It is named after Ugo Fano, who gave a theoretical explanation in 1961. As a general wave phenomenon, the Fano resonance can be found across many fields of physics, such as atomic physics, condensed matter physics, electrical circuits and optics. In recent years, Fano resonance has drawn renewed interest because of the progress modern nanotechnology. The shorter propagation distances in these nanoscale devices highlight the phase-coherent processes of waves, resulting in notable interference phenomena. The unique properties associated with the line-shape can not only be utilized as characteristic features or 'probes' for material analysis but also be utilized in the design of devices, such as transistors, switches, and filters.

In the field of nanophotonics, the Fano resonance was initially introduced and observed for plasmonic structures. The multiple resonance modes in a plasmonic structure provide opportunities for modes coupling or interferencing, creating conditions for versatile Fano resonances. Benefit from large field enhancement and asymmetric resonance profile, the plasmonics Fano resonances possess inherent sensitivity to changes in geometry or local environment: small perturbations can induce dramatic resonance or lineshape shifts. These properties render plasmonic Fano resonant media attractive for a range of applications, such as chemical or biological sensing, switching and electro-optics. However, for such plasmonic structures, ohmic losses and heating limit performance in many optical devices. For this reason, the study of Fano resonance in all-dielectric metamaterials have gathered attention. Compared with the plasmonic Fano resonance, the Fano resonances in all-dielectric metamaterials are superior for their high quality factor resonances (usually $Q > 100$), benefiting highly dispersive and low-loss photonic devices. Apart from these advanced applications, the Fano features in these nanostructures are relying on their 2D or 3D configurations. Thus, multiple fabrication processes, e.g., lithography, etching, liftoff, and sputtering, are needed, which may increase the fabrication cost and hinder their real applications.

To achieve large-area fabrications without added complexity in fabrication, a planar multilayer structure has many advantages. However, limited by resonance mode from the low-dimension configuration, it is hard to tailor Fano behaviors in 1D nanostructures for various applications. Actually, the theoretical study of a controllable Fano resonance in 1D structure has been reported. By inducing disordered permittivity

into a 1D dielectric diffractive Bragg gratings (DBR) structure, order-induced Bragg scattering interferes with disorder-induced scattering, which shapes the Bragg stop band into versatile Fano profiles. However, the stack of dielectric layers with varying permissivities are difficult to be actually realized. To date, experimental results of a Fano resonance with tailorable spectral profiles is yet to be reported.

In this work, we both numerically and experimentally achieve highly tailorable Fano resonances in a 1D metal-optical Tamm state structure (metal-OTS structure) forming from a thin metal film on top of an OTS resonator (Fig. 1a). Rich Fano resonances with narrow bandwidth (Q-factors above 1,000) originate from the interference between a lossy Fabry-Perot resonance within the metal film and a sharp quasi-OTS resonance. One of the immediate surprising effects we observe is that the metal-OTS structure can switch from a perfect absorber (corresponding to a Fano parameter q of -5) to a perfect reflector (a near-zero q) when changing the top metal films, as shown in Fig. 1b. Furthermore, independent from metal related Fano shape, the widths and the frequencies of the Fano resonances in the metal-OTS structures can be controlled by changing the geometry of the OTS component. Thus, the Fano resonances can be arbitrarily designed within a large range (as large as the DBR stop-band) without losing its Fano features. The Fano resonance with high flexibility, large Q-factor and independent controlling mechanism even have never been reported in a 2D or 3D nanostructure. Taking advantages of these properties, we also experimentally demonstrate a dispersion device by depositing a spatially distributed OTS layer, realizing a sub-nanometer distinguishing capacity of monochromic lights and a direct visualization of a molecular absorption fingerprint.

As a summary of the work, the investigated structure as well as the main effects are presented in Fig. 1. Illustrated in Fig. 1a, the metal-OTS structure is formed by a 20-nm metal film on top of an OTS structure consisting of two DBRs adjacent to each other with SiO$_2$ layers. In the following, unless mentioned otherwise, the Si and SiO$_2$ in OTS structure have fixed thicknesses of 111 nm and 268 nm, respectively, corresponding to a Bragg frequency of 6451.6 cm^{-1} (1550 nm). Interestingly, as shown in Fig. 1b, by using different metals on top, the structure can exhibit totally different optical behaviors: a perfect absorber transforms to a perfect reflector as the metal material is changed from Au to Ti with a constant thickness (for normal incident light). This drastic change in the optical behavior corresponds to a difference in Fano parameter q (from ~-5 for the Au structure to ~-0.05 for the Ti structure).

In order to characterize the optical properties of the proposed metal-OTS

structure, we first compare the optical behaviors of the metal-OTS structure with typical Tamm plasmon (TP) and OTS structures. Figure 2a shows the electric field magnitude distributions at resonance wavelengths of the TP, OTS and metal-OTS structures underlain with their configurations. The TP structure consists of a thin metal (Au) film and a DBR with alternating quarter-wave layers of Si and SiO_2, and the DBR connects to the metal with the Si layer. The OTS structure is formed by two DBRs with the same configuration adjacent to each other with SiO_2 layers. Each material corresponds to a fixed thickness in these three structures (t_{Au} = 20 nm, t_{Si} = 111 nm and t_{SiO2} = 268 nm), and the DBR layer numbers have been optimized for critical coupling conditions (strong resonance modes) in each structure. The electric field in the TP structure exhibits a relatively weak standing-wave pattern with a maximum electric field value near the Au thin film decaying towards the structure bottom, which indicated the TP mode existing at the interface between the metal and the DBR. A relatively small electric field in TP structure indicating small stored energy, which turns to a broad absorptance peak (corresponding to a Q-factor of 30, as the brown curve in Fig. 2b). Similar electric field distributions are found for the OTS and the metal-OTS structures, i.e., maximum values for the normalized electric field near the interface of the two DBRs (indicated as a white dashed line) decaying in intensity away from the DBR interface. Instead of using relatively lossy thin metal film to confine the light, the modes are mainly sustained within loss-less DBRs in the OTS and metal-OTS structure. As a result, larger energy can be stored in the OTS and metal-OTS structures, evidenced by the strong electric field, which contributes to resonance peak with larger Q-factor (see their spectra in Fig. 2b). Due to the lack of an inelastic loss channel, the OTS structure exhibits a transmittance peak at the resonance frequency. In contrast, the metal thin film in the metal-OTS structure provides an additional inelastic loss channel, resulting in a large absorptance peak instead of a transmission peak. Different from the symmetric spectrum profile of the OTS structure, with a thin metal film, the TP and metal-OTS structures can exhibit asymmetric Fano shapes, indicating that the thin metal film induced Fano resonances may universally exist in 1D resonantors. However, due to the damping in the TP structure is too large for the Fano resonance to be clearly observed.

To further identify and clarify the Fano resonance properties in the metal-OTS structure, we simplify the metal-OTS structure into a theoretical model, in order to derive spectrum expression into a form of the Fano formula. As shown in Fig. 3a, the two DBRs under the metal film can be re-separated into a symmetric OTS structure (i.e., the "cavity") defined by resonance bandwidth γ and an ideal DBR mirror with minus unity reflection coefficient (i.e., $r_3 \sim$ -1). Thus, the multilayered metal-OTS structure can be

simplified into three components: the metal thin film, the cavity, and the ideal mirror. r_1, r_2 are reflection coefficients of the upper and lower surfaces of the metal thin film. φ_m is the optical thickness of the metal film in the unit of phase, $\varphi_m = 2\pi t_m(n + ik)/\lambda$, where t_m is the real thickness of the metal layer with the refractive index of $(n + ik)$, and λ is the incident wavelength. Since the resonance in the metal-OTS structure is narrow in bandwidth, we assume that the n, k, r_1, r_2 and $\varphi_m = 2\pi t_m(n + ik)/\lambda_0$ to be constants against incident frequency (wavelength) within the small resonance range, where λ_0 is the central wavelength of resonance. The characteristic matrix for the whole structure can be written using the Transfer Matrix Method as follows

$$\text{M}_{total} = \begin{pmatrix} M_{11} & M_{12} \\ M_{21} & M_{22} \end{pmatrix} = K \begin{pmatrix} 1 & r_1 \\ r_1 & 1 \end{pmatrix} \begin{pmatrix} e^{-i\varphi_m} & 0 \\ 0 & e^{i\varphi_m} \end{pmatrix} \begin{pmatrix} 1 & r_2 \\ r_2 & 1 \end{pmatrix} \begin{pmatrix} 1 + \dfrac{\omega - \omega_0}{i\gamma} & -\dfrac{\omega - \omega_0}{i\gamma} \\ -\dfrac{\omega - \omega_0}{i\gamma} & 1 - \dfrac{\omega - \omega_0}{i\gamma} \end{pmatrix} \begin{pmatrix} 1 & r_3 \\ r_3 & 1 \end{pmatrix}, (1)$$

where $K = 1/(t_1 \, t_2 \, t_3)$, and t_1, t_2, and t_3 are the transmission coefficient of the upper and lower surfaces of the metal film and the bottom "mirror". The reflection coefficient spectrum of the whole structure is calculated as $r_{total}(t, x) = \dfrac{M_{21}}{M_{11}}$. Thus, the r_{total} can be expressed as

$$r_{total} = \frac{(i + 2\Omega)(r_1 + r_2 e^{2i\varphi_m}) - i(r_1 r_2 + e^{2i\varphi_m})}{(i + 2\Omega)(1 + r_1 r_2 e^{2i\varphi_m}) - i(r_2 + r_1 e^{2i\varphi_m})}, \tag{2}$$

where $\Omega = \dfrac{\omega - \omega_0}{\gamma}$. Since r_1, r_2 and $e^{2i\varphi_m}$ are complexes, we can rewrite them by separating the real and imaginary parts: $r_1 = r_1^{'} + ir_1^{''}$, $r_2 = r_2^{'} + ir_2^{''}$ and

$e^{2i\varphi_m} = e^{-4\pi \frac{kt_m}{\lambda_0}}(\cos\left(4\pi \frac{nt_m}{\lambda_0}\right) + i\sin(4\pi \frac{nt_m}{\lambda_0}))$. As a result, the real and imaginary parts in the numerator and denominator of r_{total} can be separated, and Eq. 2 can be written into the form

$$r_{total} = \frac{(a\Omega + b) + i(c\Omega + d)}{(e\Omega + f) + i(g\Omega + h)}. \tag{3}$$

In the case of weak transmission of the investigated metal-OTS structure, the absorptance spectrum can be calculated as

$$A_{total}(\Omega) \approx 1 - |r_{total}|^2 = 1 - \frac{(a\Omega + b)^2 + (c\Omega + d)^2}{(e\Omega + f)^2 + (g\Omega + h)^2}. \tag{4}$$

Then, the absorptance spectrum can be written into a form of

$$A_{total}(\Omega) = \frac{A\Omega^2 + B\Omega + C}{F\Omega^2 + G\Omega + H}. \tag{5}$$

Here, the expressions for *A, B, C, F, G,* and *H* can be given as follows:

$$A = 4\left(1 - r_1'^2 - r_1''^2\right)\left(1 - e^{-8\pi\frac{ktm}{\lambda_0}}\left(r_2'^2 + r_2''^2\right)\right) - 16e^{-4\pi\frac{ktm}{\lambda_0}}r_1''\left(r_2'\sin\left(4\pi\frac{ntm}{\lambda_0}\right) + r_2''\cos\left(4\pi\frac{ntm}{\lambda_0}\right)\right), (6.1)$$

$$B = 8e^{-4\pi\frac{ktm}{\lambda_0}}r_1''\left(1 - r_2'^2 - r_2''^2\right)\cos\left(4\pi\frac{ntm}{\lambda_0}\right) + 4\left(1 + e^{-8\pi\frac{ktm}{\lambda_0}}\right)r_2''\left(1 - r_1'^2 - r_1''^2\right), \quad (6.2)$$

$$C = \left(r_2'^2 - 2r_2' + 1 + r_2''^2\right)\left(\left(1 - r_1'^2 - r_1''^2\right)\left(1 - e^{-8\pi\frac{ktm}{\lambda_0}}\right) + 4e^{-4\pi\frac{ktm}{\lambda_0}}r_1''\sin\left(4\pi\frac{ntm}{\lambda_0}\right)\right), \quad (6.3)$$

$$F = 4e^{-8\pi\frac{ktm}{\lambda_0}}\left(r_1'^2 + r_1''^2\right)\left(r_2'^2 + r_2''^2\right) + 4 + 8e^{-4\pi\frac{ktm}{\lambda_0}}\left(\left(r_1'r_2' - r_1''r_2''\right)\cos\left(4\pi\frac{ntm}{\lambda_0}\right) - \left(r_1''r_2' + r_1'r_2''\right)\sin\left(4\pi\frac{ntm}{\lambda_0}\right)\right).$$

$$G = 4r_2''\left(1 - e^{-8\pi\frac{ktm}{\lambda_0}}\left(r_1'^2 + r_1''^2\right)\right) + 4e^{-4\pi\frac{ktm}{\lambda_0}}\left(1 - r_2'^2 - r_2''^2\right)\left(r_1''\cos\left(4\pi\frac{ntm}{\lambda_0}\right) + r_1'\sin\left(4\pi\frac{ntm}{\lambda_0}\right)\right), (6.5)$$

$$H = \left(r_2'^2 - 2r_2' + 1 + r_2''^2\right)\left(1 + e^{-8\pi\frac{ktm}{\lambda_0}}\left(r_1'^2 + r_1''^2\right)\right) - 2e^{-4\pi\frac{ktm}{\lambda_0}}\left(r_1'\cos\left(4\pi\frac{ntm}{\lambda_0}\right) - r_1''\sin\left(4\pi\frac{ntm}{\lambda_0}\right)\right). (6.6)$$

We then separate Eq. 5 into a Fano function and a Lorentz function:

$$A_{total}(\Omega) = \frac{A}{F}\frac{\left(\frac{2F\Omega+G}{\sqrt{4FH-G^2}} + \frac{\frac{BF}{A}-G}{\sqrt{4FH-G^2}}\right)^2}{\left(\frac{2F\Omega+G}{\sqrt{4FH-G^2}}\right)^2 + 1} + \frac{F}{A}\frac{\frac{4AC-B^2}{4FH-G^2}}{\left(\frac{2F\Omega+G}{\sqrt{4FH-G^2}}\right)^2 + 1}, \quad (7)$$

and the Fano parameter can be extract as (a function of t_m):

$$q(t_m) = \frac{\frac{BF}{A} - G}{\sqrt{4FH - G^2}}. \quad (8)$$

Figure 3b plots the calculated results of Eq. 8 as a function of t_m (in log-scale) for five different metals, namely, Au, Al, Ni, Pt, and Ti. The Fano parameter q for different metals follow an exponentially damped sinusoidal dependence as t_m increases. For low-reflection metals, i.e., Ni, Pt and Ti, the sine fluctuation is obvious; while for metals with high reflection, like Au and Al, the q values will first reach a minimum value for t_m around 20 nm, and then recover back to very small positive values for t_m above 100 nm. As depicted in the insets, the q value determines the shape of the Fano profile. The fact that q for metal-OTS structure can change within a large range from -5 to +0.2 indicates that the metal-OTS structure can exhibit versatile shapes in the absorptance spectrum: changing from an asymmetric Fano-shaped absorptance peak to a symmetric Lorentzian-shaped absorptance dip by varying t_m or changing the metal. The q values plotted in Fig. 3b are confirmed by the simulated absorptance spectra as shown in Fig. 3c for given t_m of 1, 10, and 100 nm and for different metals. Most of the absorptance spectra show Fano shape with a negative q (absorptance spectrum showing a peak at smaller frequencies and

a dip at larger frequencies), while, for the Ti, when the metal thickness is 1 nm, the absorptance spectrum exhibits an almost symmetric profile; for the 100-nm-Ti, Ni and Pt, the absorptance spectra is possible to show Fano profile with positive q values (a dip followed by a peak), which are in accordance with the results in Fig. 3b. Notice that light cannot transmit through these large metal thicknesses resulting in weak resonance in the absorptance spectra for t_m above 100 nm. Figure 3d plots the optical properties of metals, i.e., refractive indices n and reflectance at Bragg frequency for infinite thickness $|r_1|^2$. Comparing the $q(t_m)$ plots in Fig. 3b with the optical properties of metals in Fig. 3d, it is found that: (i) the modulation of the $q(t_m)$ is consistent with the reflection ability of the metal (i.e., the higher reflection ability, the larger negative q value it can achieve); (ii) the frequency for $q(t_m)$ crossing zero is positively correlated to the refractive index of the metal (i.e., the metal with larger n can have more t_m for a zero q value). For the first phenomenon, the reflection ability of the metal ($|r_1|^2$) can determine the ratio of light getting coupled into the structure, which affects the background of the Fano resonance, thus resulting in different the q values. We will discuss it in details by investigating the near field distributions of the metal-OTS structure with Au (the highest reflection) and Ti (the lowest reflection) in Fig. 4. For the second relation, we found that the frequency of $q(t_m)$ crossing zero roughly correlated to $2nt_m/\lambda_0$, indicating that the Fano resonance in metal-OTS structure should be related to the Fabry-Perot mode of the metal thin film (the mode sustained between metal's upper and lower surfaces).

As shown in the schematic diagram of Fig. 3e (left part), to clarify the origin of the Fano resonance in the metal-OTS structure, we have developed a theoretical model by considering the coupling between two resonators (Resonators A and B) inside the metal-OTS structure. Resonator A refers to the strongly damped Fabry-Perot mode inside the metal film (with the upper cavity mirror provided by the upper surface of the metal and the lower mirror provided by lower surface of the metal+DBR$_1$). Resonator B refers to the undamped quasi-OTS mode sustained at the interface between the two DBRs (DBR$_2$ acts as the lower mirror; the upper mirror is offered by the lower surface of the metal+DBR$_1$). Only Resonator A is directly driven by the incident electromagnetic wave, and the two resonators are coupled by sharing the same cavity mirror, i.e., metal's lower surface+DBR$_1$. The Fano resonance occurs when the resonance frequencies for these resonators are not consistent. The change of t_m or using different the metals will change the resonance frequency and/or the background of Resonators A, thus altering the Fano shapes in spectral profiles (we assume that the resonance frequency of Resonator B is independent from the t_m and possesses a value around Bragg frequency). The phase difference between the light reflected by the top surface of the metal and the lower surface,

104

i.e., $\text{Phase}(r_{m1}) - \text{Phase}(r_{m2})$, is a key parameter to understand the Fabry-Perot mode in Resonator A (note that $\text{Phase}(r_{m2})$ refers to the phase change for the whole route: (1) transmission through the upper surface, (2) transport through the film to the lower surface, (3) reflection from the lower surface, (4) transport to the upper surface, and (5) transmission through the upper surface, as shown in the inset of Fig. 3e). Figure 3e plots $\text{Phase}(r_{m1}) - \text{Phase}(r_{m2})$, for varying t_m at the Bragg frequency. As diagrams outside of the plot, when $\text{Phase}(r_{m1}) - \text{Phase}(r_{m2})$ has a value of π, r_{m1} will destructively interfere with r_{m2} leading to the Fabry-Perot resonance of the metal film appears coincident with that of Resonator B. Thus, the two couple resonators have a same resonance frequency, which satisfies the condition for electromagnetically induced transparency (EIT) and the q parameter vanishes (i.e., $q \sim 0$). When $\text{Phase}(r_{m1}) - \text{Phase}(r_{m2})$ has a value smaller (or larger) than π, Resonator A shows a resonance frequency larger (or smaller) than that of Resonator B, and the different relative spectral positions create q parameters with different signs. When the $\text{Phase}(r_{m1}) - \text{Phase}(r_{m2})$ has a zero value or the metal thickness is thin enough (e.g., less than 1 nm), Resonator A equivalents to a single interface instead of a cavity and therefore the Fabry-Perot resonance of Resonator A disappears. As there is only one resonator in the system (Resonator B) in the system, the Fano profile will disappear (i.e., $q \sim 0$). As shown in Fig. 3e, as t_m increases from zero, $\text{Phase}(r_{m1}) - \text{Phase}(r_{m2})$ varies the value between 0 and 2π periodically, so the function of $q(t_m)$ has a sine-type dependency around the zero value. The t_m values for $\text{Phase}(r_{m1}) - \text{Phase}(r_{m2})$ crossing 0 or π is roughly consistent with the t_m values for a q of zero in Fig. 3b, which provides evidence for our model. Interestingly, it is difficult to have a natural metal thin film for the metal-OTS structure to achieve a q value larger than $+1$, unless we replace the metal thin film by a metasurface. This two-resonator theory described in Fig. 3e can not only explain the Fano resonance in the metal-OTS structure but also the Fano resonances reported in the Fabry-Perot cavity structures and TP structures with a thin metal film on top of a DBR.

In order to study the reason for different q values using different metals in the metal-OTS structure, we further investigate the electric field and absorption distributions of the metal-OTS structures with 10-nm Au and 10-nm Ti as the top metal layers. Figure 4a shows the absorptance spectrum of the metal-OTS structure with a 10-nm Au film, exhibiting a clear Fano profile. The near-field behavior of the structure is investigated at four frequencies (Points A−D in Fig. 4a). Figure 4b presents the absorption distributions in the metal film (in the upper maps) and the electric field distributions of the whole structure (as the curve plots) together with the zoom-in plots around the metal thin film (shown in the red squared areas inserted in the electric field plots). As off-resonance

(background), the electric field distributions at Points A and D manifest weak standing-waves inside the structures and relatively strong standing-waves above the structures, indicating strong reflection properties. The absorption can be quantified as $\omega \text{Im}(\varepsilon)|E(z)|^2$, where ω is the angular frequency, and $\text{Im}(\varepsilon)$ is the imaginary part of permittivity. Due to a relatively large reflection ability of Au, at background wavelengths, the field cannot be coupled into the Au, resulting in a relatively low electric field and thus a low absorption. Point B corresponds to the absorptance peak, and as shown in the zoom-in plot of the electric field distribution around the Au, the metal film sustains a large electric field leading to the strong absorption. At Point C, the electric field exhibits a node at the center of the Au with small values, leading to a near-zero absorption. The metal-OTS structure with Au thin layer on top was fabricated and its reflectance together with its SEM cross-section image are shown in Fig. 4c. The measured reflectance spectrum under normal incidence shows a sharp dip at 6450 cm⁻¹ with a bandwidth of 5.76 cm⁻¹ (corresponding to a Q-factor of 1120). The simulation results of the absorptance and reflectance spectra are shown as the dashed curves by considering the actual dimensions in the fabricated structure. The simulated spectra reproduce the measured spectrum of the fabricated structures in terms of the position, bandwidth, and Fano profile.

Figures 4d-f show the results for the metal-OTS structure with the Ti thin film on the top of the structure. Due to the easy oxidation of the Ti thin film, we consider adding a SiO₂ protection layer on Ti to isolate the layer from its environment. Interestingly, it is found that this extra protection layer can also affect the Fano profile. Figure 4d shows the absorptance spectra as a function of the thickness of the protection SiO₂ layer (t_{cap}). As the layer thickness t_{cap} increases, the absorptance reveals oscillations in the resonance mode profile around a vertical line, indicating variations of the q value around zero. To clarify the effect of t_{cap}, three absorptance spectra with different thicknesses (t_{cap} = 0, 150, 380 nm) are shown on the right side of Fig. 4d, and the green arrows indicate the inconspicuous absorption peaks. Without the protection layer, the absorptance peak shows on the left side of the dip, revealing a $q < 0$ profile. As the t_{cap} increases, the spectrum successively shows a $q > 0$ (t_{cap} = 150 nm) and $q < 0$ (t_{cap} = 380 nm). The reason for the oscillations in the q values can be explained using the model in Fig. 3e: as the t_{cap} increases, the interference induced by the SiO₂ protection layer periodically modifies the resonance condition of the Resonator A and thus changes the Fano behavior. The control of the Fano shape by varying the protection layer thickness not only provides a simple means to adjust the profile of the spectrum but has also potential applications in sensing. It is noted that this effect of the protection layer on q is also found for the metal-OTS structure covered with Au. The near field behavior in the case of t_{cap} = 150 nm is

investigated for the four points E, F, G, and H shown in Fig. 4d. The absorptance dip at Point F features a similar behavior as the absorptance dip at Point C, showing a similar electric field distribution in the metal film. Since the electric field shows a node within the metal, the structure presents a minimum absorption. In contrast to the strong transmission in the standard OTS structure (see Fig. 2), Point F involves two light beams reflected respectively by DBR_2 and by Ti-DBR_1 that constructively interfere to give a strong reflection. Point G refers to the weak absorptance peak corresponding to Point C in Fig. 4. Unlike the Au thin film, the lossy Ti thin film cannot contribute to better light confinement at the absorption peak, which results in an electric field distribution with a weaker intensity than that of Point F, so the peak shows a broad profile with weak modulation. The poor reflection ability causes the light being coupled into the Ti easily, and even at the off-resonance frequencies of Points E and H, the Ti layer shows a relatively large electric field and an absorption values as strong as that of the absorptance peak. This high level off-resonance absorption leading to a q-near-zero symmetric shape corresponding to a narrowband reflection behavior. Figure 4f shows the measured reflectance spectrum of the fabricated metal-OTS structure with the top Ti layer. The cross-section of the fabricated metal-OTS structure observed with an SEM reveals a 10-nm-Ti thin-film covered by a 180-nm-SiO_2 protection layer. The reflectance spectrum exhibits a peak with a flat and weak background (reflectance < 0.08) and a slightly positive q value, in good agreement with the simulation results. The measured reflectance peak shows a bandwidth of 11.52 cm^{-1} (corresponding to a Q-factor of 560).

Different from the metal-dependent Fano shape, the resonance frequency is dominantly determined by the configuration of the OTS structure. Figure 5a shows the simulated reflectance spectra for Au (the upper plots) and Ti (the lower plots) of the metal-OTS structures for different thicknesses of the middle SiO_2 layer t_{mid} (as demonstrated on the right side). By varying t_{mid}, the resonance wavelength of OTS can be changed, leading to a shifting of the Fano resonance within a range as wide as the DBR stop-band. It is found that the change of t_{mid} shows little influence on the spectral background level, and ascribed to the flat backgrounds, the resonance can be tuned with a similar Fano shape. This property of the metal-OTS structure provides a means to design and fabricate Fano resonances that can be used in a wide range of wavelengths without losing their spectral features. However, in order to integrate different dimensions of 1D structure into one device, it requires lithography and etching processes to create different layer thicknesses on different positions, which will greatly increase the cost and complexity of the fabrications. Here, without adding fabrication difficulty, Furthermore, taking advantages of the properties of the ultra-narrow resonance and the wavelength tuning feature, we

experimentally demonstrate a means to realize a high-resolution dispersion device with Fano lineshape, without adding fabrication difficulties. By intentionally utilizing the inhomogeneous deposition region in the sputtering system, we deposited a slope layer for the middle SiO_2 layer (continuously varying t_{mid} along the sample surface). Thus, Fano resonances with different frequencies (wavelengths) can be excited and assigned to different positions along the x-axis covering a continuum range of frequencies (wavelengths). As depicted in Fig. 5b, when illuminate the slope metal-OTS structure with a monochromic light source, the metal-OTS structures with top Au ("absorber") and Ti ("reflector") can exhibit different behaviors: for the absorber, the reflected image of the sample surface will show a dark line at the specific spatial location matching with the resonance wavelength on a bright background; for the "reflector", the sample surface will show an opposite behavior with a bright line on a dark background. By reading the position of the lines, one can recognize the incident wavelength or distinguish different incident wavelengths, which enables a spectroscopic measurement without relying on a standard spectrometer such as an FTIR.

The fabricated devices are characterized by reflection images captured by an IR camera using a tunable laser as the monochromic incident light, as shown in the setup of Fig. 5c. The fabricated sample and the IR camera are mounted on a theta/2-theta rotation stage which is set to the angular position of 20°. A polarizer is used to select the transverse-magnetic (TM) polarization, and the light expander is used to obtain complete coverage of the fabricated sample (in the xy-plane). The reflected image is captured with an IR camera recording an image on the sample surface (the xy-plane) which is patterned with a scale to measure the position along the x-axis (the scale has a millimeter unit and was patterned by lithography). Figures 5d and 5e shows the captured images from the absorber (reflector) when the incident wavelength was varied slightly (left) and the intensity distributions as a function of the surface position (right). In Fig. 5d, a single dark line appears on a bright background for different incident wavelengths (the wavelength starts from 1430.0 nm, increases by small steps of 0.2, 0.5, 1.0, 2.0, and 5.0 nm). It is clear from the intensity distribution plots that the small changes of the incident wavelength presented by the shifts of the Fano-shaped dips. For the reflector, a single bright line appears on a dark background and shifts when the incident wavelength is varied (Fig. 5e). Due to a relatively broad resonance, the reflector can show a similar response (shift of intensity peaks with a similar trend) for larger increasing steps of the incident wavelength: 0.5, 1.0, 2.0, 5.0, and 10.0 nm. From the intensity distribution plots, both the absorber and the reflector show response to the slight change in the incident wavelength, indicating a sub-nanometer resolution ability. Moreover, it is found that with

a given bandwidth, the steep profile of Fano shaped target lines can further benefit the distinguishing ability of the light.

The advantages of the reflector (metal-OTS structure with Ti on top) embedded in its high-intensity signal and low-intensity background attributed to its q-near-zero Fano resonance (i.e., the bright line in the dark background). This optical behavior is particularly attractive because each wavelength component can be presented independently with little influence from the background of other wavelengths, which could enable monitoring for multiple wavelengths using a broadband light source. Also, benefit from a high spectral resolution of the reflectance device ($\sim$6 cm^{-1}, which is as high as commercial grating-based spectrometers), we could demonstrate a direct visualization of the molecular absorptance fingerprint. When a molecular sample is inserted on the light path between a broadband source and the reflector device, light transmission through the molecular sample will be reduced at some given wavelengths owing to the molecular fingerprint absorption. Therefore, the certain positions on the device surface corresponding to characteristic absorption fingerprint wavelengths reveal as dark lines, like a barcode. Superior to a normal barcoding pattern with only position and width information, this reflected pattern can also reveal the real absorbance intensity of the molecular sample by the darkness of each bercoding. Here, direct visualization of the molecule absorption fingerprint is demonstrated with the dichloromethane (CH_2Cl_2) molecules, which can provide rich characteristic fingerprints within the near-infrared range (marked as Areas A, B, and C with an FWHM of 50 cm^{-1} in the wavelength range from 1390-1450 nm).

Figure 6b shows the setup for the fingerprint monitoring purpose. An incandescent light source is employed to cover the near-infrared wavelength range, and an optical filter is used to select the measurement wavelength range of 1300~1500 nm. A spectroscopic cuvette with a path length of 2 cm is filled with the target molecule CH_2Cl_2. Figure 6c shows the images captured by the IR camera after normalization by the intensity distribution without the CH_2Cl_2. Three dark regions are found on the image (marked as Areas A, B, and C), forming a barcode along the x-axis. After calibrating the position on the x-axis with respect to the wavelength, the intensity spectrum of the reflection image (solid curve) was recorded and graphed in Fig. 6d together with the transmittance spectrum of the CH_2Cl_2 (dashed curve) measured with an FTIR spectrometer. The intensity distribution is found to well approximate the absorption signature of the CH_2Cl_2 molecule in terms of wavelength, bandwidth, and modulation. Thus, a spectrometer-free visualization of the molecular absorption fingerprint was made possible without the need for a dispersion. As shown in Fig. 6d, comparing the real transmittance spectrum, the

imaging-based spectroscopy result reveals a lower intensity level for the shorter wavelengths. This distorted distribution of intensity may be caused by the inhomogeneous signal and background intensity levels along the surface of this imaging-based spectrometer. Taking advantage of the fine controlling mechanism of the Fano shapes within a wide wavelength range of the metal-OTS structure, the realization of an even flatter and weaker background of this imaging-based spectrometer should make it possible to further improve the sensitivity.

In conclusion, we both numerically and experimentally demonstrated that the 1D metal-OTS structure presents versatile Fano resonance profiles with narrow resonance bandwidth through the interference between lossy Fabry-Perot mode in the metal thin film and the sharp quasi-OTS mode. By selecting the metal and/or controlling its thickness, the Fano parameter was controlled from approximately -5 to a near-zero value. This range of variation makes it possible to cover the complete range of optical behaviors for the spectral profiles from a perfect absorber to a perfect reflector. Moreover, we revealed that besides in the metal-OTS structure, the lossy Fabry-Perot mode of the thin metal film should universally exist and participate in shaping the Fano profiles in well-known 1D nanostructures including Fabry-Perot cavity (with metal mirror) and Tamm plasmon structure. This thin film related Fano behavior could also be employed as a material analysis technique, for example for non-destructive monitoring of minute changes in thin-film materials (such as 2D materials, epsilon-near-zero thin films or phase-change materials). Other advantages of the metal-OTS structure lie in its narrowband resonance (a Q-factor more than 1000) with a flat and wide-range background, and the possibility to tune the resonance frequency by adjusting the OTS dimension without losing its Fano features. Hence, by introducing a continuous variation in the thickness of the OTS structure, a Fano resonance can be excited for a continuum of frequencies along the structure surface. By designing the structure to generate a sharp resonance with a steep Fano profile, we have experimentally realized imaging-based spectroscopy achieving a sub-nanometer wavelength distinguishing capacity. Furthermore, taking advantage of the low-level background of the spectrally clean reflection peak ($q \sim 0$), the proposed spectroscopy technique enabled direct visualization of spectrum using a broadband light source. Exploiting this technique, we demonstrated the direct visualization of the molecular absorption fingerprint for the CH_2Cl_2 molecule. It should be noted that the large electric field enhancement inside the metal-OTS structure (at the interface between the two DBRs) offer potential benefit for high-sensitivity molecule detection. This large electric field enhancement could be exploited by

introducing the target molecules into the center region of the metal-OTS structure through micro/nanochannels or porous materials. The reported lithography-free metal-OTS structure offers well defined and controlled Fano resonances with demonstrated spectroscopic ability that could pave the way for various practical applications, such as a quick and label-free sensing, portable material property monitoring, and optical switching and filtering.
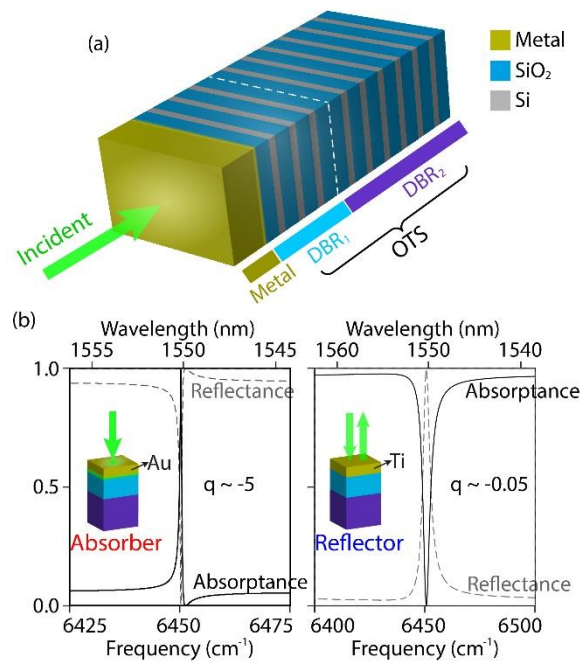
Figure 1 (a) Schematic diagram of the metal-OTS structure consisting of a metal thin film on top and two DBRs underneath. (b) Opposite optical responses for different metals on top: a 20-nm Au corresponding to spectrally selective absorption and a 20-nm Ti corresponding to spectrally selective reflection.
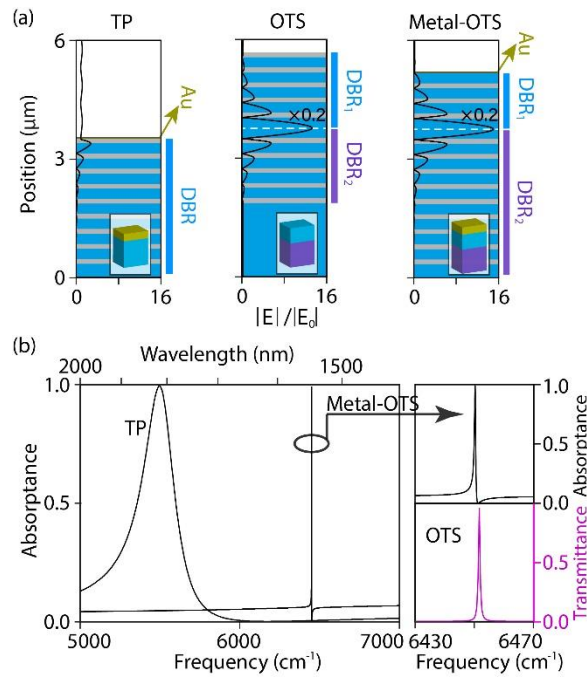
Figure 2 (a) Configurations and normalized electric field magnitude of the TP, OTS, and metal-OTS structures. The thicknesses of DBR layers are the same as in Fig. 1, and the thicknesses of Au thin films in the TP and the metal-OTS structure are fixed at 20 nm. (b) Left: absorptance spectra of the TP and the metal-OTS structures; right: comparison between the magnified transmittance spectrum of the OTS structure and the absorptance spectrum of the metal-OTS structure.
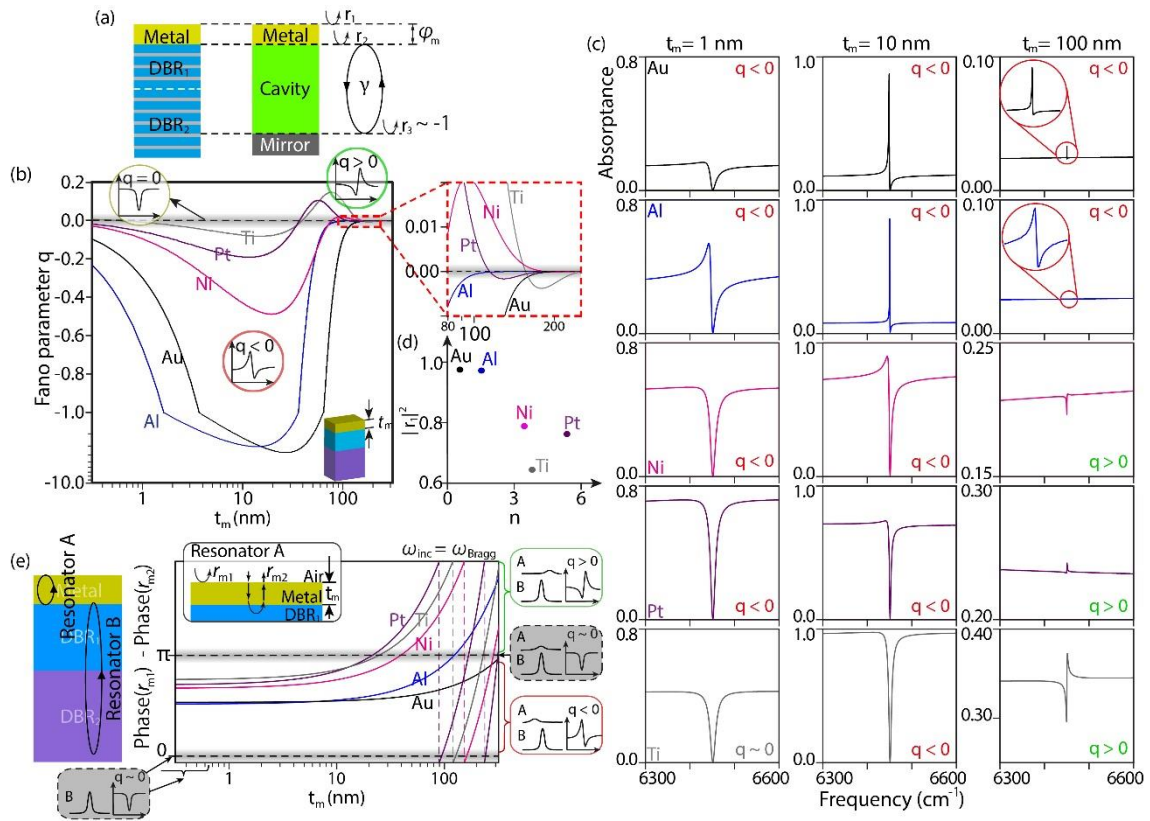
113

Figure 3 (a) Schematic diagram of the theoretical model for the metal-OTS structure. (b) Calculated results of Fano parameter q as a function of the metal thickness t_m for the metal-OTS structure with different metals (Au, Al, Ni, Pt, and Ti). (c) The simulated absorptance spectra of the metal-OTS structures with different metals and thicknesses. (d) Optical properties (real part of refractive index and reflectance for an infinite thickness) of the metals used: Au, Al, Ni, Pt, and Ti. (e) The "two-resonator" model used to explain the physical origin of the Fano resonance behavior in the metal-OTS structure.
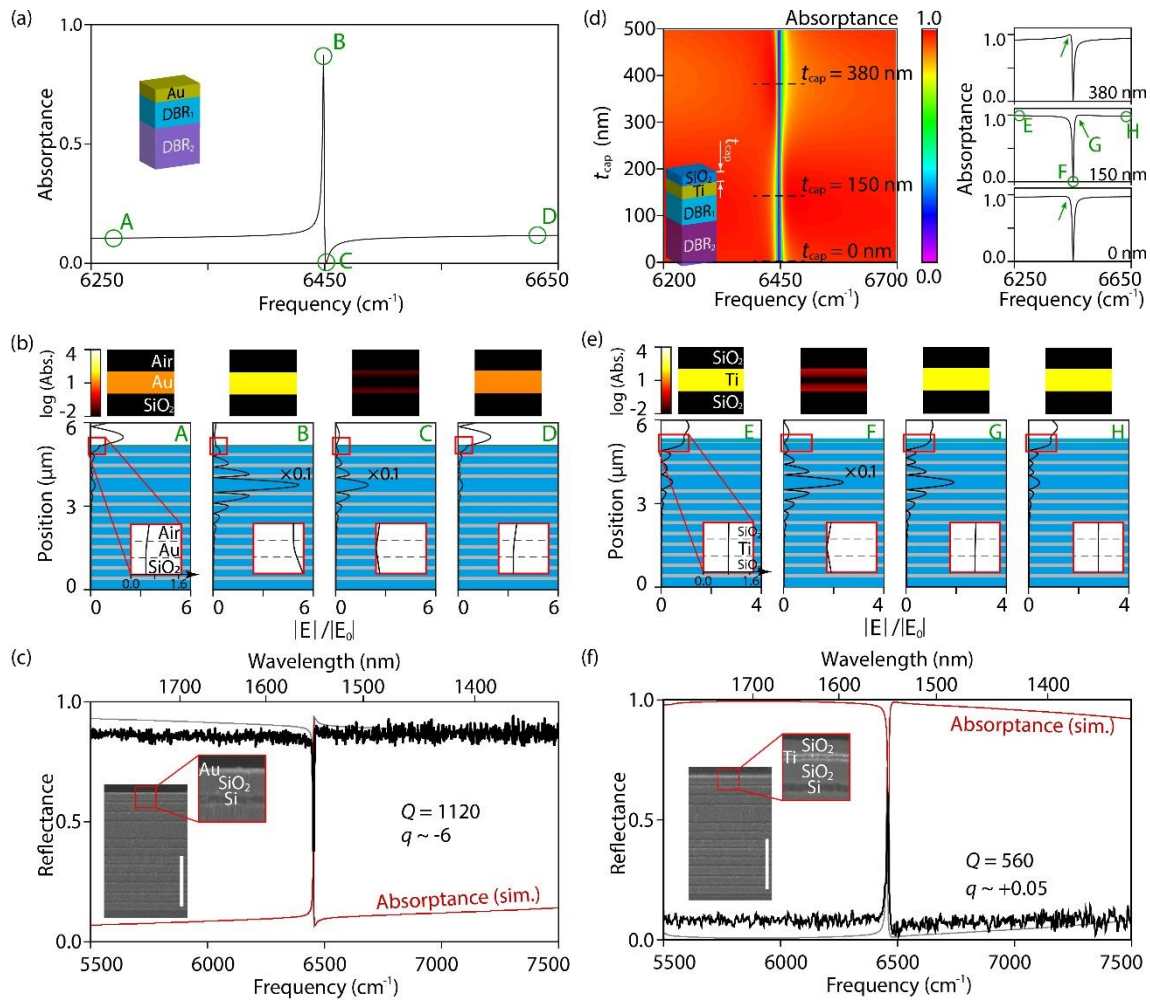
Figure 4 (a) Simulated absorptance spectrum of the metal-OTS structure with 10-nm Au on top. (b) The electric field magnitude distribution at Points A, B, C, and D with their zoom-in plots around the Au film (inset) and the absorption distribution in the Au film (on top of the electric field profiles). (d) The simulated absorptance of the metal-OTS structure with 10-nm Ti on top varying with frequency and the thickness of the SiO_2 protection layer t_{cap}. The absorptance spectra for the three t_{cap} are exhibited on the right side. (e) The electric field magnitude distribution at Points E, F, G, and H with their zoom-in plots around the Ti film (inset) and the absorption distribution in the Au film (on top of the electric field plots). Experimental reflectance spectrum of the fabricated samples with 10-nm Au (c) and 10-nm Au protected by 180 nm SiO_2 (f) (in black) together with simulated reflectances (in gray) and absorptance spectra (in red).
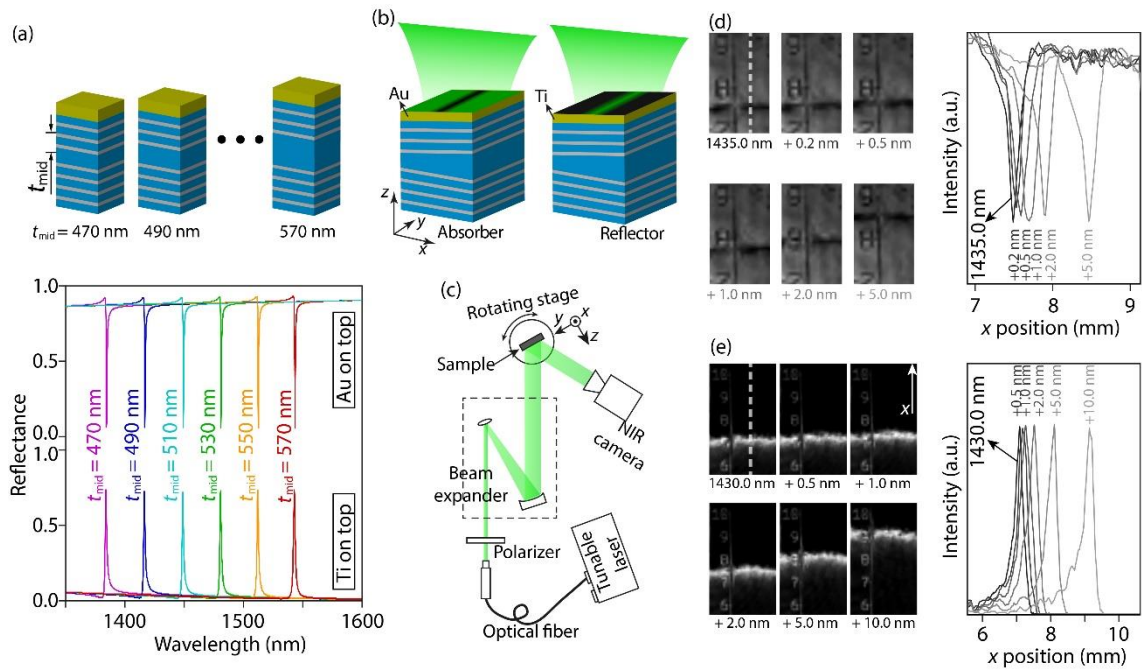
Figure 5 (a) The simulated absorptance and reflectance of the Au-on-top and Ti-on-top structures with varying light wavelength and thickness of the middle SiO$_2$ layer t_{mid} under normal incident light. (b) Illustration of the optical behaviors for the "absorber" and "reflector" devices. (c) The measurement setup. Reflected images of the monochromic light by the (d) Au-on-top and (e) Ti-on-top metal-OTS structures.
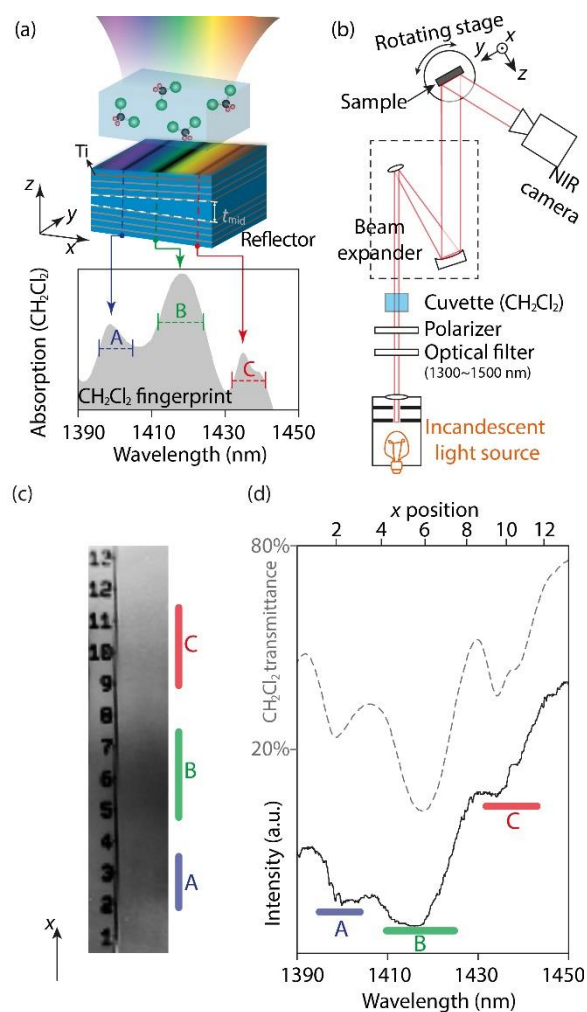
Figure 6 Visualization of the CH_2Cl_2 molecular absorptance fingerprint. (a) Illustration of the mechanism of the measurement. (b) Setup of the measurement. (c) Images captured by IR camera after normalization by the intensity distribution without the CH_2Cl_2. (d) Intensity spectrum of the reflection image, together with the transmittance spectrum of the CH_2Cl_2 measured with the same cuvette (dashed curve).